Institut de Physique de l'Université de Neuchâtel

Near infrared intersubband absorption and photovoltaic detection in GaN/AlN multi quantum well structures

Thèse

Présentée à la Faculté des Sciences de l'Université de Neuchatel

Pour l'obtention du grade de Docteur ès sciences

Par

Esther Baumann

Soutenue le 14 août 2007

En présence du directeur de thèse

Prof. Daniel Hofstetter

et des rapporteurs

Dr. Eva Monroy et Prof. Hans-Peter Herzig

Université de Neuchâtel **unine**

FACULTE DES SCIENCES
Secrétariat-Décanat de la faculté
- Rue Emile-Argand 11
- CP 158
- CH-2009 Neuchâtel

IMPRIMATUR POUR LA THESE

Near infrared intersubband absorption and photovoltaic detection in GaN / AlN multi quantum well structures

Esther BAUMANN

UNIVERSITE DE NEUCHATEL

FACULTE DES SCIENCES

La Faculté des sciences de l'Université de Neuchâtel,
sur le rapport des membres du jury

Mme E. Monroy (Grenoble F),
MM. D. Hofstetter (directeur de thèse)
et H.P. Herzig

autorise l'impression de la présente thèse.

Neuchâtel, le 27 septembre 2007

Le doyen :
T. Ward

...ERSITE DE NEUCHATEL
FACULTE DES SCIENCES
Secrétariat-décanat de la faculté
Rue Emile-Argand 11 - CP 158
CH-2009 Neuchâtel

Keywords

- Semiconductor heterostructures
- Intersubband transitions
- Near infrared
- Group III nitrides
- Photoinduced polarization

Mots-clés

- Hétérostructures semiconductrices
- Transitions intersousbandes
- Infrarouge proche
- Nitrures d'élément III
- Polarisation photoinduite

Abstract

Due to the large conduction band offset of nearly 2 eV between GaN and AlN, group III nitride semiconductor heterostructures are of great interest for optoelectronics based on intersubband transitions (ISBTs). These properties allow the extension of the ISBT wavelength range into the near infrared.

In this work near infrared ISBTs in GaN/AlN heterostructures were investigated for samples grown by both plasma assisted molecular beam epitaxy (PAMBE) and metal-organic vapor-phase epitaxy (MOVPE). It was shown in the experiment that a 15 Å thick quantum well (QW) absorbs light around 800 meV (1.5 µm). The highest ISB absorption energy for PAMBE samples in this work is 890 meV (1.39 µm) and 834 meV (1.49 µm) for MOVPE. Those results show that both growth techniques are appropriate to achieve short ISBT wavelengths.

As group III nitrides are non-centrosymmetric, strong piezo- and pyro-electric fields occur in GaN/AlN heterostructures; they lead to intrinsic asymmetries in the electronic potential of a multi quantum well (MQW) structure and give rise to nonlinear optical phenomena. Based on the photoinduced polarization detection mechanism, ISB detectors were designed and investigated. Photovoltaic responses, which originate both from linear absorption as well as from step two-photon absorption were measured. These prototype photoinduced polarization photodetectors work up to room temperature. The frequency response obtained with a modulated telecommunication laser diode showed a signal up to 3 GHz.

A narrow-band electro-optic modulator prototype working around 1.5 µm based on the depletion of a GaN/AlN MQW region is also presented.

Those results on modulation and fast photovoltaic detection at 1.55 µm illustrate the application potential of group III nitride ISB devices as electro-optic detectors and modulators for long-haul optical fiber telecommunication.

Contents

1 Introduction **1**
1.1 Historical overview . . . 1
1.2 Motivation and outline of this thesis . . . 2

2 Group III Nitrides **5**
2.1 Material properties . . . 5
2.1.1 Crystalline structure . . . 6
2.1.2 Polarization in wurtzite nitride structures . . . 8
2.1.3 Electrical and optical parameters . . . 12
2.2 Growth . . . 13
2.2.1 Plasma assisted molecular beam epitaxy . . . 14
2.2.2 Metal-organic vapor-phase epitaxy . . . 17
2.2.3 Dislocations and defects . . . 18

3 Theoretical Background **19**
3.1 Electron wavefunctions in quantum wells . . . 19
3.1.1 Schrödinger equation . . . 19
3.1.2 The envelope function model . . . 20
3.1.3 Intersubband absorption coefficient of a single quantum well . . . 21
3.1.4 Intersubband transitions in group III nitrides . . . 26
3.2 Photodetector physics . . . 28
3.2.1 Rectification voltage and two photon absorption in asymmetric quantum wells . . . 29

4 Design and Simulation **35**
4.1 Simulation programs . . . 35
4.2 Common ISB photodetector designs . . . 35
4.3 Photoinduced polarization detector design . . . 38
4.4 Sample geometry . . . 40

5 Experimental Setup **43**
5.1 Sample preparation . . . 43
5.2 Spectral measurements . . . 44
5.2.1 Absorption . . . 45
5.2.2 Photovoltage . . . 47
5.3 Frequency response . . . 47

6 Absorption Measurements 49
6.1 Rapid scan absorption for MOVPE and PAMBE grown samples 49
6.2 Rapid scan absorption of samples with $Al_xGa_{1-x}N$ barriers 54
6.3 Electromodulated absorption of MOVPE samples 55
6.4 Electromodulated absorption for different external fields 57
6.5 Comparison of electromodulated and rapid scan absorption 58

7 Probing the Band Structure using Electromodulated Absorption 61
7.1 Electromodulated absorption of samples with two, five and ten periods . . . 61
7.1.1 Comparison of samples grown on GaN and AlN template 66
7.2 Modulator prototype 67
7.2.1 Waveguide 69

8 Photodetectors 71
8.1 Comparison of mesa and stripe process 71
8.2 Different thickness of AlN barriers 73
8.3 Different number of periods 76
8.4 Different GaN QW thickness 78
8.5 Different $Al_{1-x}Ga_xN$ barriers 80
8.6 Different cap thicknesses 82
8.7 PV response measured with a laser 83
8.7.1 Rectification voltage amplitude 86
8.8 MOVPE samples 87
8.9 PV originating from higher levels 90
8.10 Photodetector design guidelines 94

9 Conclusions 95

Bibliography 99

Publication list 109

A Band Alignment and Metal Work Function 111

B Brewster Angle Transmission 113

C X-ray 115

D PL Measurement 117

E CV Measurement 119

F Resonant Tunneling Diode Design 121

G Input return loss S11 125

H Multipeak Absorption 127

I Different Growth Temperatures **129**

List of Figures

2.1 Bandgap vs lattice constant of common semiconductors 6
2.2 GaN crystal structure 6
2.3 Ga- and N-face crystal 7
2.4 Piezo- and pyroelectric polarization 10
2.5 Polarization at a GaN/AlN heterostructure 11
2.6 Sapphire lattice constant for AlN 14
2.7 AFM of sample E890 16
2.8 AFM of sample E888 and TEM of sample E882 16
2.9 AFM of sample E740 17
2.10 TEM showing defects 18

3.1 Reflection at Air/AlN interface 25
3.2 Standing wave intensity in an MPW 26
3.3 Internal fields in GaN QWs and AlN barriers 28
3.4 Simulated Stark shift in a GaN QW 29
3.5 Conduction band simulations of asymmetric QWs 30
3.6 Conduction band simulation of a 15 Å QW with AlN barriers 32

4.1 Schematic band diagrams of a QWIP and a QCD 36
4.2 Conduction band simulation of III-N QWIP and QCD 37
4.3 Tunneling probability as function of AlN barrier thickness 38
4.4 Simulations of regular AlN/GaN SLs 39
4.5 Simulations for different QW thicknesses 40
4.6 ISB waveguides 41

5.1 Submount picture 44
5.2 Beam condenser schema 45
5.3 Perpendicular transmission of E1208 46
5.4 EMA sample process schema 46
5.5 Spectrum of the spectrometer's internal lamp 47
5.6 Frequency response measurement setup 48

6.1 Measured and theoretical absorption peak energy as function of QW thickness 51
6.2 Transmission of series with different QW thicknesses 52
6.3 Measured and simulated ISBT energies of E1293, E1295, E1291, E1297, and E1295 53

6.4 Transmission of series with 60%, 70% and 100% Al barriers 54
6.5 Image of A699 surface showing cracks; EMA of A767, A663, and A699 . . . 56
6.6 EMA of A767 for different voltage amplitudes 57
6.7 HRXRD of E728, E739, and E740 58
6.8 Transmission of E728 and E740 and EMA of E740 59

7.1 Structure of series with 2, 5, and 10 periods 62
7.2 EMA of 2, 5, and 10 period samples under MIS contact 63
7.3 Schematic conduction band of a 2 and 5 period sample 63
7.4 EMA of 2, 5, and 10 period samples under MS and MIS contact 64
7.5 Computed integrated absorbance as function of sheet carrier density 65
7.6 EMA of 15 Å QWs showing a shift between AlN buffer and GaN buffer . . . 66
7.7 Rapid scan and EMA differential transmission for different voltages of E887 67
7.8 Modulator conduction band schema 68
7.9 Slab waveguide simulation of sample E966 69

8.1 Transmission and normalized PV of sample E740 72
8.2 I-V measurement of E740 mesa process 72
8.3 PV spectra of series with different barrier thicknesses 74
8.4 Peak PV height for series with different barrier thicknesses as function of temperature 74
8.5 Simulations of QW between AlN barriers of different widths 75
8.6 Transmission and PV of series with different number of periods 77
8.7 Absorbance and PV of gs1709, gs1752, and gs1758 78
8.8 Transient PV of gs1758 with and without Si optical filter 80
8.9 Transmission and PV of series with different barrier Al content 81
8.10 Equivalent circuit for illuminated sample 83
8.11 Transmission and PV of series with varying AlN cap thicknesses 84
8.12 PV peak as function of temperature and cap thickness 84
8.13 PV at different temperatures and transmission of E1065 85
8.14 Frequency response of E1065 86
8.15 Computed rectification voltage as function of intensity. 87
8.16 Structure of MOVPE samples A699, A1003 and A1007. 87
8.17 PV response of A699 88
8.18 PV response of A1003 and A1077 88
8.19 Frequency response of A1003 and A1077 90
8.20 Computed $\Pi\tau$ and E_{13} of a 15 Å QW for different barrier thicknesses; PV of E1299 91
8.21 TPA PV of E1208; laser PV of E1206 92
8.22 Fundamental peak energy as function of laser drive current 93

B.1 Brewster angle transmission of E1208 as function of temperature 113

C.1 X-ray and reciprocal space mapping of E1065 116
C.2 X-ray measurement of sample A699. 116

D.1 Photoluminescence of series with different barrier thicknesses 117

D.2 PL of samples with different number of periods resp. cap thicknesses 118
D.3 Photoluminescence of series with different well thicknesses 118

E.1 CV measurement of samples E889 (left) and E888 (right). 119

F.1 Simulation of the RTD structure E926 121
F.2 Design of the RTD structure E926. 122
F.3 X-ray measurement of sample E926. 122
F.4 Transmission of the RTD structure E926 123

G.1 Reflection amplitude and phase of E1065. 125
G.2 Resistance and capacitance of E1065. 125

H.1 Multipeak transmission of E1132 127

I.1 PV of samples with different growth temperatures 129

List of Tables

2.1 Wurtzite nitride parameters 7
2.2 Spont. polarization, piezoelectric moduli and constants, and elastic constants for GaN, AlN, and InN 9
2.3 Group III nitrides bandgap parameters 12
2.4 Dielectric constants for AlN and GaN 13

3.1 Parameters extracted from the simulation of a 15 Å QW with AlN barriers . 32

6.1 Nominal growth parameters of various samples 50
6.2 Measured absorption peak position and FWHM of various samples 51
6.3 Various values of sample series with different QW thicknesses 53
6.4 Structure parameters for MOVPE samples investigated by EMA. 55

7.1 Template material of the 2, 5, and 10 period samples 62
7.2 Parameters used for absorbance calculation of 2, 5, and 10 period samples . 65

8.1 Measured PV peak and FWHM for samples E1206 – E1211 73
8.2 Integrated absorbance and PV of samples with different number of periods 77
8.3 Structure of samples gs1709, gs1752, and gs1758 78
8.4 Series with different barrier Al content 81
8.5 Nominal cap layer thickness and integrated absorbance of E1300, E1301, E1297 and E1299. 83
8.6 Measured peak position and FWHM of MOVPE samples A699, A1003 and A1077. 89

A.1 Metal work functions and Schottky barrier heights 111

I.1 Growth temperature of samples E1174, E1176, and E1178. 129

Chapter 1

Introduction

1.1 Historical overview

Since the demonstration of the first transistor made of Germanium (Ge) by John Bardeen, Walter Houser Brattain and William Bradford Shockley in December 1947, the research field of semiconductors has literally exploded. From the early seventies on, Silicon (Si) was the preferred material for the fabrication of transistors and rectifiers due to its superior electrical properties as compared to Ge. The third classical semiconductor is Gallium Arsenide (GaAs), a compound of Gallium and Arsenic in which the saturated electron velocity and mobility exceeds the values found in Si. Therefore, GaAs devices can be operated at higher frequencies than Si. In addition GaAs has a direct bandgap, allowing for efficient photon-electron interactions. Already in 1955 Rubin Braunstein of the Radio Corporation of America (RCA) first reported on infrared emission (electroluminescence) of GaAs and in 1962 Nick Holonyak Jr. created the first light emitting diode (LED) emitting visible light in $GaAs_{1-x}P_x$. In 1957 Herbert Kroemer proposed heterostructures using sequences of thin semiconductor layers with different bandgaps. With this technique, Zhores Alferov demonstrated the first $GaAs/Al_xGa_{1-x}As$ continuous wave semiconductor laser 1970 in the Soviet Union.

Heterostructures allow to design semiconductor layers with a one-dimensional confinement of the carrier wave functions, leading to quasi-two-dimensional electron (hole) states in the conduction (valence) band called subbands. Dingle et al. [1974] published experimental evidence of quantized levels associated with the confinement of carriers. West and Eglash [1985] from Stanford University investigated heterostructures consisting of a thin GaAs layer (called quantum well, QW) sandwiched between two $Al_{0.3}Ga_{0.7}As$ layers (called barriers); they were the first to measure the absorption between two conduction subbands, which later became generally known as intersubband (ISB) absorption, and the inverse dependence between peak ISB absorption energy and QW thickness. Since then the field of conduction band ISB transitions (ISBTs) was widely explored, initially in unstrained GaAs-AlGaAs and in InGaAs-InAlAs grown on InP and later on also in InGaAs-AlGaAs, InGaAs-AlAsSb, and in AlGaN-GaN heterostructures. Levine et al. [1987] demonstrated the first quantum well infrared photodetector (QWIP) and eight years later, Faist et al. [1994b] reported on the first quantum cascade laser (QCL).

Tiede et al. [1928] were the first to synthesize Aluminum nitride (AlN); the first

report on the synthesis of Gallium nitride (GaN) is by Johnson et al. [1932]. Those early group III nitrides synthetizations were however only in the form of powder, very small crystals or needles. In 1968, J. Tietjen's group at the RCA worked towards a full color image using LEDs. Red GaAs based and yellow-green Gallium Phosphide (GaP) based LEDs being available, the missing link was a blue LED, for which the wide bandgap semiconductor GaN was a promising candidate. Maruska and Tietjen [1969] successfully applied the growth technique known as Hydride Vapor Phase Epitaxy (HVPE), previously used to prepare GaAs, GaP and GaSb, to GaN using a [0001] orientated single crystalline sapphire substrate; this is the first report on single crystalline, colorless GaN. Although non intentionally doped, those GaN films showed n-type conductivity and typical electron concentrations of $1-5\times10^{19}$ cm^{-3}. The group at RCA processed a device consisting of insulating-to-n-type GaN layers and an indium surface contact, the first GaN LED. Its emittance around 480 nm was due to Zn acceptor levels in GaN [Pankove et al., 1971a,b]. In the same year, Dingle et al. [1971] from Bell Labs investigated GaN layers grown on sapphire with a reduced electron concentration of about 10^{17} cm^{-3} and showed that GaN is a direct bandgap semiconductor with a lowest exciton state of 3.474 eV at 2 K. The lack of a lattice matched substrate, the high intrinsic n-type doping, and problems with p-type doping however remained major challenges in the development of single crystalline group III nitride heterostructures and retarded their development in comparison to other III-V material systems.

Yoshida et al. [1983] proposed a growth technique using an intermediate AlN layer between sapphire and GaN reducing the impact of the lattice mismatch between substrate and epilayer. Amano et al. [1989] succeeded on GaN p-type doping with Magnesium which led to the demonstration of the first GaN p-n junction LED by the same group [Akasaki et al., 1991]. Since then, the interest in wurtzite single crystalline group III nitrides increased rapidly again. Their wide band gap range between 0.7 eV for InN and 6.2 eV for AlN, strong bond strengths, and high electron mobility [Ambacher et al., 1999] made group III nitrides the material of choice for solid-state light emitting devices in the blue and ultraviolet and for high power high frequency high electron mobility transistors (HEMTs).

Nakamura et al. [1994] at Nichia Chemical Industries, Tokushima, manufactured the first Indium Gallium nitride (InGaN) high-brightness blue LED (450 nm), followed by LEDs emitting at 525 nm (green) and 590 nm (yellow) [Nakamura et al., 1995]. The first blue InGaN laser emitting at 417 nm was reported by Nakamura et al. [1996]. Khan et al. [1993b] reported on a metal semiconductor field effect transistor (MESFET) in GaN and on an HEMT based on a GaN/$Al_xGa_{1-x}N$ heterostructure [Khan et al., 1993a]. Moreover different groups demonstrated solar-blind UV-detectors [Munoz et al., 2001]. Today Nichia and Osram have a commercial production of GaN based LEDs and Fujitsu fabricates GaN/$Al_xGa_{1-x}N$ HEMTS.

1.2 Motivation and outline of this thesis

In the GaAs/AlGaAs or the $In_{0.52}Al_{0.48}As/In_{0.53}Ga_{0.47}As$ systems, the ISBT operation range is limited towards high energies by the conduction band offset (CBO) of 1.0 eV respectively 0.52 eV [Vurgaftman et al., 2001]. Semtsiv et al. [2007] demonstrated a short

wavelength QCL emitting at 3.05 μm using strained AlAs/$In_{0.73}Ga_{0.27}As$ layers. An alternative to reach shorter ISB wavelengths is the $In_{0.52}Ga_{0.48}As/AlAs_{0.56}Sb_{0.44}$ system lattice matched to InP with a CBO of 1.6 eV [Georgiev and Mozume, 2001], with which a quantum cascade detector operating at 2.04 μm was realized [Giorgetta et al., 2007]. Compared to the heterostructures mentioned above, GaN/AlN not only offers a larger CBO of almost 2 eV, but also the shortest ISB scattering time: due to the strong electron optical phonon interaction and large electron effective mass of group III nitrides, it is in the sub-picosecond range [Heber et al., 2002].

The GaN/AlN system therefore opens the field of ISBT towards the near infrared; Suzuki and Iizuka [1997] conducted a theoretical feasibility study for near infrared (NIR) ISBTs in GaN QWs sandwiched between $Al_xGa_{1-x}N$ barriers, concluding that ISBT wavelengths of 1.55 μm can be realized. This prospect of fast and robust optoelectronic devices at the long haul fiber telecommunication wavelengths of 1.55 μm and 1.3 μm has recently incited the interest for ISBTs in group III nitrides.

First experiments on GaN/AlN ISBTs where carried out at Bell Labs. ISB absorptions of MBE grown samples with QW thicknesses ranging from 30 Å down to 10 Å, and $Al_xGa_{1-x}N$ barriers with an Al content between 45% and 80% were investigated by Gmachl et al. [2000a,b, 2001] and reported to cover wavelengths from 4.15 μm down to 1.41 μm. Iizuka et al. [2002] measured ISB absorptions between 2.2 μm and 1.3 μm for MBE grown GaN/AlN MQW structures. Kishino et al. [2002] showed that in theory, the shortest ISBT wavelength in a GaN QW sandwiched between AlN barriers is 1.07 μm, as the second subband comes to lie into the continuum for QWs thinner than four monolayers (one GaN ML corresponds to 2.59 Å). A systematic experimental and theoretical study on NIR ISBTs in GaN QWs was conducted by Tchernycheva et al. [2006].

Iizuka et al. [2000] observed a relaxation time around 150 ps for ISBTs at 4.5 μm. Heber et al. [2002] report a value of 370 fs at 1.55 μm. Hamazaki et al. [2005] also investigated ISBT relaxation at 1.55 μm by pump and probe experiments and reported on absorption bleaching attributed to a phase space filling of the upper subband and a carrier cooling process in the lower subband, having relaxation times of 140 fs respectively 300−400 fs. Time resolved two color pump and probe measurements in a superlattice showed spectral holes separated by the LO phonon energy (92 meV) due to the electron-LO phonon coupling [Wang et al., 2006]; a homogeneous ISBT linewidth broadening in the order of 50 meV was found.

Vertical transport in group III nitrides heterostructures was studied theoretically and experimentally by Bykhovski et al. [1995], Hermann et al. [2004], Kikuchi et al. [2002], and Golka et al. [2006]; Although some groups measured negative differential resistance (NDR), its origin is not clear as the transport is influenced by the high defect density at the interfaces.

Recently, ISB emission at 2.3 μm originating from a second harmonic generation process was observed by Nevou et al. [2007]. A quantum dot detector working at room temperature around 1.38 μm was presented by Doyennette et al. [2005]. The first QW detector was presented by Hofstetter et al. [2003].

This work focuses on light detection based on ISBT in group III nitrides heterostructures. Owing to the novelty of ISBT in nitrides, it is based on absorption and photovoltaic detection measurements of simple structures to extract elementary working principles and parameters necessary for the future development of nitride ISB photodetectors.

It was found that the photovoltaic detection scheme in those detectors is based on optical nonlinearities, namely photoinduced polarization. Sample series were investigated to identify the influence of different parameters affecting the photoinduced polarization process such as number of periods, QWs, and barriers and cap layer thicknesses.

Chapter 2 starts with an introduction into the group III nitride system. Important parameters, such as the internal fields (which are not present in GaAs or InP based system) are discussed and the relevant electrical and optical parameters are given. Chapter 3 describes the theoretical aspects used to design and analyze the structures investigated in this work. In chapter 4, the simulation of the conduction band is described. Chapter 5 contains a description of the sample preparation and used measurement setups.

In chapters 6 and 7 absorption measurements and in chapter 8 photovoltaic (PV) measurements are presented. A summary is given in chapter 9.

Chapter 2

Group III Nitrides

In the first part of this chapter, an overview of the crystalline structure of group III nitrides is given, and some electrical and optical properties are discussed. GaN is the most studied group III nitride compound, but compared to GaAs, there is still relatively little known [Strite and Morkoç, 1992]. Even for GaN material parameters, values reported in the literature can vary depending on the growth method and material quality. As for InN, a less mature group III nitride compound, researchers only recently agreed to a bandgap value of 0.7 eV [Wu et al., 2003]. The focus of this work lies on GaN, AlN and their alloys, however some optical parameters of InN are included for completeness. Boron nitride, which at the moment is not a common constituent of device fabrication, is not discussed in this work.

The second part of the chapter discusses the epitaxial growth using plasma assisted molecular beam epitaxy and metal-organic vapor-phase epitaxy.

2.1 Material properties

Although AlN, GaN and InN can exist in the cubic zincblende (β) phase, only the hexagonal wurtzite (α) phase is thermodynamically stable. In the wurtzite phase, group III nitrides form a continuous alloy system with direct bandgaps. In figure 2.1 the bandgap energies of some common semiconductors are depicted as a function of lattice constant. InGaN alloys cover the whole visible range.

The large bandgap difference of 2.72 eV (300 K) between AlN and GaN leads to a large conduction band offset which makes it possible to achieve ISBT energies of up to 1 eV. Nitride structures are usually grown on SiC-6H (silicon carbide) or Al_2O_3 (sapphire) substrates. With lattice constants a_0 of 3.0806 Å for SiC-6H respectively 2.748 Å for Al_2O_3 [Ambacher, 1998], both substrates are not lattice matched to GaN or AlN, which causes a compressive strain of the epilayer. Due to the 30° cell rotation between GaN and sapphire, an inplane lattice constant of $a_{sap}/\sqrt{3} = 4.759/\sqrt{3} = 2.748$ has to be considered for the lattice mismatch of GaN on sapphire. Recently, GaN substrates became commercially available, but they are rarely used due to their high costs and still high defect density in the range of $10^6\,\text{cm}^{-2}$.

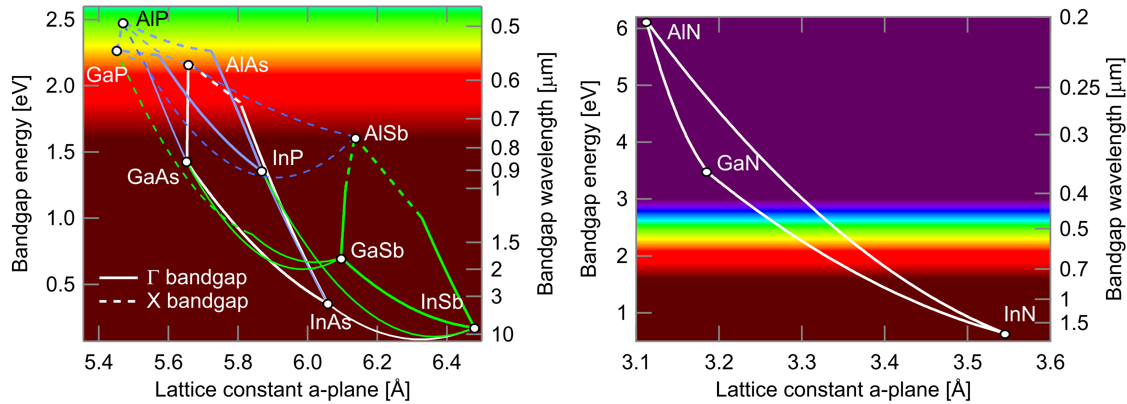

Figure 2.1: Left: bandgap versus lattice constant of common III-V semiconductor. Right: bandgap versus lattice constant for group III nitrides. Direct bandgaps are marked by a solid line, indirect by a dashed line.

2.1.1 Crystalline structure

The wurtzite crystal structure (space group $P6_3mc$) consists of alternating ABAB sequences of bilayers made of two closely spaced hexagonal layers of Ga and N atoms in the c-direction [0001], as seen in figure 2.2 on the left. The wurtzite hexagonal crystal structure of group III nitrides can be described by the edge length a_0 of the basal hexagon $[11\bar{2}0]$, the height of the hexagonal prism c_0 and the internal parameter u_0, defined as the anion-cation bond length along the [0001] axis. The ratio u_0/c_0 is a measure of the non-ideality of the actual crystal in comparison to an ideal wurtzite structure with $u_0/c_0 = 3/8 = 0.375$. As seen in the right panel of figure 2.2 showing the unit cell of GaN, u_0 and c_0 are directly related: the longer u_0 is, the greater is c_0. Thus, the ratio c_0/a_0 is another measure for the crystal non-ideality and equals $\sqrt{(8/3)} = 1.633$ for an ideal wurtzite crystal.

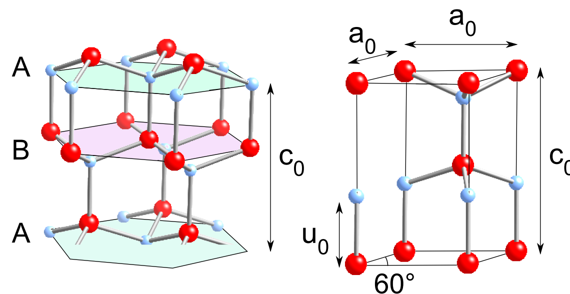

Figure 2.2: Left: hexagonal structure of wurtzite GaN with A, B bilayers. Right: wurtzite GaN unit cell. Ga-atoms are red (dark), N-atoms are blue (bright). c_0 and a_0 are the lattice constants, u_0 is the anion-cation bond length.

A wurtzite structure is asymmetric in the [0001] direction, which by convention is given by the vector pointing from the cation (Ga, Al, In) to the nearest neighbor anion (N) in positive c-direction. As seen in figure 2.3, the closely spaced bilayers {0001} are different in the [0001] and the $[000\bar{1}]$ direction. GaN has polar faces: in the [0001] direction it is

Ga-face and in the $[000\bar{1}]$ direction N-face. The terminology of Ga- or N- face should not be confounded with termination which is a surface property; a Ga-face crystal grown in the [0001] direction can be terminated with nitrogen [Ambacher, 1998]. Ga-face and N-face GaN have different chemical properties; the latter has a rougher surface [Hellman, 1998, Rouviere et al., 1997], which is also easier attacked chemically than Ga-face GaN [Gao et al., 2004]. The crystal face depends on several factors such as substrate preparation and growth conditions, as described by Sarigiannidou et al. [2006], Seelmann-Eggebert et al. [1997], Sumiya et al. [1999] and Yoshikawa and Xu [June 2002].

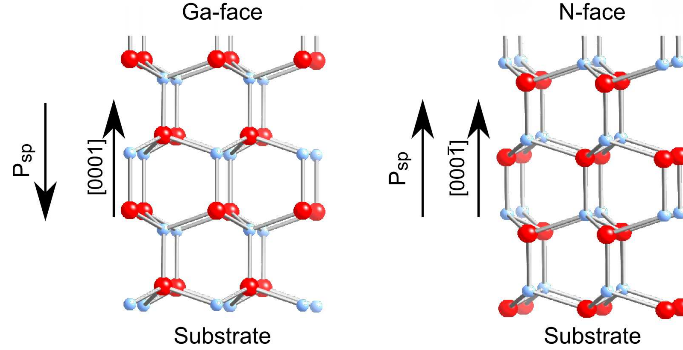

Figure 2.3: Left: Ga-face crystal in the [0001] direction. Right: N-face crystal in the $[000\bar{1}]$ direction. Ga-atoms are red (dark), N-atoms are blue (bright). P_{sp} stands for the spontaneous polarization vector discussed in section 2.1.2.

In table 2.1, parameters describing the crystal structure of group III nitrides are summarized. For $Al_xGa_{1-x}N$ alloys, the lattice constants can be linearly interpolated between

	AlN	GaN	InN	sapphire
a_0 [Å]	3.112	3.189	3.533	4.758 [1]
c_0 [Å]	4.982	5.186	5.693	12.991 [1]
c_0/a_0	1.601	1.624	1.611	—
Bond length $R_{metal-N_1} u_0$ [Å] [2]	1.892	1.949	2.156	—
u_0/c_0	0.798	0.376	0.379	—
Bohr radius a_0 [3]	5.814	6.040	6.660	—
Electron mass	$0.4\,m_0$	$0.2\,m_0$	$0.11\,m_0$	—
Monolayer thickness [Å](bulk)	—	2.5928 [4]	—	—
Optical phonon [meV]	99	91.2	73	—

Table 2.1: Wurtzite nitride parameters taken from Levinshtein et al. [2001], except [1]: Ambacher [1998], [2]: Mattila and Zunger [1999], [3]: Bernardini et al. [1997], [4]: Tchernycheva et al. [2006].

AlN and GaN as a function of the Al content x [Ambacher et al., 2000]:

$$a_0(x) = 3.189 - 0.077x \quad (2.1)$$

$$c_0(x) = 5.186 - 0.203x \quad (2.2)$$

2.1.2 Polarization in wurtzite nitride structures

In absence of an external electrical field and of any deformation due to stress, the hexagonal wurtzite phase exhibits an electrical polarization along the [0001] axis called spontaneous polarization (P_{sp}). At the microscopic scale this means that the centers of gravity of charges of opposite signs (positive for the metal atoms, negative for Nitrogen) within an unit cell do not coincide, resulting in a parallel orientation of dipoles in the [0001] directions [Zheludev, 1971]. Group III nitrides lack an inversion symmetry along the c-axis and are therefore polar crystals; hence, they are pyroelectric. Pyroelectric phenomena are associated with a change of P_{sp} due to a change in temperature. For AlN, the change of P_{sp} with temperature is $P_{sp}/dT = 7.5\mu C/K/m^2$; this comparably small value is an advantage for high power and high-temperature applications [Ambacher et al., 2002]. In this work, P_{sp} is considered to be temperature independent. As seen in figure 2.3, P_{sp} points from the N- to the Ga-atom and is therefore negative for Ga- and Al-face and positive for N-face crystals. The magnitude of P_{sp} depends on the non-ideality of the crystal (ratio u_0/c_0) and increases from GaN to InN to AlN. The spontaneous polarization in C/m^2 for the $Al_xGa_{1-x}N$ alloy as function of the Al content x can be approximated by [Ambacher et al., 2002]:

$$P_{spAlGaN}(x) = -0.090x - 0.034(1-x) + 0.021x(1-x). \quad (2.3)$$

Because a pyroelectric crystal has neither a center of symmetry nor a rotation axis, or at most a single rotation axis that is no inversion axis, all pyroelectrics are also piezoelectric; the inverse is not true. Wurtzite group III nitrides exhibit an additional piezoelectric polarization P_{piezo} when stress is applied. As GaN, AlN, and InN all have different lattice constants and are not lattice matched to the sapphire substrate, strain induced piezoelectric polarization occurs in almost all group III nitride heterostructures; it is up to ten times larger than in other III-V compounds [Bernardini et al., 1997].

Just like in a dielectric, where the electric polarization is related to the electric field via the susceptibility, the polarization charge per unit area in a crystal $P_{piezo,i} = d_{ijk}\sigma_{jk}$ (specified in three components) is linearly related to all components of a general stress σ_{ij} (specified by a second-rank tensor with nine components) via the piezoelectric moduli d_{ijk} (27 components). Using the symmetry relation between the piezoelectric moduli (based on the crystallographic point group), a reduction of the independent piezoelectric moduli can be achieved. Hooke's law states that for small stresses, the amount of strain is proportional to the magnitude of the applied stress, so the deformation of a crystal ϵ_{kl} due to stress σ_i can be described by $\sigma_i = C_{ij}\epsilon_j$, where the stiffness or elastic constant C_{ij} is a 6×6 matrix for the wurtzite structure. The biaxial strain (deformation in z direction) is $\epsilon_z = (c - c_0)/c_0$ and the deformation in the plane $\epsilon_x = \epsilon_y = (a - a_0)/a_0$, where a_0 and c_0 are the unstrained lattice parameters. An elaborated theory is presented in general by Nye [1976] and specifically for group III nitrides by Ambacher et al. [2002].

Often the piezoelectric constants $e_{kl} = d_{kj}C_{jl}$ and not the piezoelectric moduli d_{kj} are used to describe piezoelectric properties of group III nitrides. Due to the symmetry of the wurtzite crystal, there are only three independent piezoelectric constants e_{33}, e_{31} and e_{15}; e_{15} is caused by shear stress and is not further discussed, since P_{piezo} is not related to it.

With

$$e_{31} = (C_{11} + C_{12})d_{31} + C_{13}d_{33} \quad (2.4)$$
$$e_{33} = 2C_{13}d_{31} + C_{33}d_{33} \quad (2.5)$$

the piezoelectric polarization can be written as

$$P_{piezo} = e_{33}\epsilon_z + e_{31}(\epsilon_x + \epsilon_y). \quad (2.6)$$

For biaxial strain, the use of the elastic constants C_{13} and C_{33} leads to

$$\frac{c - c_0}{c_0} = -2\frac{C_{13}}{C_{33}}\frac{a - a_0}{a_0}, \quad (2.7)$$

and therefore

$$P_{piezo} = 2\frac{a - a_0}{a_0}(e_{31} - e_{33}\frac{C_{13}}{C_{33}}) \quad (2.8)$$

for the wurtzite phase.

In table 2.2 the parameters used in the calculation for P_{piezo} and values for P_{sp} are listed; those values were taken from Vurgaftman and Meyer [2003], nevertheless there is still a discussion going on about the exact values.

	AlN	GaN	InN
P_{sp} [C/m^2]	-0.090	-0.034	-0.042
d_{31} [pm/V]	-2.1	-1.6	-3.5
d_{33} [pm/V]	5.4	3.1	7.6
e_{31} [C/m^2]	-0.536	-0.527	-0.484
e_{33} [C/m^2]	1.561	0.895	1.058
C_{11} [GPa]	396	390	223
C_{12} [GPa]	137	145	115
C_{13} [GPa]	108	106	92
C_{33} [GPa]	373	398	224

Table 2.2: Spontaneous polarization P_{sp}, piezoelectric moduli d_{kj}, piezoelectric constants e_{kl}, and elastic constants C_{jl} for GaN, AlN, and InN [Vurgaftman and Meyer, 2003].

The left panel of Figure 2.4 shows the spontaneous polarization P_{sp} of $Al_{1-x}Ga_xN$ along with the computed piezoelectric polarization for a pseudomorphically grown GaN (respectively AlN) layer on an $Al_xGa_{1-x}N$ layer as a function of the lattice constant a_0 of the $Al_{1-x}Ga_xN$ buffer. Pseudomorph stands here for a layer grown with the lattice constant a of the underlying layer.

Due to the larger lattice constant of GaN in comparison to AlN, GaN grown pseudomorphically on AlN is compressively strained, whereas AlN grown pseudomorphically on GaN is tensile strained, see also figure 2.4 to the right. P_{sp} remains negative for all Al-contents x; P_{piezo} is always positive for a GaN (tensile strain) and negative for an AlN layer (compressive strain). The magnitude of P_{piezo} increases with strain, and is thus a function of the lattice mismatch. For an N-face crystal, both the spontaneous and the

piezoelectric polarization vectors have the opposite direction compared to a Ga-face crystal. Computed values of P_{piezo} are 0.037 Cm^{-2} for a fully strained GaN layer on relaxed AlN, and -0.049 Cm^{-2} for AlN on GaN. The spontaneous polarization P_{sp} is lowest for GaN, higher for InN and highest for AlN.

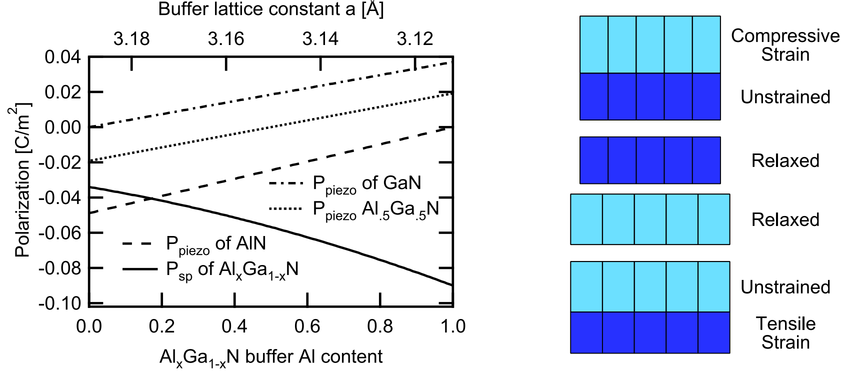

Figure 2.4: Left: P_{piezo} for a strained GaN respectively AlN layer and P_{sp} for an $Al_xGa_{1-x}N$ layer. Right: sketch of a pseudomorphically grown layer under compressive strain (top panel) and tensile strain (bottom panel).

The dashed line in figure 2.4 depicts the linear interpolation of P_{piezo} for ternary $Al_{0.5}Ga_{0.5}N$ calculated using

$$P_{piezo}^{AlGaN/AlN}(x) = 0.026(1-x) + 0.0248x(1-x) \tag{2.9}$$

$$P_{piezo}^{AlGaN/GaN}(x) = -0.0525x + 0.0282x(1-x), \tag{2.10}$$

where x is the Al concentration [Ambacher et al., 2002]. Calculations for the piezoelectric and elastic constant for ternary alloys are found in Ambacher et al. [1999].

The different polarizations in adjacent layers induce a fixed charge density at the interfaces. Those polarization induced interface charges can be estimated as follows. The charge density ρ_P associated with the divergence of the polarization in space is

$$\rho_P = -\nabla P. \tag{2.11}$$

For homogeneous top/bottom layers, P is constant in the layers and has a discontinuity at the interface where the fixed two dimensional polarization charge density σ is found. For an area S, the charge $\sigma \times S$ can thus be calculated using Gauss' theorem:

$$\sigma \times S = \int_V \rho_P dv = -\int_V \nabla P dv = -\oint_S P dS = (|P_{top}| - |P_{bottom}|) \times S \tag{2.12}$$

Again assuming an abrupt interface and homogeneous layers, the total bound interface charge density is given by

$$\sigma = |P_{top}| - |P_{bottom}| = |P_{piezo}^{top} + P_{sp}^{top}| - |P_{piezo}^{bottom} + P_{sp}^{bottom}|. \tag{2.13}$$

For Ga-face $Al_xGa_{1-x}N$/GaN heterostructures σ is positive [Ambacher et al., 2002].

In n-type heterostructures, free electrons will compensate the positive σ (for example during the cooling process after growth). Those electrons form a two dimensional electron gas (2DEG) localized in a $3-4\,\text{Å}$ wide interface region [Bernardini and Fiorentini, 2000]. For a gap-state-free interface the maximal sheet carrier density of the 2DEG is σ/e, where e is the electron charge; even for non-intentionally doped structures it is about $10^{13}\,\text{cm}^{-2}$.

Figure 2.5 gives an overview of the different strain states of an AlN/ GaN heterostructure grown metal faced. If the polarization induced sheet carrier density σ is positive, as for AlN on GaN (panels a, b, c), free electrons are accumulated at this interface and a 2DEG is formed. If on the other hand σ is negative, as is the case for GaN on AlN (panels d, e, f) free electrons will move away from the interface and holes will accumulate at the interface. As stated before, P_{sp} is always negative as opposed to P_{piezo} which is negative for compressive and positive for tensile strain, wherefore both polarizations enhance each other in a strained AlN layer and attenuate one another in a strained GaN layer. Panels c and f depict the case of a strain compensated AlN/GaN MQW structure grown on an $Al_xGa_{1-x}N$ buffer, with x corresponding to the overall Al content of the MQWs; each layer in the SL is strained in comparison to the $Al_xGa_{1-x}N$ layer.

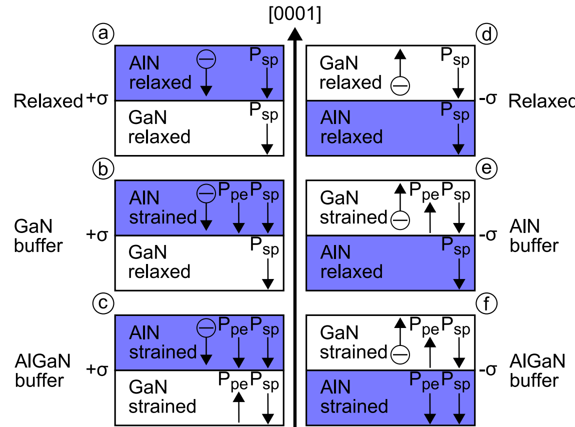

Figure 2.5: Internal polarization in heterostructures; the direction, where the electrons will move to are indicated by an arrow. Left: AlN grown on GaN (a,b,c); a 2DEG forms at the interface. Right: GaN grown on AlN (d,e,f); a two-dimensional hole gas forms at the interface. Except for panels a and d, both layers are pseudomorphically strained to the buffer material.

The internal electric field due the internal polarizations is $F_{int} = P_{tot}/\epsilon_0\epsilon_r$, where ϵ_r is the static dielectric constant and P_{tot} the sum of P_{piezo} and P_{sp} in the particular layer [Bernardini and Fiorentini, 1998]. Those combined polarization effects lead to huge built-in electrostatic fields and affect the optical and electrical properties of multi-layered nitride structures, for example by inducing a quantum confined Stark effect [Fiorentini et al., 1999]

P_{piezo} is a function of strain; the grade of relaxation however depends on the composition and the thickness of the strained layer [Bykhovski et al., 1997, Einfeldt et al., 2001]. In general, a tensile strained AlN layer will relax sooner than a compressively strained GaN layer of the same thickness. P_{piezo} and therefore σ is not a linear function of the strain; an approximation based on experimental results is found in Ambacher et al. [2000].

For calculations in this work, layers are assumed to be pseudomorphically strained if not otherwise stated.

2.1.3 Electrical and optical parameters

Wurtzite phase AlN, GaN, and InN are direct bandgap semiconductors: their conduction band minima lie in the Γ valley. The direct bandgap energy of GaN was already measured in the seventies by Monemar [1974] and by Dingle et al. [1971]. For AlN it was measured by Yim et al. [1973] or Perry and Rutz [1978] in the seventies and later by Brunner et al. [1997]. Several groups have calculated the bandstructure of nitrides, for example Christensen and Gorczyca [1994] and Suzuki et al. [1995]. As already mentioned, there is still a discrepancy in the literature concerning some material parameters.

The temperature dependence of the bandgap energy E_g can be approximated by the Varshni formula

$$E_g(T) = E_g(0) - \frac{\alpha T^2}{T + \beta} \tag{2.14}$$

using the Varshni coefficients α and β [Vurgaftman and Meyer, 2003].

Table 2.3 lists the Γ valley bandgap energy at 0 K and the Varshni parameters of AlN, GaN, and InN. At room temperature, the indirect bandgap energies relative to the Γ valley valence band maximum are E_{ML} =4.5–5.3 eV and E_A=4.7–5.5 eV for GaN, and E_{ML} =6.9 eV and E_k=7.2 eV for AlN.

The Γ valley bandgap energy for $Al_{1-x}Ga_xN$ can be approximated by a parabolic dependency upon the Al content x [Vurgaftman and Meyer, 2003]:

$$E_g(x) = (1 - x)E_g(GaN) + xE_g(AlN) - x(1 - x)b \tag{2.15}$$

where the values of the bowing parameter b found in literature vary from 0.53 to 1.5 eV [Vurgaftman and Meyer, 2003]. Recently, Buchheim et al. [2005] reported a value of 0.9 eV. An investigation on the influence of biaxial and uniaxial strain on the optical bandgap is found in Wagner and Bechstedt [2002].

There is still some incertitude about the value of the band offset at a GaN/AlN heterostructure. Bernardini and Fiorentini [1998] calculated the type I valence band offset (VBO) as function of strain for an AlN layer strained on GaN, and for a GaN layer strained on AlN. In the first case they found a VBO of 0.2 eV (leading to a CBO of 2.54 eV at 0 K) and in the second case a VBO of 0.85 eV (CBO of 1.89 eV). A detailed experimental study of ISB absorption in GaN/AlN SL was conducted by Tchernycheva et al. [2006], where a CBO of 1.65 – 1.75 eV resulted in the best fit to the measured data.

	GaN	AlN	InN
E_g (0 K / 300 K) [eV]	3.510 / 3.438	6.250 / 6.158	0.78 / 0.586
α [meV/K]	0.909	1.799	1.994
β [K]	830	1462	624
e^- affinity χ [eV]	4.1 [1]	2.1±0.3 [2]	-

Table 2.3: Bandgap parameters taken from Vurgaftman and Meyer [2003], except for [1]: Pearton et al. [1999], [2]: Wu et al. [1998].

In this work most GaN/AlN MQW structures were assumed to be strained to the AlN buffer. For conduction band simulations, a CBO of 1.9 eV, was used, which is also nearly consistent with the electron affinities listed in table 2.3.

The ideal wurtzite crystal is an optically anisotropic uniaxial crystal: the ordinary ($\boldsymbol{E} \perp c$) dielectric function $\epsilon_x = \epsilon_y = \epsilon_o$ differs from the extraordinary ($\boldsymbol{E} \parallel c$) dielectric function $\epsilon_z = \epsilon_e$, where c corresponds to the growth direction which is parallel to [0001]. The dielectric function was among others studied by Buchheim et al. [2005] and Wagner and Bechstedt [2002]. Brunner et al. [1997] and Yu et al. [1997] have studied the refractive index close to the absorption edge for $Al_xGa_{1-x}N$ and GaN.

In this work, most of the optical characterization was done in the wavelength range of 1.3 µm–2 µm, where for bulk material the investigated crystals are transparent and the imaginary part of $\epsilon(\omega)$ is zero.

	$\epsilon_o(0)$	$\epsilon_o(\infty)$	$\epsilon_e(0)$	$\epsilon_e(\infty)$	n
GaN	9.28	5.18	10.2	5.31	2.3-2.335
AlN	7.76	4.160	9.32	4.35	2.03-2.15

Table 2.4: Experimentally obtained dielectric constants taken from Moore et al. [2005] for AlN and from Shokhovets et al. [2003] and Azuhata et al. [1995] for GaN; refractive indices were taken from Hui et al. [2003a], Levinshtein et al. [2001].

The refractive index for $Al_xGa_{1-x}N$ layers with different Al concentration was measured by Hui et al. [2003a] at 1.5 µm; it can be expressed by

$$n(1500nm) = 0.431x^2 - 0.735x + 2.335. \tag{2.16}$$

In analogy to the dielectric functions, the refractive indices are different for optical fields perpendicular and parallel to the c-axis. Hui et al. [2003b] found an index difference of $n_e - n_o = 2.357 - 2.315 = 0.042$.

The refractive indices of sapphire at 1.55 µm are $n_o = 1.74618$ and $n_e = 1.73838$ [int, b].

2.2 Growth

Today, most nitride based commercial optoelectronic devices are grown by metal-organic vapor-phase epitaxy (MOVPE). However, for structures with layer thickness of a few MLs, molecular-beam epitaxy (MBE) is advantageous due to the lower growth temperature, which produces more abrupt interfaces than MOVPE. The samples investigated in this work were synthesized either by plasma-assisted molecular-beam epitaxy (PAMBE) or by MOVPE. Typical growth rates for MOVPE are in the range of 2 µm/h for GaN. In the case of PAMBE, the maximum growth rate (limited by the activation rate of the nitrogen plasma) is about 1 µm/h.

The substrate for both epitaxies was sapphire. The lattice mismatch of GaN (16%) and AlN (13.5%) towards sapphire results in a high dislocation density of the order of 10^9 cm^{-2}. Figure 2.6 shows the in-plane arrangement of an AlN layer on sapphire. Due to the cell rotation a reduced sapphire lattice constant $a_{sap}/\sqrt{3} = 2.748$ is used for the calculation of the lattice mismatch.

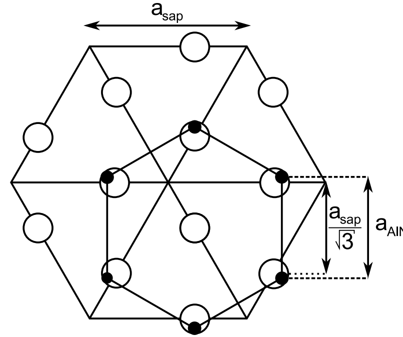

Figure 2.6: Schematic representation of the in-plane atomic arangement in the case of a (0001) AlN film grown on c plane sapphire [Jain et al., 2000]. Black: III-plane of AlN, white: O-plane of sapphire

To reduce the high defect density, either a thick GaN or AlN layer is deposited first by MOVPE on the sapphire, serving as pseudo substrate. Most MOVPE samples investigated were grown on a thick GaN buffer deposited on a sapphire substrate, whereas for PAMBE samples AlN on sapphire templates were used. For the MOVPE samples with GaN pseudo substrates, strained epilayers containing Al are thus under tensile stress. For PAMBE samples with AlN pseudo substrates, strained epilayers containing Ga are under compressive stress. As the overall Al content of the investigated epilayers is generally higher than the Ga content and strained layers crack easier under tensile stress than under compressive stress, PAMBE samples seldom cracked.

As already discussed, group III nitrides can be grown in both metal or nitrogen face. MOVPE grown GaN layers grown on sapphire are always Ga face. In the case of PAMBE, the layer polarity can be chosen by varying the growth conditions of the buffer layer. In general, MQW structures with Ga polarity present a lower interface roughness than their N polarity counterparts [Sarigiannidou et al., 2006]. All samples investigated in this work are Ga-faced.

Despite the recent substantial progress in the growth of group III nitrides, there are still difficulties remaining, for example the high background doping of GaN or the feasibility of doping $Al_xGa_{1-x}N$ layers with high Al content: the doping efficiency of donors and acceptors decreases drastically as the Al content and band gap of $Al_xGa_{1-x}N$ increases. The ionization energy of Si in $Al_xGa_{1-x}N$ increases from 20 meV to 54 meV between 0% and 20% Al content [Jain et al., 2000]. Zhang [2002] investigated the microscopic origin of the doping limits in wide gap semiconductor. A high doping level of $2\times10^{19}\,\mathrm{cm}^{-3}$ in GaN gives an electron concentration that is independent of the temperature [Gotz et al., 1996b]. For the structures studied in this work, GaN layers are Si doped to $1 - 10 \times 10^{19}\,\mathrm{cm}^{-3}$, wherefore all donor electrons can be assumed to be active.

2.2.1 Plasma assisted molecular beam epitaxy

All PAMBE samples were grown at CEA in Grenoble. The growth chamber is equipped with standard effusion cells for Ga, Al, In and Si; active nitrogen was provided by an RF cell.

PAMBE growth of group III nitride layers is based on the use of a metal excess that

segregates on the growing surface and decreases the surface energy of the (0001) layer. This excess metal is denoted 'surfactant' since it changes the energetic equilibrium at the growing surface without modifying the composition of the material. Growing very thin layers of GaN and AlN (the samples investigated in this work have layer thicknesses of 7.5 Å– 150 Å) requires a good control of the interface and also an optimization of the growth conditions for both materials.

GaN Due to the smaller Ga-N binding energy, GaN has a lower decomposition temperature than AlN. It is crucial to determine growth conditions compatible with both AlN and GaN to optimize the GaN/AlN interface. The best GaN structural quality is achieved under GaN-rich conditions with two ML of Ga excess segregating at the growth front [Adelmann et al., 2003]. There is a broad growth window where two ML of GaN are dynamically stable on the growth front at temperatures between 700 an 750°C where Ga desorption is active. However, even within this window, the quality of the GaN/AlN was found to be particularly sensitive to the Ga/N ratio. The strain fluctuation induced by Si doping and by the presence of AlN barriers favors the formation of V-shaped pits, even in layers grown with two ML Ga-excess [Hermann et al., 2004, Nakamura et al., 2002]. The suppression of these defects can be achieved by an enhancement of Ga flux so that growth is performed at the limit of Ga accumulation.

AlN A two-dimensional growth of AlN is achieved under Al rich conditions. However, Al is not desorbed from the surface at the standard growth temperatures for GaN (700–750°C). To prevent Al accumulation at the surface, the growth is interrupted periodically under nitrogen. Alternatively to growth interruptions, Ga can be used as a surfactant for the growth of AlN, with the Al flux corresponding to the Al/N stoichiometry and an additional Ga flux to stabilize the surface. Since the Al-N binding energy is much higher than the Ga-N binding energy, Ga segregates on the surface and it is not incorporated into the AlN layer. The lowest interface roughness has been achieved by using Ga as a surfactant during the growth of AlN without growth interruptions [Sarigiannidou et al., 2006].

On the other hand, while analyzing the quality of the GaN/AlN interface it was observed that overgrowth of GaN QWs with AlN at high temperatures results in an irregular thinning of the QW thickness due to the exchange of Ga atoms in the GaN layer with Al [Gogneau et al., 2004]. This process is thermally activated and limits the growth to temperatures below 720°C.

In conclusion, best interface results were achieved at a substrate temperature of 720°C, growing AlN at the Al/N stoichiometry without growth interruptions and using Ga as a surfactant during the growth of AlN barriers. Under these conditions, the samples present a flat surface morphology with an rms surface roughness of 1.0–1.5 nm, measured in an area of 5×5 μm^2. Furthermore, high-resolution transmission electron microscopy (HRTEM) showed homogeneous QWs with an interface roughness of about 1 ML [Sarigiannidou et al., 2006].

Figures 2.7 and 2.8 show atomic force microscopy (AFM) surface images of GaN / AlN SLs grown on GaN and AlN templates by PAMBE. In both cases the rms surface

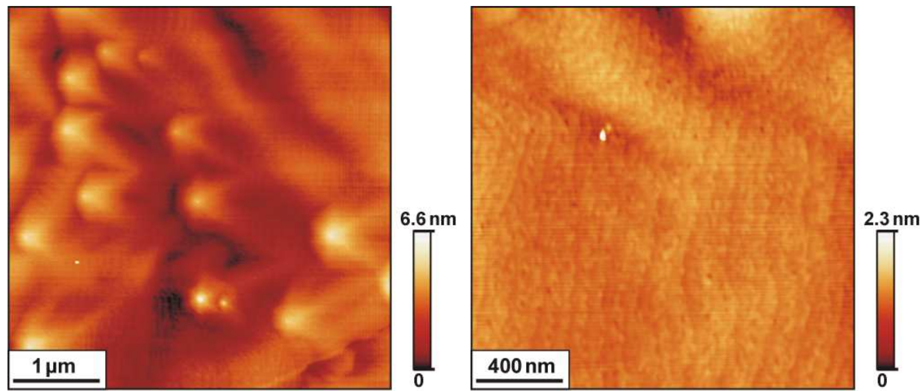

Figure 2.7: AFM of sample E890 grown on a GaN buffer; the right panel shows a magnification.

roughness remains around 1 nm in a surface of $5\times5\ \mu m^2$. The samples present the characteristic surface of GaN layers, with atomic terraces and spiral hillocks. The hillock density is systematically higher in the samples grown on AlN templates, which indicates a higher density of screw dislocations. Figure 2.8 to the right shows the TEM image of a sample grown on an AlN on sapphire template. The MQW region consists of five periods with 15 Å QW and 15 Å thick AlN barriers.

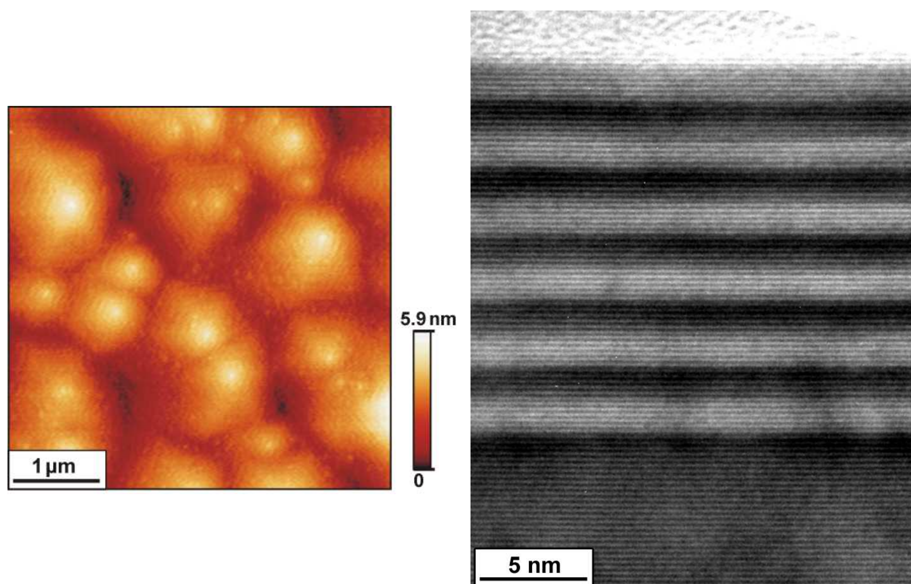

Figure 2.8: Left: AFM of sample E888 grown on AlN substrate. Right: TEM image of a five period SL sample grown on an AlN buffer (E882).

In order to reduce the defect density and the piezoelectric polarization, it is interesting to grow the GaN/AlN SL sandwiched between $Al_xGa_{1-x}N$ layers with an Al mole fraction close to the average Al content of the SL. The difficulty in growing thick $Al_xGa_{1-x}N$

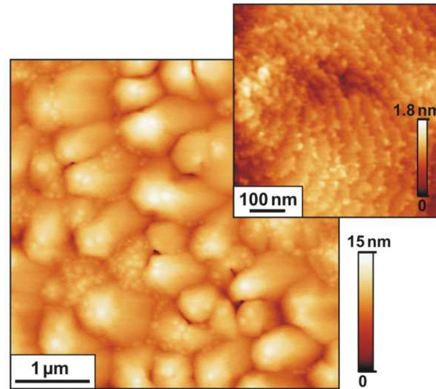

Figure 2.9: AFM of sample E740 grown on an $Al_{0.35}Ga_{0.65}N$ buffer layer; the inset shows a magnification.

layers (>20 nm) lies in the smaller surface mobility of AlN as compared to GaN. For an Al mole fraction smaller than 35% the growth can be performed under Ga-rich condition without deterioration of the surface morphology and crystalline quality. For the growth of $Al_xGa_{1-x}N$ with more than 50% Al, a deterioration of the surface morphology when growing under Ga excess is observed. In order to maintain a good crystalline quality, the substrate temperature is reduced to about 680°C, the Ga flux is reduced and an additional flux of In is used as a surfactant. In is not incorporated in the layers if the grown temperature is kept higher than 650°C. Figure 2.9 shows AFM images of the surface of an SL grown and capped with $Al_{0.35}Ga_{0.65}N$ layers. The rms surface roughness is 1.7 nm. In the magnified image, atomic-step terraces are observed.

2.2.2 Metal-organic vapor-phase epitaxy

The metal-organic vapor-phase epitaxy (MOVPE) samples investigated in this work were grown at EPF Lausanne. Growth was carried out in an AIXTRON 200/RF-S MOVPE reactor on 2" c-plane sapphire substrates. The growth usually started with the deposition of a 2 µm thick GaN buffer or pseudo-substrate layer grown at 1075° C. The active region, a GaN/AlN SL, was then deposited at low temperature (885-935° C). Using In as a surfactant leads to a general improvement of the crystalline structure [Nicolay et al., 2006] while only a small amount (< 2%) is incorporated into AlN barriers; therefore, some of the investigated samples have $Al_{0.98}In_{0.02}N$ barriers.

One difficulty of MOVPE AlN growth is the high reactivity of Al with ammonia: they already react before reaching the substrate, complicating the growth of thick AlN layers. Nevertheless AlN on sapphire pseudo substrates are commercially available. They are normally grown in specific reactors at a higher temperature and slower growth rate than normally used in MOVPE.

As experiments showed, the interface quality for an SL grown pseudomorphically on GaN is inferior to an SL grown strained on AlN. So the later MOVPE structures studied in this work were grown on AlN pseudo substrates [Nicolay et al., 2007].

2.2.3 Dislocations and defects

Despite of the continuous progress in nitride growth technology, group III nitride structures still have a high defect density in the range of $10^9\,\text{cm}^{-2}$. Dislocations and defects are formed due to lattice mismatch. Figure 2.10 shows a TEM measurement of a sample grown on sapphire. It is seen that threading dislocations formed in the AlN buffer layer

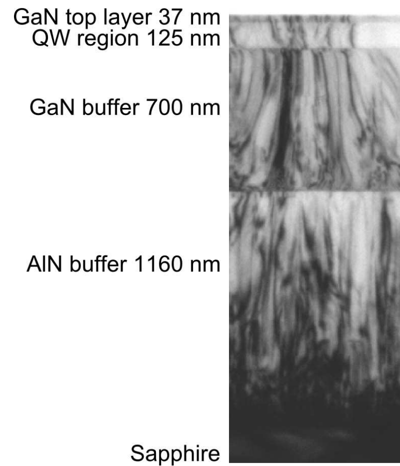

Figure 2.10: TEM image of a sample grown on sapphire substrate

and in the GaN layer cross the QW region and terminate at the free surface.

Many groups have studied different types of defects both theoretically, for example Van de Walle and Neugebauer [2004], and experimentally by deep level transient spectroscopy, for example Gotz et al. [1994, 1996a] or Pearton et al. [1999]. Defects manifest themselves also in the photoluminescence at various energies [Reshchikov and Morkoc, 2005]. In the photovoltaic measurements presented in this work, the signature of various defects was observed as well, however no thorough investigation of their nature was carried out.

Chapter 3

Theoretical Background

In this chapter the relevant basic physic principles concerning discrete states in a confined potential are given. The second part deals with nonlinear phenomena in optics.

3.1 Electron wavefunctions in quantum wells

Intersubband photodetectors are based on ISB absorption in a QW. Thus, the ISB absorption coefficient in a single-particle, one band model is discussed using Fermi's golden rule; a more detailed discussion can be found in Helm [2000], Kittel [1996], Schwabl [1998], Sze [1981], or Bastard [1988].

3.1.1 Schrödinger equation

The Schrödinger equation describes the space- and time-dependence of quantum-mechanical systems.

According to the correspondence principle, physical quantities are assigned to operators in quantum mechanics [Schwabl, 1998]. This results in the following assignments:

$$\text{Momentum } \boldsymbol{p} \longrightarrow \frac{\hbar}{i}\nabla \tag{3.1}$$

$$\text{Energy } E \longrightarrow i\hbar\frac{\partial}{\partial t}\,. \tag{3.2}$$

Applying the correspondence principle to the Hamiltonian of a particle in a potential $V(\boldsymbol{r})$ and taking into account that the state of a quantum mechanical system is described by a wave function $\psi(\boldsymbol{r},t)$ results in

$$E = \frac{\boldsymbol{p}^2}{2m} + V(\boldsymbol{r}) \longrightarrow i\hbar\frac{\partial}{\partial t}\psi(\boldsymbol{r},t) = \left(-\frac{\hbar^2}{2m}\nabla^2 + V(\boldsymbol{r})\right)\psi(\boldsymbol{r},t)\,. \tag{3.3}$$

This is the Schrödinger equation

$$i\hbar\frac{\partial}{\partial t}\psi(\boldsymbol{r},t) = H\psi(\boldsymbol{r},t) \tag{3.4}$$

$$H = -\frac{\hbar^2}{2m}\nabla^2 + V(\boldsymbol{r})\,, \tag{3.5}$$

where H is the Hamiltonian. Provided that H is time independent, the wavefunction can be separated in a space-independent and a time-independent part: $\psi(\boldsymbol{r},t) = f(t)\psi(\boldsymbol{r})$. This leads to the time-independent Schrödinger equation

$$H\psi(\boldsymbol{r}) = E\psi(\boldsymbol{r}) \tag{3.6}$$

which is an eigenvalue equation with eigenstates $\psi(\boldsymbol{r})$ and eigenvalues E.

3.1.2 The envelope function model

According to the Bloch theorem, the total electron wave function $\psi(\boldsymbol{r},t)$ at the Γ point (center of the Brillouin zone) is the product of a Bloch function $u_\nu(\boldsymbol{r})$ varying on the scale of the host material's crystalline periodicity and an envelope function $f_n(\boldsymbol{r})$ which is a plane wave varying slowly compared to $u_\nu(\boldsymbol{r})$:

$$\psi_n(\boldsymbol{r},t) = f_n(\boldsymbol{r})u_\nu(\boldsymbol{r})\exp(-i\frac{E_n t}{\hbar}), \tag{3.7}$$

where n is the quantum number, E_n the energy eigenvalue and $f_n(\boldsymbol{r})$ the envelope function, which depends on the QW potential and externally applied fields. Considering that the Hamiltonian is time independent and assuming that the lattice-periodic Bloch function $u_\nu(\boldsymbol{r})$ remains the same in the QW as well as in the barrier material, the solution to the Schrödinger equation reduces to the envelope function $f_n(\boldsymbol{r})$. For a free motion in x and y direction (with z being the growth direction), where $\boldsymbol{k} = (k_x, k_y, 0)$ and $V(\boldsymbol{r}) = V(z)$, the envelope function can be separated:

$$f_{n\boldsymbol{k}}(\boldsymbol{r}) = \frac{1}{\sqrt{A}}e^{i\boldsymbol{kr}}\phi_n(z) \tag{3.8}$$

where A is the sample area. Inserting equation (3.8) in equation (3.6) leads to the one-dimensional time-independent Schrödinger equation

$$\begin{aligned}\frac{-\hbar^2}{2m^*}\phi_n(z)\left(\frac{d^2}{dx^2}+\frac{d^2}{dy^2}\right)e^{i\boldsymbol{kr}} + \frac{-\hbar^2}{2m^*}e^{i\boldsymbol{kr}}\frac{d^2}{dz^2}\phi_n(z) + e^{i\boldsymbol{kr}}V(z)\phi_n(z) \\ = E_{n,\boldsymbol{k}}e^{i\boldsymbol{kr}}\phi_n(z).\end{aligned} \tag{3.9}$$

Along the z axis, (3.9) becomes

$$-\frac{\hbar}{2m^*}\frac{d^2}{dz^2}\phi_n(z) + V(z)\phi_n(z) = E_n\phi_n(z). \tag{3.10}$$

For a minimum in the dispersion relation, the total eigenenergy for a free particle in the $x-y$ plane is quadratic in $\boldsymbol{k}$:

$$E(n,\boldsymbol{k}) = E_n + \frac{\hbar^2\boldsymbol{k}^2}{2m^*} \tag{3.11}$$

where m^* stands for the effective mass and the subband energies E_n depend on the potential $V(z)$. In samples consisting of thin films of different materials A respectively B,

(3.10) needs to be solved for each material and the boundary conditions at the interface $z = z_{AB}$,

$$\phi_n^A(z_{AB}) = \phi_n^B(z_{AB}) \quad \text{and} \quad \frac{1}{m^{*A}}\frac{d\phi_n^A}{dz}(z_{AB}) = \frac{1}{m^{*B}}\frac{d\phi_n^B}{dz}(z_{AB}), \tag{3.12}$$

must be fulfilled: the wavefunction has to be continuous and the probability current needs to be conserved across the interface. For the simple case of a symmetric finite single QW, (3.9) can be solved analytically. For most real structures, however, no analytical solution exists and ϕ_n and E_n are obtained by numerical simulation.

3.1.3 Intersubband absorption coefficient of a single quantum well

In a two dimensional system with discrete energy states where only the ground state is occupied, the transition rate W_{if} from the ground state $|\psi_i\rangle$ to a final state $|\psi_f\rangle$ under the influence of an external electromagnetic wave with frequency ω is given by Fermi's golden rule:

$$W_{if} = \frac{2\pi}{\hbar}|\langle\psi_i|H'|\psi_f\rangle|^2\delta(E_f - E_i - \hbar\omega), \tag{3.13}$$

where $H' = \frac{e}{2m^*}(\boldsymbol{A}\cdot\boldsymbol{p} + \boldsymbol{p}\cdot\boldsymbol{A})$ is the interaction Hamiltonian and m^* the effective mass based on the one-band effective-mass model. $\boldsymbol{A}$ is the vector potential of the electric field $\boldsymbol{E}$ which is described by a plane electromagnetic wave with an amplitude E_0:

$$\boldsymbol{E}(\boldsymbol{r},t) = E_0\boldsymbol{e}\cos(\boldsymbol{q}\cdot\boldsymbol{r} - \omega t) = \frac{E_0\boldsymbol{e}}{2}\left(e^{i(\boldsymbol{q}\cdot\boldsymbol{r}-\omega t)} + e^{-i(\boldsymbol{q}\cdot\boldsymbol{r}-\omega t)}\right), \tag{3.14}$$

where $\boldsymbol{q}$ is the propagation vector, and $\boldsymbol{e}$ the linear polarization vector perpendicular to $\boldsymbol{q}$. Using $\boldsymbol{E} = \frac{-\partial\boldsymbol{A}}{\partial t}$ leads to

$$\boldsymbol{A}(\boldsymbol{r},t) = \frac{E_0\boldsymbol{e}}{\omega}\sin(\boldsymbol{q}\cdot\boldsymbol{r} - \omega t) = \frac{iE_0\boldsymbol{e}}{2\omega}e^{i(\boldsymbol{q}\cdot\boldsymbol{r}-\omega t)} + \text{c.c.}\ . \tag{3.15}$$

If the characteristic length of the electronic system is much smaller than the wavelength of the radiation, H' can be simplified using the dipole approximation: $\boldsymbol{A}$ and $\boldsymbol{p}$ commute, resulting in $H' = \frac{e}{m^*}\boldsymbol{A}\cdot\boldsymbol{p}$. For ISBTs, this condition is almost always met; the QWs studied in this work have thicknesses of 10–20 Å whereas the wavelength of the radiation is 1-2 µm. Therefore, (3.13) can be rewritten as

$$W_{if} = \frac{2\pi}{\hbar}\frac{e^2E_0^2}{4m^{*2}\omega^2}|\langle\psi_i|\boldsymbol{e}\cdot\boldsymbol{p}|\psi_f\rangle|^2\delta(E_f - E_i - \hbar\omega). \tag{3.16}$$

Using (3.7), the matrix element $\langle\psi_i|\boldsymbol{e}\cdot\boldsymbol{p}|\psi_f\rangle$ can be split in two parts due to the significantly slower variation of the envelope function f_n as compared to the Bloch function u_ν:

$$\langle\psi_i|\boldsymbol{e}\cdot\boldsymbol{p}|\psi_f\rangle = \boldsymbol{e}\cdot\langle u_\nu|\boldsymbol{p}|u_{\nu'}\rangle\langle f_n|f_{n'}\rangle + \boldsymbol{e}\cdot\langle u_\nu|u_{\nu'}\rangle\langle f_n|\boldsymbol{p}|f_{n'}\rangle \tag{3.17}$$

If the initial and final state lie in different bands ($\nu \neq \nu'$), the overlap integral of the Bloch function $\langle u_\nu|u_{\nu'}\rangle$ vanishes and only the first term remains. It therefore describes interband transitions, whose dipole matrix elements $\langle u_\nu|\boldsymbol{p}|u_{\nu'}\rangle$ are built on the Bloch functions [Rosencher and Vinter, 1998]. If the initial and final states lie in the same band

($\nu = \nu'$), the first term vanishes and $\langle u_\nu | u_{\nu'} \rangle = 1$. The second term describes hence ISBTs, whose dipole matrix elements $\langle f_n | \boldsymbol{p} | f_{n'} \rangle$ are given by the envelope functions. The ISB dipole matrix element of the envelope function (3.8) is

$$\begin{aligned} &\langle f_{n\boldsymbol{k}} | \boldsymbol{e} \cdot \boldsymbol{p} | f_{n'\boldsymbol{k'}} \rangle \\ &= \frac{1}{A} \int d^3 r e^{-i\boldsymbol{k}\boldsymbol{r}} \phi_n^*(z) \left[e_x p_x + e_y p_y + e_z p_z \right] e^{i\boldsymbol{k'}\boldsymbol{r}} \phi_{n'}(z). \end{aligned} \tag{3.18}$$

Due to the particular form of the envelope function, ISBTs are only allowed between states having the same wave vectors $\boldsymbol{k}_{x,y}^i = \boldsymbol{k}_{x,y}^f$; for transitions between different initial and final states ($n \neq n'$) only the term proportional to e_z does not vanish. In semiconductor heterostructures, this polarization selection rule only allows optical transitions if the electric field has a component perpendicular to the semiconductor layers. This reduces the dipole matrix element describing ISB transitions in a one band model to

$$\langle n | p_z | n' \rangle = \mu_{nn'} = \int dz \phi_n^*(z) p_z \phi_{n'}(z). \tag{3.19}$$

In an ideal QW with a symmetric potential, the wavefunctions ϕ are also symmetric and have either an even or odd parity; the dipole matrix element (3.19) becomes zero if ϕ_n and $\phi_{n'}$ have the same parity. This is known as the parity selection rule.

A commonly used quantity in spectroscopy is the dimensionless oscillator strength

$$f_{nn'} = \frac{2}{m^* \hbar \omega_{n'n}} |\langle n | p_z | n' \rangle|^2 = \frac{2 m^* \omega_{n'n}}{\hbar} |\langle n | z | n' \rangle|^2 \tag{3.20}$$

obeying the sum rule

$$\sum_{n'} f_{nn'} = 1 \tag{3.21}$$

where $f_{nn'}$ is positive for $n < n'$ (absorption) and negative for $n > n'$ (emission). The definition of the oscillator strength has to be adapted for multiband or nonparabolic models [Sirtori et al., 1994].

Based on the dipole matrix element (3.19), the absorption coefficient α can be calculated. In general, α is defined as the ratio between absorbed electromagnetic energy per volume V and time ($\hbar\omega \times W_{if}/V$) and the intensity of the incident radiation ($I = 1/2 \times \epsilon_0 c n E_0^2$). In the case of a quasi-two-dimensional system (for example a QW) a two dimensional absorption coefficient α_{2D} is defined. As opposed to the three dimensional α which has the dimension of inverse length, α_{2D} is dimensionless. If the sum over all possible initial and final states n, n' (considering emission and absorption) is taken into account, α_{2D} is given by

$$\begin{aligned} \alpha_{2D} = &\frac{\hbar\omega}{IA} \sum_{n,n'} \sum_{\boldsymbol{k}_\perp} \frac{2\pi}{\hbar} |\langle n | \frac{e}{m^*} \boldsymbol{A} \cdot \boldsymbol{p} | n' \rangle|^2 \times \\ &\left[f(E_n(\boldsymbol{k})) - f(E_{n'}(\boldsymbol{k})) \right] \delta(E_{n'}(\boldsymbol{k}) - E_n(\boldsymbol{k}) - \hbar\omega), \end{aligned} \tag{3.22}$$

where $f(E_n)$ is the occupation in state n given by the Fermi-Dirac distribution. Expressing $\boldsymbol{A}$ with (3.15) and I by E_0, applying the polarization selection rule and changing the

summation over $\boldsymbol{k}$ into a 2D-integral leads to

$$\begin{aligned}\alpha_{2D} =& \frac{\pi e^2}{\epsilon_0 c n \omega m^{*2}} \sum_{n,n'} \frac{2}{(2\pi)^2} \times \\ & \int d^2\boldsymbol{k} |\langle n|p_z|n'\rangle|^2 \left(f(E_n) - f(E_{n'})\right) \delta(E_{n'} - E_n - \hbar\omega).\end{aligned} \tag{3.23}$$

Assuming a parabolic in-plane dispersion (3.11), the integration over the Fermi-Dirac distributions can be solved analytically. Additionally, the δ function is replaced with a Lorentzian with a full width at half maximum (FWHM) of 2Γ to take into account the finite lifetime of the excited state. Assuming $\omega_{nn'} \approx \omega$ [Helm, 2000] the absorption coefficient is

$$\alpha_{2D} = \frac{e^2 k_B T}{2\epsilon_0 c n \hbar} \sum_{n,n'} f_{nn'} \ln \left(\frac{1 + e^{\frac{E_F - E_n}{k_B T}}}{1 + e^{\frac{E_F - E_{n'}}{k_B T}}} \right) \frac{\Gamma/\pi}{(E_{n'} - E_n - \hbar\omega)^2 + \Gamma^2}. \tag{3.24}$$

In ISB structures, often only the transition between the ground state and the first excited state of the QW, which has the largest oscillator strength, is of interest. For this transition, using $\ln\left(\frac{\cdot}{\cdot}\right) \approx \frac{E_F - E_1}{k_B T}$, (3.24) simplifies to

$$\alpha_{2D} = \frac{n_s e^2 \hbar}{2\epsilon_0 c n m^*} f_{12} \frac{\Gamma}{(E_2 - E_1 - \hbar\omega)^2 + \Gamma^2} \qquad \text{at } T = 0. \tag{3.25}$$

Density of states and Fermi level

For a three-dimensional semiconductor, the energy dependent density of states is [int, a]

$$\frac{dN_{3D}}{dE} = \frac{2\sqrt{2}}{\hbar^2 \pi} m^{*3/2} \sqrt{E - E_c}, \tag{3.26}$$

where E_c is the conduction band edge.

To achieve ISB absorption in a QW, it usually has to be degenerately doped, so that the Fermi level is between the first state E_1 and the second state E_2 of the QW. Assuming a complete ionization of the donors, the 2D doping density equals the 2D sheet carrier density n_s which is related to the Fermi level in the QW by

$$n_s = \frac{m^*}{\hbar^2 \pi}(E_F - E_1). \tag{3.27}$$

The QW ground state can also be populated by other means than doping, such as pumping electrons from the valence band into the QW ground state by illuminating the semiconductor with radiation having an energy equal or greater than the optical bandgap in the QW. In the work presented here, however, only the doping technique was used.

Manybody effects

The theory described so far is based on the assumption that carriers are far apart from each other and do not interact. In heavily doped semiconductors, this simplification can

lead to significant errors. To improve the simulation of ISBTs, the interactions between carries, so-called manybody effects, must be taken into account.

The shift of the ISBT E_{12} can be expressed by $\tilde{E}_{12} = E_{12}(1+\alpha-\beta)$. The depolarization shift α and the excitonic shift β are computed following the theory elaborated in Helm [2000].

External radiation excites not only electrons from the first state into a higher lying state in the QW, but leads also to a modulation of n_s. This collective oscillation of the electron plasma screens the external infrared field and results in an increase of the transition energy. The frequency or depolarization shift α describing this phenomenon is given by

$$\alpha = \frac{2e^2 n_s}{\epsilon\epsilon_0 E_{12}} \int_{-\infty}^{\infty} dz \left[\int_{-\infty}^{z} dz' \phi_2(z')\phi_1(z') \right]^2 . \tag{3.28}$$

The excitonic shift β (decrease of the ISBT energy) originates from the Coulomb interaction between the excited electrons and quasi-holes left behind in the ground state, forming a pair similar to the excitonic electron-hole pair, and is given by

$$\beta = -\frac{2n_s}{E_{12}} \int_{-\infty}^{\infty} dz \phi_2(z)^2 \phi_1(z)^2 \frac{\partial V_{xc}(n)}{\partial n} \tag{3.29}$$

$$V_{xc} = -\left(\frac{9\pi}{4}\right)^{1/3} \frac{2}{\pi r_s(n)} \times \left[1 + \frac{0.7734}{21} r_s(n) \ln\left(1 + \frac{21}{r_s(n)}\right)\right] \frac{e^2}{8\pi\epsilon\epsilon_0 a_B^*} \tag{3.30}$$

$$n = n(z) = \frac{m^* kT}{\pi\hbar^2} \sum_i \ln\left[1 + e^{\frac{E_F - E_i}{kT}}\right] |\phi_i(z)|^2 \tag{3.31}$$

$$r_s = \left[\frac{4\pi}{3} a^* 3 n(z)\right]^{-1/3} ; \tag{3.32}$$

V_{xc} is the exchange-correlation potential, and the dimensionless parameter r_s is the mean electron distance normalized to the effective Bohr radius $a^* = \frac{4\pi\epsilon_0\epsilon_r\hbar^2}{m_0 m^* e^2}$ and characterizes the electron gas. $\phi_i(z)$ are the wavefunctions in the QW and $n(z)$ is the three dimensional electron density.

The values of α and β can be estimated using the computed wavefunctions $\phi_1(z)$ and $\phi_2(z)$ taken from a simulation of an AlN/GaN MQW structure with the Schrödinger-Poisson solver *cband*. $n(z)$ was determined by equaling $\int n(z)$ to the 3-dimensional electron concentration in the QW, assuming that only the first state is occupied. For a sheet carrier density of $n_s = 7.5 \times 10^{12}\,\text{cm}^{-2}$ and a transition energy of 800 meV, $\alpha = 0.07$ and $\beta = 0.05$. In this work however, the dependency of the ISBTs on the doping level was not investigated; experiments covering this subject can be found in Helman et al. [2003].

Geometry factors

Due to the polarization selection rule, ISBTs only interact with the component E_z of an electrical field parallel to the growth axis c. To ensure that E_z is not zero when measuring ISB-related quantities, special sample geometries are used.

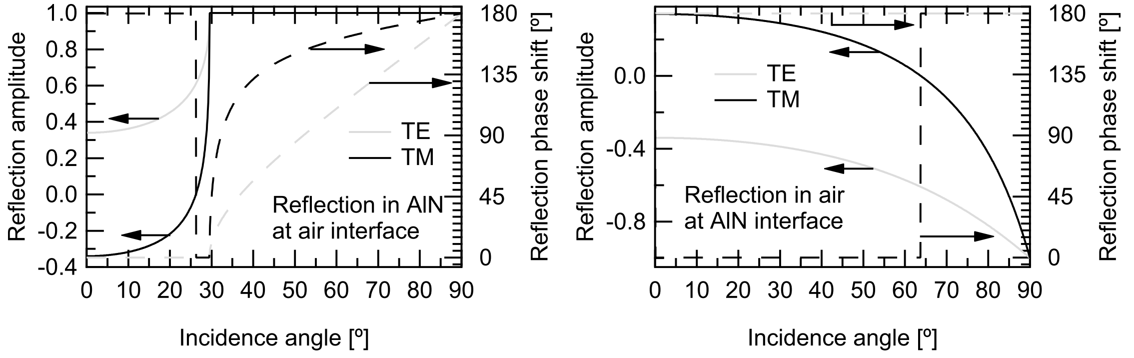

Figure 3.1: Reflection amplitudes calculated with the Fresnel equations at an AlN to air interface (left) and at an air to AlN interface (right) for TE and TM polarized light ($n_{AlN} = 2.03$, $n_{air} = 1$).

In this work, multipass waveguides (MPW) (see section 5) are used. To compare the calculated α_{2D} with experimental results, the sample geometry needs to be taken into account. In an MPW, the electric field component interacting with an ISBT is $E_z = E_0 \sin\Theta$, Θ being the angle between the growth axis z and the propagation direction of the optical beam, and E_0 the TM polarized field component. The TM intensity is therefore $I = 1/2 \times cn\epsilon_0 E_0^2 \sin^2\Theta$. The increase of effective interaction length between optical beam and QW has to be taken into account by a factor $1/\cos\Theta$. For an MPW the transmission is therefore

$$T = e^{-N_{QW} N_p \alpha_{2D} \frac{\sin^2\Theta}{\cos\Theta}} = e^{-\alpha L}, \tag{3.33}$$

where N_{QW} is the number of QWs and N_P the number of passes through the sample. As ISBTs do not interact with TE polarized radiation due to the polarization selection rule, T_{TE} can be used as baseline for ISB absorption and the absorbance can be extracted as $\alpha L = \ln(T_{TE}/T_{TM})$.

The standing wave pattern of the electric field in the waveguide must also be considered. The Fresnel equations describe the reflection and refraction of light (here given for non magnetic materials):

$$\left(\frac{E_{0r}}{E_{0i}}\right)_S = \frac{\sin(\Theta_t - \Theta_i)}{\sin(\Theta_t + \Theta_i)} \qquad \left(\frac{E_{0t}}{E_{0i}}\right)_S = \frac{2\sin\Theta_t \cos\Theta_i}{\sin(\Theta_i + \Theta_t)} \tag{3.34}$$

$$\left(\frac{E_{0r}}{E_{0i}}\right)_P = \frac{\tan(\Theta_t - \Theta_i)}{\tan(\Theta_t + \Theta_i)} \qquad \left(\frac{E_{0t}}{E_{0i}}\right)_P = \frac{2\sin\Theta_t \cos\Theta_i}{\sin(\Theta_i + \Theta_t)\cos(\Theta_i - \Theta_t)}. \tag{3.35}$$

The subscript i stands for the incident, r for the reflected and t for the transmitted (refracted) part. S denotes the reflection/transmission perpendicular (TE) and P parallel (TM) to the plane of incidence. In figure 3.1, the amplitude and phase of the reflected field is shown for an AlN/air interface as a function of the angle of incidence Θ_i. Coming from the AlN side (as is the case in the MPW) total reflection occurs at an angle of 29.5°. The Brewster angle, where the TM reflexion R_p is zero, is 26.2°.

The standing wave pattern of the intensity (SWI) for TM polarized light with a free space wavelength of 1.5 μm in a GaN/AlN sample is seen in figure 3.2. The period of

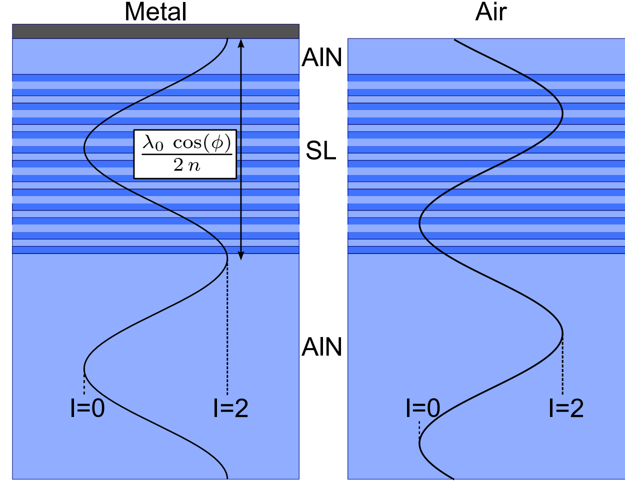

Figure 3.2: TM SWI in an MPW of a typical GaN/AlN sample with a 50 nm thick AlN cap layer. Left: metal coated sample surface. Right: uncoated sample surface.

the SWI in z direction is $\lambda \cos\Theta/2n = 295\,\text{nm}$ for a 45° MPW with an AlN active region on sapphire with an incidence angle $\Theta = 37°$ and a refractive index of $n = 2.03$. For a typical sample consisting of AlN buffer and cap layers and 40 periods of 5 nm AlN barriers and 1.5 nm thick GaN QWs, the absorption therefore also depends on the optical overlap of the SWI and the active MQWs. To calculate the optical overlap, two different sample configurations with different boundary condition are taken into account, one with a metal coated surface, the other without metal. At the metal-semiconductor interface, the intensity of TM polarized light has a maximum, whereas at the air-semiconductor interface, the reflected TM polarized light undergoes a phase shift of 121.5° for an AlN on sapphire MPW (for an angle of incidence $\Theta = 37°$). Averaging the integral of the SWI over the active region t as $1/t \int_t SWI$ results in a coupling factor C of 1 for the uncoated sample and 0.86 for the metal coated sample, shown in figure 3.2. For a sample with a thick active region, the standing wave effect is averaged out ($C = 1$). For a metal coated sample without cap, the crest of the SWI overlaps with the active region, wherefore C can be nearly two if the active region is thin.

3.1.4 Intersubband transitions in group III nitrides

In group III nitrides, ISBTs occur in transistor structures, where the transistor's GaN channel has a triangular potential with a 2DEG formed by the internal piezo and pyroelectric fields at the interface to the overlying $Al_xGa_{1-x}N$ barrier. An experimental study of ISBTs in such structures was done by Hofstetter et al. [2002]. Assuming that the electric field in the triangular potential is constant, the barrier is infinitely high, and that the 2DEG does not penetrate into it, the energy of the quantized electron states in the 2DEG can be estimated using the triangular potential approximation [Stern and Das Sarma, 1984]:

$$E_j = \left(\frac{\hbar^2}{2m_w^*}\right)^{1/3} \left[\frac{3\pi}{2} eF \left(j + \frac{3}{4}\right)\right]^{2/3}, \qquad (3.36)$$

where E_j is the j-th energy level and F the constant electric field in the triangular channel. The accessible ISBT energy range depends here on the Al concentration of the $Al_xGa_{1-x}N$ barrier and the relaxation grade of the structure, which both influence F and hence also the ISBT.

The sheet carrier density in the triangular channel can be approximated following Ambacher et al. [1999]. Subtracting carriers screened by a Schottky contact at the sample surface from the maximal sheet carrier density $\frac{+\sigma(x)}{e}$ induced by the internal fields results in a sheet carrier density

$$n_s = \frac{+\sigma(x)}{e} - \frac{\epsilon_0 \epsilon(x)}{de^2}[e\Phi_B + E_F - \Delta E_C], \tag{3.37}$$

where d is the distance between the Schottky contact and the $Al_xGa_{1-x}N$/GaN interface, Φ_B is the Schottky barrier height, $\epsilon(x)$ is the average static permittivity of the $Al_xGa_{1-x}N$ barrier, ΔE_C is the CBO between $Al_xGa_{1-x}N$ and GaN, and E_F is the Fermi level.

Another way to achieve ISBTs in GaN/AlN structures are MQWs. The internal fields in a QW or barrier in a MQW system are influenced by the presence of the adjacent layers. The interface charge density σ_{int} is now a function of the barrier and QW thickness [Bernardini and Fiorentini, 1998]:

$$\sigma_{int} = (P_{tot}^{AlN} - P_{tot}^{GaN})\frac{t_{AlN} + t_{GaN}}{t_{AlN}\epsilon_{GaN} + t_{GaN}\epsilon_{AlN}}, \tag{3.38}$$

where t_{AlN} and t_{GaN} are the barrier respective QW thicknesses. The internal electric field in the QW depends thus on that of the barrier and vice versa, so for an infinite GaN/AlN MQW, the internal fields in the GaN QW and the AlN barrier can be approximated by [Bernardini and Fiorentini, 2000, Lefebvre et al., 1999]:

$$F_{int}^{GaN} = \frac{t_{AlN}(\mid P_{sp}^{GaN} \mid - \mid P_{piezo}^{GaN} \mid - \mid P_{sp}^{AlN} \mid - \mid P_{piezo}^{AlN} \mid)}{\epsilon_{AlN}t_{GaN} + \epsilon_{GaN}t_{AlN}} \tag{3.39}$$

$$F_{int}^{AlN} = \frac{t_{GaN}(\mid P_{sp}^{AlN} \mid + \mid P_{piezo}^{AlN} \mid - \mid P_{sp}^{GaN} \mid + \mid P_{piezo}^{GaN} \mid)}{\epsilon_{AlN}t_{GaN} + \epsilon_{GaN}t_{AlN}}, \tag{3.40}$$

where ϵ_{GaN} or ϵ_{AlN} is $\epsilon_0\epsilon_{stat}$ for the GaN QW or AlN barrier respectively.

In figure 3.3, the internal fields in the AlN barrier and in a GaN QW (for a fixed QW thickness) are plotted as a function of barrier thickness, using (3.39) and the material parameters given in section 2.1.2. The curves to the left were computed for an active region fully strained on an AlN buffer ($P_{piezo}^{AlN} = 0$). To the right F_{int} for a 15Å and a 35 Å QW once strained on AlN and once on GaN ($P_{piezo}^{GaN} = 0$) are shown.

Since the voltage drop over the active region $V = \sum(t_{GaN}F_{GaN} - t_{AlN}F_{AlN})$ has to be zero, the second part of figure 3.3 depicting the internal field in the barrier is redundant and only shown for completeness.

It is also seen that F_{int} in the QW increases but saturates for thicker barriers; this can be explained by the increasing separation of two adjacent QWs, leading to a reduced screening of the interface charge densities. In an unstrained GaN QW (MQW grown pseudomorphically to GaN), F_{int} is greater than in a QW being strained to AlN (top right). The reason for this is that P_{sp}^{GaN} and P_{piezo}^{GaN} are pointing in opposite directions and attenuate each other in a pseudomorphic GaN QW on AlN. In AlN barriers, P_{sp}^{AlN} and

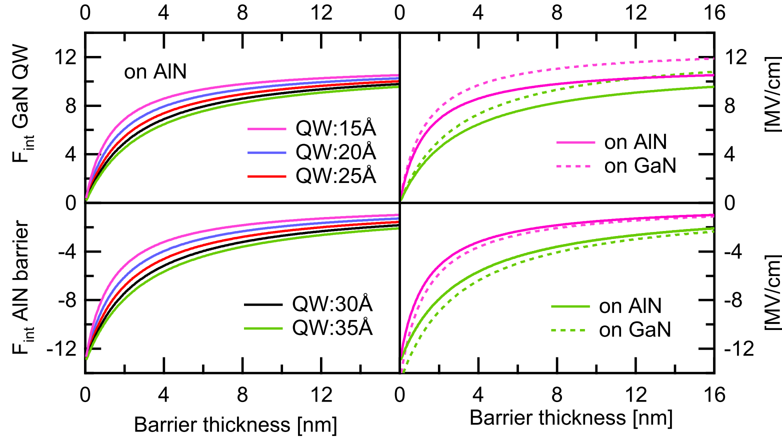

Figure 3.3: Internal field in the GaN QW and AlN barrier for QW thicknesses of 15, 20, 25, 30, 35 Å. Left: layers strained on AlN; the upper part shows the internal field in the QW, the lower part in the barrier. Right: comparison of the internal fields of a 15 Å and a 35 Å QW and barriers strained on AlN and GaN as a function of barrier thickness.

P_{piezo}^{AlN} have the same sign, resulting in a larger F_{int}^{AlN} for strained AlN barriers than for unstrained ones.

In a real MQW structure, which is some 100 nm thick and not far away from the surface, the assumption of an infinitely thick MQW structure does not hold anymore. There is an additional conduction band bending due to the buffer and cap layer and possibly a Schottky barrier height. F_{int} is therefore not the same for all QWs in the MQW.

Stark shift In contrast to InP or GaAs based system, electronic levels in group III nitride material systems (grown on c plane sapphire) are intrinsically Stark shifted due to the internal fields, as shown in the left panel of figure 3.4. An external field screens or enhances the internal fields, reducing or enhancing the intrinsic Stark shift. Applied external fields will almost always be significantly weaker than the internal fields having an amplitude of the order of 5–10 MV/cm.

The right panel of figure 3.4 shows the ISB energy E_{12} as function of the internal field. For a typical internal field of 8 MV/cm, the E_{12} transition is blueshifted by 80 meV compared to the hypothetical zero internal field case.

3.2 Photodetector physics

A photodetector is a responsive element that transforms incoming radiation into another signal (mechanical or electrical), which can be further amplified and processed. In general photodetectors are divided into two groups, following the process of transduction. In a thermal detector, the incoming radiation leads to a temperature change in the detector which induces for example a measurable change in detector resistance (bolometric effect). Such detectors generally have a spectrally broad photoresponse. In a photon detector, incident photons are absorbed producing free charge carriers which change the electrical

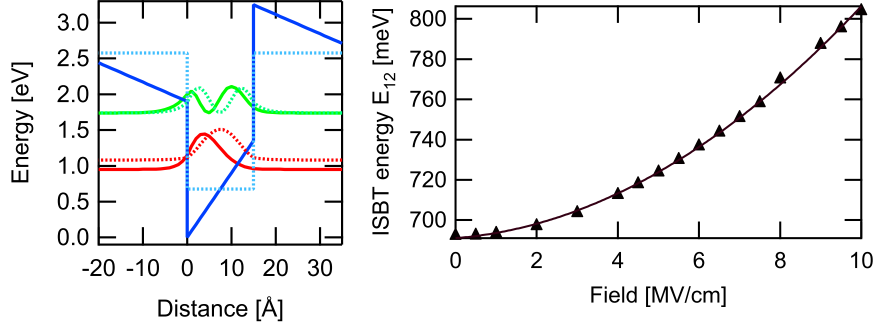

Figure 3.4: Stark shift in a 15 Å GaN QW between AlN barriers computed with *calcul-bande*. Left: conduction band diagram with typical nitride internal fields (solid lines) and with zero internal fields (dotted line). Right: ISBT energy E_{12} as function of internal field in the QW.

characteristics of the detector [Wolfe and Zissis, 1985].

All structures investigated in this work are photon detectors. Although the emphasis of the work is on understanding the working principle of structures and not on device performance, some basic figures for infrared photodetectors are given here.

The quantum efficiency $\eta = \frac{N_e}{N_P}$ is the ratio of generated electrons N_e per number of photons N_P falling on the detector during an observation period. Usually, the detector efficiency is characterized by the responsivity $\mathcal{R}$, which measures the ratio of the electrical output Δ to the monochromatic optical input P_i:

$$\mathcal{R} = \frac{\Delta}{P_i} = a\frac{\lambda e}{hc}\frac{N_e}{N_p} \tag{3.41}$$

$$P_i = \frac{hc}{\lambda\tau}N_P \qquad \Delta = a\frac{eN_e}{\tau} \tag{3.42}$$

It has the units of A/W or V/W and is, as opposed to the quantum efficiency, a function of the illumination wavelength λ. e is the electron charge, c the vacuum speed of light, τ the observation period and a a factor which depends on the working principle of the photon detector.

3.2.1 Rectification voltage and two photon absorption in asymmetric quantum wells

Nonlinear optics (NLO) describe the behavior of light in nonlinear media, in which the polarization P responds nonlinearly to the electric field E. NLO are most studied in nonlinear crystals such as lithium niobate or potassium dihydrogen phosphate. In the late eighties, Rosencher and Bois [1991], Rosencher et al. [1989, 1990] investigated second order optical effects of ISBTs in GaAs-AlGaAs step QWs with an asymmetric QW potential and huge second-order optical nonlinearities compared to bulk nonlinear crystals. Those optical nonlinearities are mainly due to the large dipole matrix elements of ISBTs, on which the second-order optical susceptibility has a quadratic dependence. The structures' ISBTs were around 10 µm, allowing for characterization with a CO_2 laser.

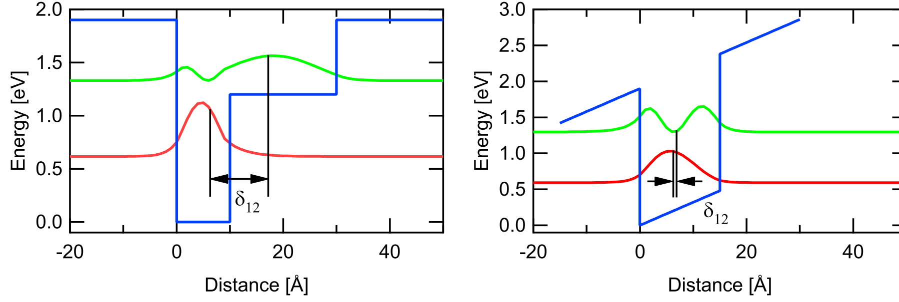

Figure 3.5: *calcul-bande* simulations of QWs with asymmetric potentials. Left: step QW. Right: biased QW. δ is the displacement between the wave functions' center of gravities.

Figure 3.5 shows two typical designs for an asymmetric QW potential; the symmetry is broken by a step in the material composition (left), or by the application of an external bias voltage (right). The mean electron displacement δ, which is the spatial difference between the center of gravities of the two involved wavefunctions (for example $\delta_{12} = \langle\psi_2|z|\psi_2\rangle - \langle\psi_1|z|\psi_1\rangle$) is 10.99 Å for the step QW but only 0.6 Å for the biased QW. The simulations are based on an artificial material with a CBO of GaN and AlN and an ISBT energy around 800 meV, but with no internal fields.

Asymmetric ISBT designs such as step QWs cannot be transferred directly to group III nitrides due to their internal fields. Furthermore, it is difficult to grow graded barriers in the group III nitride system. However, the internal fields lead to a built-in asymmetry of the potential; in a GaN QW, the symmetry is broken by default (even in the absence of an external field), making it a prominent candidate to study optical nonlinearities. A theoretical discussion of piezoelectric field enhanced optical nonlinear effects in a GaN/$Al_xGa_{1-x}N$ QW structure was published by Liu et al. [2000]. Another theoretical optimization of continuously graded $Al_xGa_{1-x}N$ QWs aiming at optical rectification (OR) at 1.55 µm and second harmonic generation (SHG) at 5.1 µm is presented by Radovanovic et al. [2004]. The first observation of ISB SHG in group III nitrides at 2.13 µm is reported by Nevou et al. [2007].

The response of an NLO medium can be described by expressing the dipole moment per unit volume, or polarization, P as a power series in the field strength E of the applied optical field:

$$P(t) = \epsilon_0\chi^{(1)}E(t) + \epsilon_0\chi^{(2)}E(t)^2 + \epsilon_0\chi^{(3)}E(t)^3 + \ldots, \tag{3.43}$$

where $\chi^{(1)}$ is the linear, $\chi^{(2)}$ the second order and $\chi^{(3)}$ the third order susceptibility [Boyd, 2003]. Second order nonlinear polarization occurs only in non-centrosymmetric crystals, such as wurtzite crystals, as opposed to third order nonlinear polarization which can be found in both centrosymmetric and non-centrosymmetric crystals.

The second order nonlinear polarization $P^{(2)} = \epsilon_0\chi^{(2)}E(t)^2$ with $E(t) = E_0e^{-i\omega_1 t} + E_0e^{-i\omega_2 t}$ can be written as

$$\begin{aligned} P^{(2)}(t) =& \epsilon_0\chi^{(2)}\big[E_0^2e^{-2i\omega_1 t} + E_0^2e^{-2i\omega_2 t} + 2E_0^2e^{-i(\omega_1+\omega_2)t} \\ & 2E_0E_0^*e^{-i(\omega_1-\omega_2)t} + \text{c.c.}\big] + 4\epsilon_0\chi^{(2)}E_0E_0^*. \end{aligned} \tag{3.44}$$

For $\omega_2 = \omega_1 = \omega$ in an asymmetric QW [Rosencher et al., 1989],

$$P^{(2)} = \epsilon_0 \chi^{(2)}_{2\omega}(\omega) E_0^2 e^{2i\omega t} + \epsilon_0 \chi^{(2)}_0(\omega) E_0^2 + \text{c.c.}\,, \quad (3.45)$$

where $\chi^{(2)}_{2\omega}$ is the second-order susceptibility, results in SHG and is not further discussed in this work. The second term does not depend on time, resulting in a DC electric field described by the optical rectification (OR) coefficient $\chi^{(2)}_0(\omega)$. In a two level QW, $\chi^{(2)}_0$ can be computed based on generation-recombination processes [Rosencher et al., 1990]: under illumination electrons are excited at the resonance frequency ω_{12} from $|1\rangle$ to $|2\rangle$ at a rate G_{12} from where they scatter back into $|1\rangle$ at a rate R_{12}:

$$G_{12} = n_{3D}\sigma_{12}\Phi \quad (3.46)$$

$$R_{12} = \frac{n_2}{\tau_{12}}, \quad (3.47)$$

where n_{3D} is the total three dimensional carrier density in a QW and n_2 is the 3D carrier density in $|2\rangle$. $\Phi = E^2 n_{GaN}/(2Z_0\hbar\omega)$ is the photon flux and $Z_0 = \frac{|\boldsymbol{E}|}{|\boldsymbol{H}|} = 1/(\epsilon_0 c)$ the vacuum impedance. In steady state, $R_{12} = G_{12}$ and

$$n_2 = \tau_{12} \times n_{3D}\sigma_{12}\Phi, \quad (3.48)$$

where τ_{12} is the ISB relaxation time. σ_{12} is the absorption cross section per electron in a QW:

$$\sigma_{12}(\omega) = \frac{\alpha_{2D}}{n_s} = \frac{e^2\omega_{12}}{\epsilon_0 c n_{GaN}} \mu_{12}^2 \frac{\Gamma}{(\hbar\omega_{12} - \hbar\omega)^2 + \Gamma^2}, \quad (3.49)$$

where 2Γ is the FWHM of the homogeneous broadening, μ_{12} the dipole matrix element and n_{GaN} the refractive index of the GaN QW. As the polarization P is the sum of all dipoles p_i per volume ($P = \frac{1}{vol}\sum p_i$),

$$P_0^{(2)} = n_2 \times q\delta_{12} = \tau_{12} n_{3D}\sigma_{12}\Phi \times \delta_{12} q. \quad (3.50)$$

Applying the definition $P_0^{(2)} = \epsilon_0 \chi_0^{(2)} E_{int}^2$ and setting $\omega = \omega_{12}$ (resonance) leads to the maximal OR coefficient

$$\chi^{(2)}_{0,max} = \frac{e^3}{2\epsilon_0\hbar} n_{3D} \frac{\tau}{\Gamma} \Pi \quad (3.51)$$

$$\Pi = \mu_{12}^2 \delta_{12} \quad (3.52)$$

This result is also obtained with the functional density matrix formalism [Rosencher et al., 1990].

The photoinduced steady state polarization $P_0^{(2)}$ can be measured as voltage drop V_{rect} over the total number of QWs times the QW width ($n_{QW} \times t_{QW}$):

$$V_{rect} = \frac{N_{QW} t_{QW}}{\epsilon_0 \epsilon_{s,GaN}} \times P^{(2)}_{0,max} \frac{\sin^2\Theta}{\cos\Theta} \quad (3.53)$$

$$V_{rect} = \frac{2 N_{QW} t_{QW}}{\epsilon_{s,GaN} n_{GaN}} \chi^{(2)}_{0,max} Z_0 I \frac{\sin^2\Theta}{\cos\Theta}, \quad (3.54)$$

$$(3.55)$$

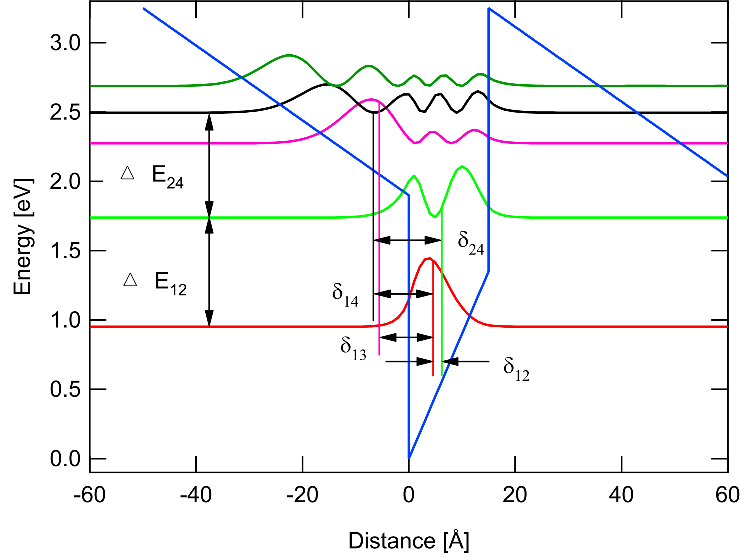

Figure 3.6: *calcul-bande* simulation of a 15 Å GaN QW with AlN barriers. The internal field is 9 MV/cm in the QW and 2.7 MV/cm in the barriers. δ_{ij} are the displacements between the center of gravities of wavefunction i and j.

where $I = \Phi \times \hbar\omega = 1/2 \times n/Z_0 E^2$ is the optical intensity, $\epsilon_{s,GaN}$ the static permittivity of GaN and $\sin^2\Theta/\cos\Theta$, the geometry factor as discussed in section 3.1.3. The rectification voltage V_{rect} is proportional to the factor $\Pi \times \tau$, the number of QWs N_{QW}, the doping density n_{3D} and the optical input intensity I.

Figure 3.6 shows the simulation for a 15 Å GaN QW between 50 Å AlN barriers. The respective values of transition energies, dipole matrix elements, mean electron displacement and oscillator strengths are listed in table 3.2.1. For a $|1\rangle$ to $|2\rangle$ transition, Π is 20.4 Å^3 compared to computed values of 131.8 Å^3 for a graded QW [Radovanovic et al., 2004] or 10.45 nm^3 for a step GaAs/AlGaAs QW in the 8–12 µm range [Rosencher and Bois, 1991]. In a graded or step QW the factor Π can be optimized by carefully adapting the QW shape. The structures investigated in this work consist of plain QWs and have therefore a smaller δ_{12} compared to the optimized theoretical structures cited above. Also, they operate around 1.5 µm, where μ is smaller compared to ISBTs at longer wavelengths, resulting in smaller Π.

Transition	Energy [eV]	μ [Å]	τ [ps]	δ[Å]	$\Pi \times \tau$ [Å^{3}ps]	f
ΔE_{12}	0.787	3.54	0.08	1.627	1.6931	0.57
ΔE_{13}	1.323	-0.24	0.48	-10.1	-0.28	0.0044
ΔE_{14}	1.544	0.11	0.39	-11.2	-0.053	0.0012
ΔE_{24}	0.757	-2.39	0.17	-12.83	-12.46	0.25

Table 3.1: Parameters extracted from the *calcul-bande* simulation presented in figure 3.6. μ is the dipole matrix element, τ the scattering time, δ the scattering time, $\Pi \times \tau$ the figure of merit, and f the oscillator strength.

A closer look at figure 3.6 shows that the ISBT of ΔE_{12}=787 meV is very close to ΔE_{24}=757 meV. As ISBTs have a line width on the order of 10–15% of ΔE, ΔE_{12} can be considered to be in resonance with ΔE_{24}. This gives rise to two photon absorption (TPA) from $|1\rangle$ via $|2\rangle$ to $|4\rangle$, another NLO process. Photons are either simultaneously (coherent TPA) or sequentially (incoherent TPA) absorbed. Under ideal conditions the TPA rate scales as the square of the excitation intensity. This dependence can intuitively be understood if one considers that the TPA process requires two photons to coincide in space and time. Together with third harmonic generation and self-focusing, coherent TPA absorption belongs to the $\chi^{(3)}$ processes (see (3.43)). Khurgin and Li [1993] discuss $\chi^{(3)}$ for different GaAs/AlGaAs QW shapes. Rapaport et al. [2003] determined experimentally the saturation intensity, the nonlinear refractive index, and the nonlinear absorption for the GaN/Al$_x$Ga$_{1-x}$N system. In Dupont et al. [1994], Liu et al. [2002], Maier et al. [2004, 2006], Schneider et al. [2005], and Zavriyev et al. [1995] QWIPS based on TPA are presented.

Similar to the absorption coefficient of the linear one photon absorption, α_{2D} (see section 3.1.3), a nonlinear two-dimensional absorption coefficient α_{2P} describing the TPA process can be derived. Incoherent TPA is strictly speaking not an NLO effect; nevertheless, it leads to a quadratic dependence on the excitation intensity. In a three level system, electrons are excited by linear absorption from $|1\rangle$ to $|2\rangle$ and in a second linear absorption process from $|2\rangle$ to $|3\rangle$. For a system with three equidistant, discrete energy levels at $T = 0$, where only the ground state is occupied, one finds

$$\alpha_{2P}^{nc} = n_2 \frac{e^2\hbar}{2\epsilon_0 cnm^*} f_{23} \frac{\Gamma_{23}}{(E_3 - E_2 - \hbar\omega)^2 + \Gamma_{23}^2}. \tag{3.56}$$

Here n_2 is the sheet carrier density in the intermediate state $|2\rangle$ (see (3.48)) and $2\Gamma_{23}$ the Lorentzian FWHM of the homogeneously broadened $|2\rangle$ to $|3\rangle$ transition. By using $n_2 = \tau_{12}\alpha_{2D}\Phi$ with $\Phi = I/(\hbar\omega)$ being the photon flux per unit area, (3.56) can be written as

$$\alpha_{2P}^{nc} = \alpha_{2D} \frac{I}{\hbar\omega} \tau_{12} \times \frac{e^2\hbar}{2\epsilon_0 cnm^*} f_{23} \frac{\Gamma_{23}}{(E_3 - E_2 - \hbar\omega)^2 + \Gamma_{23}^2}. \tag{3.57}$$

At resonance $\hbar\omega = \Delta E_{12} = \Delta E_{23}$; taking into account the geometry factors discussed in section 3.1.3, (3.57) becomes

$$\alpha_{2P}^{nc} = n_s \left(\frac{e^2\hbar}{2\epsilon_0 cnm^*} \right)^2 \frac{I}{\hbar\omega} \tau_{12} \frac{f_{12}}{\Gamma_{12}} \frac{f_{23}}{\Gamma_{23}} \frac{\sin^4\Theta}{\cos\Theta} N_p N_{QW}. \tag{3.58}$$

Sometimes the dephasing time $T_{ij} = h/(2\Gamma_{ij})$ is used instead of the FWHM $2\Gamma_{ij}$.

Assuming homogeneous broadening, the transition rate W_{13} and thus the absorption α_{2P}^c for coherent TPA is [Schneider et al., 2007]

$$W_{13}^{2P} = \frac{2\pi}{\hbar} \left| \frac{\langle\psi_1|H'|\psi_2\rangle n \langle\psi_2|H'|\psi_3\rangle}{E_2 - E_1 - \hbar\omega} \right|^2 \delta(E_3 - E_1 - 2\hbar\omega) \tag{3.59}$$

$$\alpha_{2P}^c = n_s \left(n_s \frac{e^2\hbar}{2\epsilon_0 cnm^*} \right)^2 \frac{I}{\hbar\omega} \frac{f_{12}}{(2\Gamma_{12})^2} \frac{f_{23}}{\Gamma_{13}} \frac{\sin^4\Theta}{\cos\Theta} N_p N_{QW}. \tag{3.60}$$

At resonance,

$$\alpha_{2P}^{c} = \alpha_{2P}^{nc} \frac{T_{12}T_{13}}{2\tau_{12}T_{23}} \tag{3.61}$$

describes the relation between coherent and non-coherent absorption.

Conclusion It was shown that in an asymmetric MQW, the displacement between the center of gravities of the wavefunctions results in a measurable photovoltage if ground state electrons are excited into a higher state of the QW. An interesting structure to investigate this phenomenon is the GaN QW, which is intrinsically asymmetric due to the internal fields of group III nitride heterostructures.

Chapter 4

Design and Simulation

In this chapter, the simulation programs used in this work to design ISB structures are presented. The second half of the chapter introduces the classical ISB photodetector schemes of the quantum well infrared photodetector and the quantum cascade detector, followed by a discussion of the photoinduced polarization detection mechanism used in the group III nitride photodetectors.

4.1 Simulation programs

Within the scope of this work, two different Schrödinger-Poisson solvers were used, the software *calcul-bande* written by J. Faist and *cband*, a program written by M. C. Foisy in 1990 at Cornell university originally intended for transistor structures. *calcul-bande* is an implementation of the transfer matrix method combined with a Poisson solver to obtain a self consistent Coulomb potential. Nonparabolicity of the in-plane carrier dispersion is taken into account through an energy-dependent effective mass [Sirtori et al., 1994]. For this work *calcul-bande* was used to calculate the states in a GaN single QW between two AlN barriers. The initial potential was calculated using (3.39). The energy dependence of the effective mass was taken from Tchernycheva et al. [2006].

cband was used to simulate more complex structures due to its superior convergence for long structures compared to *calcul-bande*. *cband* calculates the internal fields based on the structure and a relaxation factor.

4.2 Common ISB photodetector designs

The most common design for ISB infrared photodetectors is the photoconductive (PC) quantum well infrared photodetector (QWIP), shown schematically on the left panel of figure 4.1. Another design is the photovoltaic (PV) quantum cascade detector (QCD), on the right of figure 4.1. The active region of a QWIP consists of several identical QWs separated by significantly thicker barriers. Using material composition and layer thickness, the QW is designed such that the second quantized electron level is in resonance with the barrier's conduction band. The thick barriers reduce dark current by oppressing the coupling between the QW's ground states. Since QWIPs are symmetric structures, the application of an external bias is required (PC operation mode) to obtain a photoresponse.

Photoexcited electrons from the QWs are then contributing to the three dimensional photocurrent I_{3D} in the continuum above the barriers. A QCD, on the other hand, has a built in asymmetry, and needs no external bias to obtain a photoresponse; it is a PV detector. The active region of a QCD consists of an active (doped) QW, where conduction band electrons are excited from the ground state to a higher state by absorbing photons. The excited carriers are extracted by an extraction region consisting of a chirped SL, from where they are injected into the ground state of the next period's active QW. For the QWIP as well as for the QCD, the contact layers are usually made of QW material doped so that their Fermi level is aligned with the Fermi level in the QW. The working principle of QWIPs and QCDs are widely explored for detectors working in the MIR and the FIR and lately also in the NIR in InP and GaAs based systems.

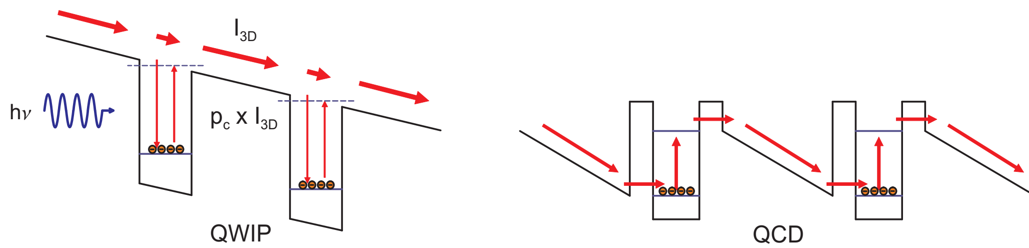

Figure 4.1: Left: schematic conduction band diagram of a QWIP under an external voltage. Right: schematic design of a photovoltaic QCD.

GaN QWIP Currently, a QWIP detector design cannot easily be applied to the AlN/GaN system for several reasons: the internal fields, originating from the spontaneous and strain induced polarizations (see section 2.1), impede the resonant alignment of a QW's electron state with the continuum, as it is preferable for a QWIP. To ease design, the barriers should also consist of ternary $Al_xGa_{1-x}N$, whose composition is a key parameter to obtain a specific ISBT energy. In nitrides, however, the internal fields depend among others on barrier composition, making the design less simple. Finally, the mobility and hence the drift velocity of electrons in $Al_xGa_{1-x}N$ layers drops with increasing Al content [Anwar et al., 2001]. Assuming perfect growth and interfaces, the second discrete state of only a very thin (2–3 ML of 2.59 Å) GaN QW sandwiched between AlN barriers is close to the continuum.

The left panel of Figure 4.2 shows a QWIP design in the $Al_xGa_{1-x}N$/GaN system. The contact layers and the 12 Å thick QWs consist of GaN, the 30 Å thick barriers of 50% $Al_xGa_{1-x}N$. Even with such thin QWs and ternary barriers, the second exited state does not lie in the continuum. Furthermore, the internal fields of this structure lead to an upward conduction band bending towards the cap layer, lifting the QWs close to the surface and their ground states above the Fermi sea; those QWs cannot contribute to the photocurrent. Towards the substrate, the active region's conduction band is bent downwards; a 2DEG and thus a triangular potential forms at the interface between the last AlN barrier and the GaN buffer layer. This band bending also makes the contact layers hard to align with the Fermi level of the active region. Finally, the doping density required for a given Fermi level is elevated in GaN due to its heavy effective electron mass, impeding the application of a homogeneous electric field across the active region.

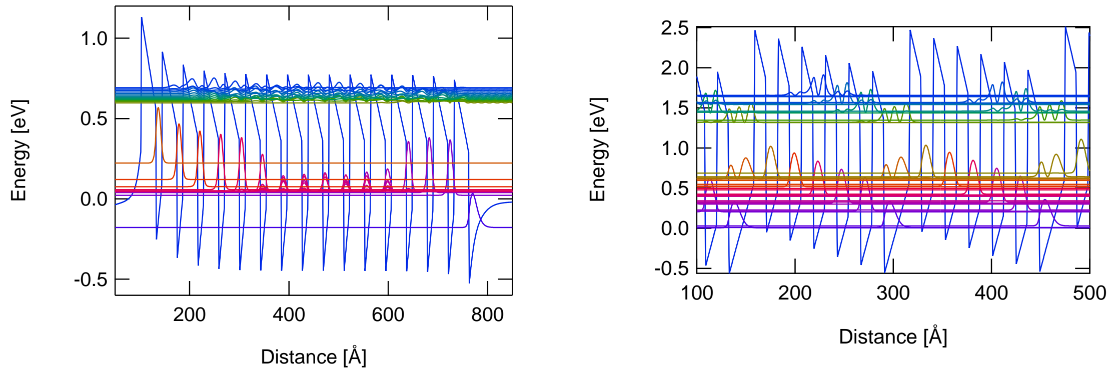

Figure 4.2: *cband* simulations of group III nitride photodetectors. Left: QWIP with GaN QWs and $Al_{0.5}Ga_{0.5}N$ barriers detecting at 630 meV. Right: QCD with GaN QWs and AlN barriers detecting at 600 meV.

GaN QCD The right panel of figure 4.2 shows a GaN/AlN QCD design with an ISBT energy of 600 meV. The active region consists of a 26 Å thick active GaN QW n-doped to 10^{19} cm^{-3} followed by an extraction cascade formed by a five period regular SL with undoped, 12.5 Å thick GaN QWs and AlN barriers. All layers are strained on a 50% $Al_xGa_{1-x}N$ buffer. Since the internal fields in the QWs and barriers have to cancel out each other (see also section 3.1.4), an asymmetric extraction cascade is formed. The energy difference between the ground states of two adjacent QWs equals the GaN LO phonon energy of 90 meV, except for the last step where it is close to twice the phonon energy. The alignment between the extractor and the active QW is crucial, as the QCDs efficiency drops if the extractor's uppermost ground state is out of resonance to the active QW's excited state. In group III nitrides, it is difficult to achieve a precise alignment, as already small changes in the internal field strengths (caused for instance by partial relaxation of the active region) can change the electron eigenenergies. Furthermore, the precision of the Schrödinger-Poisson simulations is at the time insufficient for QCD design due to uncertainties regarding the material parameters (discussed in section 2.1). Also, the tunneling probability through an AlN barrier is lower than through a comparable AlGaAs barrier because of the high effective AlN electron mass of 0.4 m_0. Figure 4.3 shows the tunneling probability T_e between the second states of two 15 Å QWs separated by an AlN barrier as function of the barrier width t_b and calculated following Capasso et al. [1986] using

$$T_e = e^{(-\sqrt{\frac{8m^* m_0 \Delta E q}{\hbar^2}} t_b)}. \tag{4.1}$$

The remaining barrier height ΔE for the second state was estimated to 830 meV. T_e decreases exponentially from 0.013 ‰ for a 1.5 nm barrier to 8.6×10^{-27} for a 10 nm barrier. The main difficulties however lie in the high defect density, which not only leads to leakage currents, but masks the tunneling process.

Nevertheless, some QWIP samples with different Al contents in the $Al_xGa_{1-x}N$ barriers and a QCD sample following the above described design were grown. Those

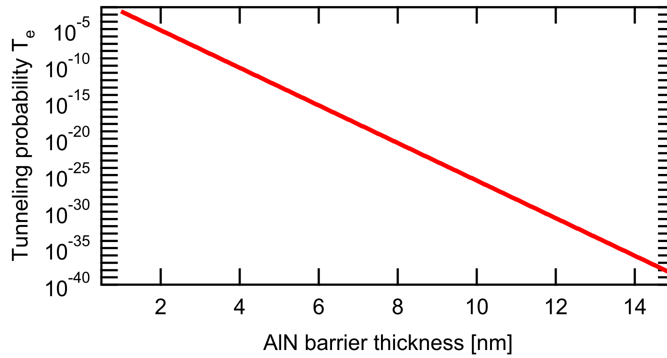

Figure 4.3: Tunneling probability as a function of AlN barrier thickness. From the simulation of a 1.5 nm QW, the remaining barrier height was taken to be 0.83 eV.

samples were processed at TU Vienna into mesas with diameters of 6 µm and 12 µm, in order to minimize the effective number of defects within one mesa. The characterization of the QWIP samples is found in section 8.1. For the QCD sample no photovoltage could be measured.

Photoinduced polarization Due to the problems described above, a detector design which does not rely on resonant tunneling or photoconductivity is desirable for group III nitrides. The approach taken in this work is based on the photoinduced polarization discussed in section 3.2.1, for which the product of the displacement of the wavefunctions center of gravity values ($\delta = \langle\psi_f|z|\psi_f\rangle - \langle\psi_i|z|\psi_i\rangle$), the squared oscillator strength μ^2 and the scattering time τ of the final state is a figure of merit ($\Pi\tau$). $\Pi\tau$ is strongly dependent on the QW asymmetry; the internal fields of $Al_xGa_{1-x}N$/GaN heterostructures, often complicating the design of quantum structures, are for once an advantage as they lead to intrinsically asymmetric QWs, enlarging the displacement δ. As for QWIPs and QCDs, the ultimate speed limit for this detection scheme is given by the scattering time τ, which was measured by Heber et al. [2002] to be on the order of 370 fs for GaN.

4.3 Photoinduced polarization detector design

The main intention of this work is to take advantage of the high conduction band offset between GaN and AlN, allowing for ISBTs in the NIR, while maintaining a simple detector design. This section describes the impact of different design aspects on photoinduced polarization.

Figure 4.4 shows self consistent *cband* simulations of two regular MQW structures with 15 Å (left) respectively 30 Å (right) thick GaN QWs and AlN barriers. The QW doping level is 10^{20} cm^{-3} and the structures are strained to an AlN buffer, giving rise to piezoelectric polarizations in the GaN QWs only. For the 15 Å QW SL, the thin barriers lead to delocalized wavefunctions. This delocalization increases the vertical current leakage through the second state, attenuating the photoinduced dipoles. Thus detector structures based on photoinduced polarization should have sufficiently thick barriers.

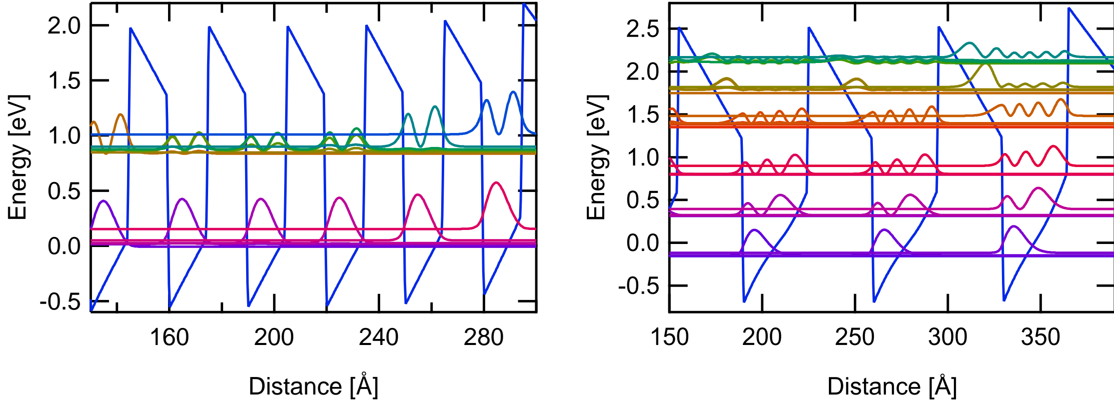

Figure 4.4: *cband* simulations of regular AlN/GaN SLs with 15 Å (left) and 30 Å (right) layers. The asymmetric potential is caused by the internal fields.

A thick QW has a lower ISBT energy and a higher $\Pi\tau$ due to the greater displacement and, more important, the higher dipole matrix element. A study on the ISBT between the QW ground state $|1\rangle$ and a final state $|f\rangle$ of a structure with GaN QW thicknesses ranging from 15 Å to 35 Å sandwiched between 50 Å AlN barriers based on *calcul-bande* simulations is presented in figure 4.5. To the left the simulated magnitude of the dipole matrix element μ_{1f} and the displacement δ_{1f} is depicted; the right panel shows the figure of merit $\Pi\tau$. Note that the parity rule, which interdicts ISBTs between wave functions of equal parity in a QW, is not valid in a GaN QW due to its broken symmetry; ISBTs can take place between all states.

For a $|1\rangle$ to $|2\rangle$ ISBT μ_{12} and δ_{12} increase for decreasing QW thickness (decreasing ISBT energy); for a 25 Å QW, $\Pi\tau$ is three times larger than for a 15 Å QW. For a $|1\rangle$ to $|3\rangle$ ISBT μ_{13} is still increasing with decreasing QW thickness, the displacement δ_{13} however is larger in the thinnest QW. This is because in a 15 Å QW, $|3\rangle$ is situated in the triangular potential close to the continuum. This state is also less confined than it would be in a thicker QW and has thus a longer scattering time τ. This argumentation also holds for a $|1\rangle$ to $|4\rangle$ ISBT in a 20 Å and 25 Å thick QW, where a partial recovery of the figure of merit can be observed.

Besides the QW thickness, other factors play a role for photoinduced polarization. The voltage across an MQW structure due to photoinduced polarization is linearly proportional to the figure of merit $\Pi\tau$, the number of periods N_{QW} and the carrier population n_{3D} in the QW ground state. Except for N_{QW}, these parameters depend on the internal fields which again depend on the chosen buffer layer, the interface quality, the overall $Al_xGa_{1-x}N$ content of the active region and hence the strain state of the layers.

Most photodetector samples investigated in this work were grown pseudomorphically on AlN and capped with AlN, wherefore a 2DEG forms at the active region/cap interface and a 2D hole gas at the active region/buffer interface (the opposite to figure's 4.2 QWIP structure simulated on GaN).

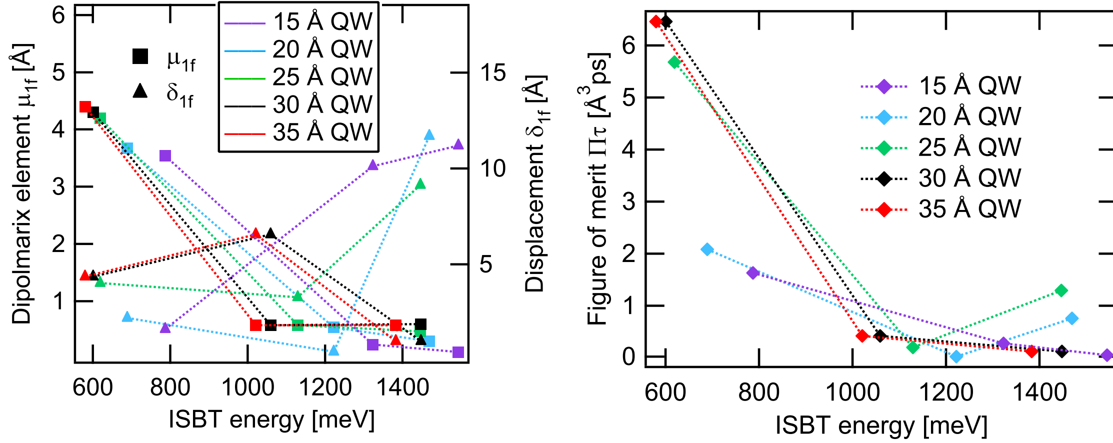

Figure 4.5: *calcul-bande* simulations for different QW thicknesses between 15 Å and 35 Å. Left: magnitude of dipole matrix elements μ_{1f} and displacements δ_{1f} for the first four states in a QW. Right: figure of merit $\Pi\tau$ for the first four states in a QW. The lines between data points are a guide to the eye.

4.4 Sample geometry

As already discussed in section 3.1.3, ISBTs can only interact with light polarized perpendicularly to the QWs (parallel to the c-axis). This must be taken into account when choosing a sample geometry for ISB experiments. The Brewster configuration shown in the right panel of figure 4.6 was used for some of the first ISB absorption measurements. The light is coupled into the sample's active region through the surface at the Brewster angle $\Theta_B = \arctan(n_{samp}/n_{air})$. This configuration is only suitable for structures with a high absorbance $N_{QW} \times \alpha_{2D}$, as the field passes only once through the active region, and the field fraction polarized perpendicularly to the QWs is small due to the steep angle Θ_2 of the field vector in the active region. For an AlN/sapphire sample, $\Theta_1 = 63.8°$ and $\Theta_2 = 26.2°$, wherefore $\sin^2\Theta_2$=20% of the TM polarized field fulfills the ISB polarization selection rule allowing it to interact with ISBTs.

An alternative geometry shown in the left panel of figure 4.6 is the 45° multipass waveguide (MPW) where the sample edges are polished into two parallel facets. The impinging field is coupled perpendicularly through one 45° facet into the sample, undergoes total reflections at the sample/air interfaces (provided that the refractive index of the sample is larger than $\sqrt{2}$), and couples out through the other facet. In 45° MPWs, $\sin^2 45°$=50% of the TM polarized field intensity is perpendicular to the QWs and for an MPW of length L and thickness d the field undergoes $N_P \approx L/d$ passes through the active region.

For $Al_xGa_{1-x}N$ on sapphire MPWs, the different refractive indices of the $Al_xGa_{1-x}N$ epilayer ($2.03 \leq n_{epi} \leq 2.3$, depending on overall Al content) and the sapphire substrate ($n_{sub} = 1.74$) must be taken into account. The field at the sapphire/epilayer interface undergoes an additional refraction, wherefore the angle between field propagation vector and c-axis is reduced from 45° to $\arcsin(n_{sub}/n_{epi} \times \sin 45°)$; for an AlN epilayer (a good approximation if the buffer layer is AlN), the angle is 37° and the fraction of TM polarized

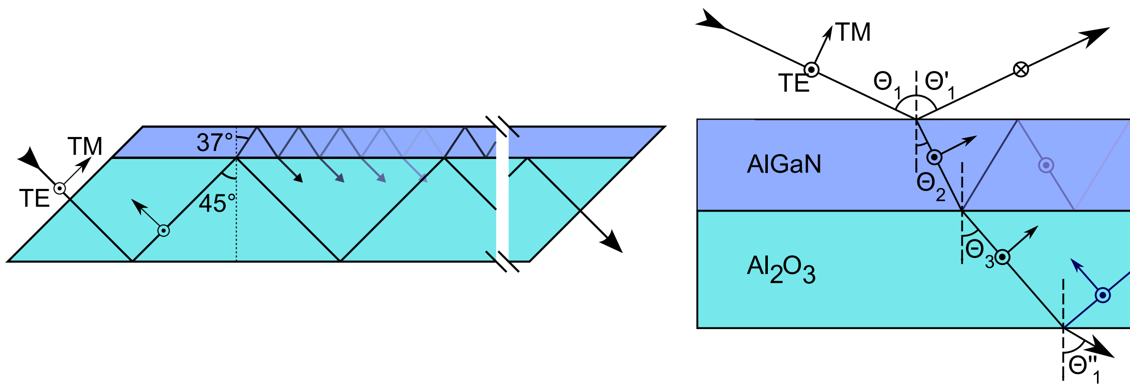

Figure 4.6: Left: 45° multipass waveguide; due to different refractive indices of the $Al_xGa_{1-x}N$ epilayer and the sapphire substrate the light undergoes an additional refraction at the sapphire/active region interface. Right: Brewster angle configuration.

field intensity perpendicular to the QWs reduces to 36%. Furthermore, the epilayer acts as a Fabry-Pérot (FP) etalon leading to FP resonances in the transmitted field (see (5.1)). As the epilayer is significantly thinner than the substrate, $N_P \approx L/d$ stays valid.

Chapter 5

Experimental Setup

After describing the sample processing from wafer to device in the first section, the measurement setup used for spectral absorption and photosignal measurements as well as for frequency response characterization is presented.

5.1 Sample preparation

All samples investigated in this work were grown on a sapphire substrate. The MQW region was then deposited either on a thick AlN buffer or on a GaN layer. Samples had typical dimensions of 7 mm×4 mm×0.4 mm. The samples were polished into 45° MPWs (described in section 4.4) for both absorption and PV measurements. To minimize scattering losses, the backside of the sapphire substrate was polished as well. This was done with an Allied TechPrep polishing machine using diamond lapping films with different grain sizes down to 1 µm, resulting in smooth surfaces at wavelengths of 1–2 µm.

For electro-optical measurements such as electromodulated absorption (EMA) or PV measurements, 800 μm wide contact stripes covering the whole sample width of about 4 mm were evaporated. Those contact stripes were either placed directly on the cap layer or on an intermediate $50 - 100$ nm thick Si_3N_4 or SiO_2 layer, which was deposited in an Oxford Plasmalab80. As 50 nm insulator layers often exhibited a significant leakage current due to pinholes, a 100 nm thick insulator layer was deposited on most samples.

For EMA measurements (see section 5.2), Ti/Au Schottky contacts were evaporated on the intermediate insulator layer (metal-insulator-semiconductor (MIS) contact). It was found that a Ti/Au contact evaporated on AlN is Schottky, therefore no intermediate layer is needed in this case.

Ohmic contacts were evaporated directly on the cap layer (metal-semiconductor (MS) contacts). Generally, Al is used as ohmic contact on GaN due to its small barrier height of 0.17 V towards GaN (Au on GaN, in comparison, has a barrier height of 5.1 V) [Mohammad, 2005] (see also appendix A). As it is not practicable to evaporate Al directly on GaN, Ti/Al/Ti/Au respectively Ti/Al/Ni/Au was used for ohmic contacts. The first Ti layer ensures a good adhesion between contact and semiconductor, the Al layer diffuses into the semiconductor for an Ohmic contact behavior, the second Ti (or Ni) layer is a diffusion barrier between Al and Au, and the final thick Au layer is required for wire bonding. After evaporation, the samples were annealed at 860 °C for one minute in an N_2 atmosphere.

At TU Vienna (Austria), some samples were processed into mesa structures using standard photolithography and reactive ion etching, with sizes ranging from a few $100\times100\,\mu m^2$, down to $6\times6\,\mu m^2$. To permit wire bonding of the smaller mesas, extended bond contacts were processed.

Figure 5.1: Picture of a sample on a submount. The background grid has a spacing of 5 mm. Two stripe contacts were evaporated on the right side of the sample; on the sample's left side, mesa structures were evaporated.

All samples were mounted on copper submounts of $19 \times 7 \times 1.5\,mm^3$, as shown in figure 5.1. As the sapphire substrate does not lend itself to soldering, varnish was used to fix the samples. The contacts were wire bonded to gold-ceramic pads which were also glued with varnish on the copper submount.

5.2 Spectral measurements

Transmission as well as most photovoltaic measurements were performed with a Bruker IFS66 Fourier transform infrared (FTIR) spectrometer. For low temperature measurements the sample's copper submount was placed in a liquid He flow cryostat. The collimated beam from the IFS66 is focused with a parabolic mirror onto one of the sample's 45° facets. As the external mirror has a focal length of 7.6 cm as compared to the IFS66s internal sample compartment with a focal length of 16.1 cm, the external setup's focus is 4.5 times smaller and more intense compared to the focus of the internal sample compartment.

For transmission measurements, the beam is collected from the samples' other 45° facet and focused on an external MCT detector with two additional parabolic mirrors, as shown in figure 5.2. To compensate the beam offset generated by the 45° MPW, the last two parabolic mirrors and the detector are mounted on an xy-stage.

Figure 5.3 shows the transmission of sample E1208, measured in the sample compartment, with different combination of sources, beam splitters, and detectors of the IFS66. The sample was placed perpendicularly into the optical path of the FTIR, so that no ISBT absorption is measured. The typical setup for low energies consists of a MIR glowbar source, a KBr beam splitter and a Mercury Cadmium Telluride (MCT) detector; below $1700\,cm^{-1}$, the transmission is cut off by the sapphire substrate. The NIR range (where the ISBT in this sample takes place) is covered by a halogen lamp, a CaF_2 beam splitter and again the MCT detector. With a Si detector, this setup is extended into the visible. For the UV (high energies), a deuterium source in combination with the CaF_2 beam splitter and a GaP detector is used; this allows to measure the bandgap absorption of GaN around $30000\,cm^{-1}$.

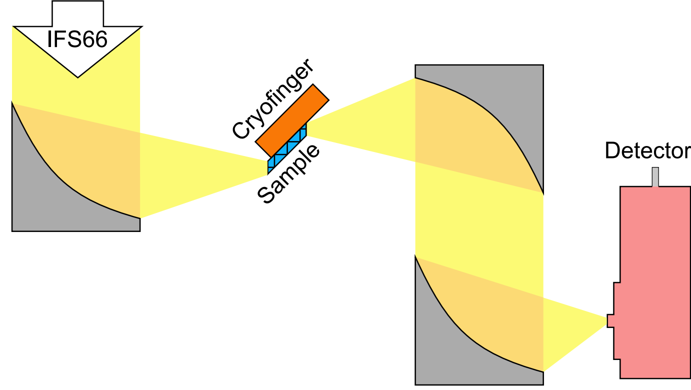

Figure 5.2: Schematic drawing of the external beam condenser. The collinear light coming from the FTIR is focused by a parabolic mirror on the sample facet; for transmission, the light is recollected from the other sample facet with another parabolic mirror and focused on the detector by a third parabolic mirror.

The modulation of the transmission seen in figure 5.3 is due to Fabry-Perot (FP) oscillations in the epilayer. For radiation propagating at an angle Θ towards the epilayer's growth direction, the period $\Lambda \propto 1/\lambda_j - 1/\lambda_{j-1}$ of the FP oscillations is linked to the epilayer thickness d by

$$\frac{1}{\lambda_j} = \frac{j}{2dn\cos(\Theta)}. \tag{5.1}$$

Adapting (5.1) for common spectroscopic units results in

$$\Lambda\,[\mathrm{cm}^{-1}] = \frac{5000}{d\,[\mu\mathrm{m}]n\cos(\Theta)}. \tag{5.2}$$

In figure 5.3, n=2.03 (refractive index of AlN), $\Theta = 90°$, and $\Lambda = 1270\,\mathrm{cm}^{-1}$ results in $d = 1.9\,\mu$m, which is in reasonable agreement with the nominal d of 1.775 µm for this sample.

5.2.1 Absorption

ISB absorption was measured with two different methods. The first is rapid scan transmission (applied to samples with high doping densities), the second is electromodulated absorption (EMA), a lock-in/step scan detection technique allowing to measure absorption changes on the order of 0.1‰ [Faist et al., 1994a] which is applied to weakly doped samples with thin or insulating cap layers. In both cases the sample is measured in transmission (MPW).

For rapid scan absorption measurement, the transmission is measured in TM (T_{TM}) and TE (T_{TE}) polarization using a polarizer and normalized with the background transmission. As ISBTs do not interact with TE polarized radiation (due to the polarization selection rule, introduced in section 3.1.3), T_{TE} can be used as baseline for ISB absorption and the absorbance can be extracted as $\ln(T_{TE}/T_{TM})$. In group III nitride samples, this normalization leads to a modulation of the absorbance spectrum due to the stronger

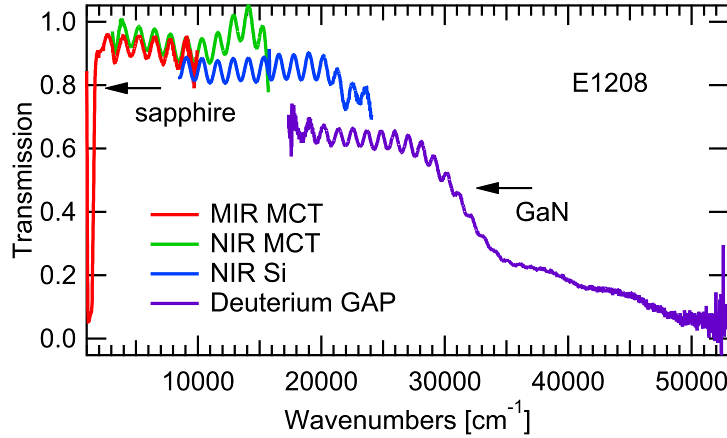

Figure 5.3: Perpendicular transmission of E1208 for different spectrometer source / beam-splitter / detector combinations, as stated in the figure.

intensity of the FP oscillations in TE polarization, impeding the precise peak energy and FWHM extraction of weak ISB absorptions. The reason for the stronger FP oscillations in T_{TE} is the weak TM reflection at the epilayer/sapphire interface, as the radiation propagates through this interface at an angle close to the Brewster angle for a 45° MPW. If only the ISBT peak energy is of interest, it is therefore advantageous to directly extract it from T_{TM}.

During EMA measurements a square wave voltage with a negative amplitude, a duty cycle of 50%, and a frequency in the 10 kHz range was applied between the Schottky and a reference contact stripe (figure 5.4). The QWs closest to the contact are periodically depleted and therefore ISB absorption is analogously periodically reduced. Light from the IFS66 is guided through the MPW below the MIS contact and detected by an external detector (see also figure 5.2). The modulated signal of the detector is then amplified by a lock-in amplifier (LIA) where it is demodulated in phase with the voltage square wave and fed back into the IFS66, whose mirror is moved in discrete steps at intervals longer than the LIA's integration time. This measurement (ΔT) is normalized with a rapid scan transmission measurement (T) of the sample under zero bias, yielding the differential transmission $\Delta T/T$, which is proportional to the absorbance.

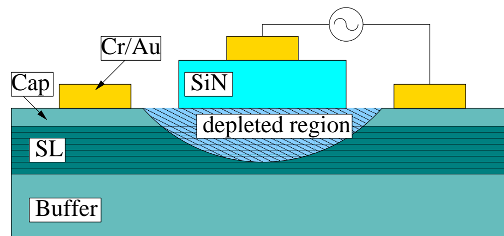

Figure 5.4: Sample processed for EMA measurements. The region beneath the Schottky contact (in this figure a Si_3N_4 MIS contact) is periodically depleted.

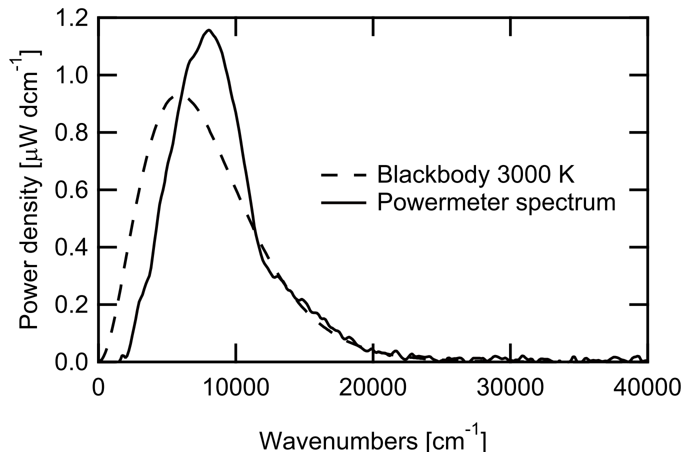

Figure 5.5: Measured spectral power density of the IFS66 internal halogen light in the focus point of the external beam condenser. The red (dashed) curve is a calculated blackbody at 3000 K.

5.2.2 Photovoltage

For PV measurements, the sample itself serves as detector for the IFS66 spectrometer. The electric signal coming from the sample is amplified with a Stanford Research SR570 low-noise preamplifier and then fed into the external detector port of the IFS66. Measurements were normally carried out at an amplification of 200 nA/V or 1 μA/V. The DC input impedance at this amplification is 100 Ω and the 3 dB bandwidth is 200 kHz in the high bandwidth and 20 kHz in the low noise mode.

The intrinsic PV spectral shape is obtained by dividing the measured PV with the combined spectrum of the radiation source and the optics (mirrors, beam splitter, windows). Figure 5.5 shows the spectrum of the IFS66 NIR source with CaF_2 beamsplitter measured with an Ophir thermopile detector (2A–SH) compared to an ideal blackbody at 3000 K with the same power. The measured source spectrum is maximal around 8000 cm^{-1} whereas the ideal blackbody peaks at 5900 cm^{-1}. This discrepancy is caused by the halogen lamp's quartz housing, which absorbs light at low energies.

For ISBTs with their narrow linewidths, the spectral shape of the measured PV does not deviate much from the intrinsic PV.

5.3 Frequency response

A crude estimation of the low frequency PV response is given by the peak value of the spectral PV as a function of the FTIR's mirror velocity and thus its scanning frequency. As the mirror position in a Fourier transform spectrometer is usually determined by measuring the intensity oscillations of a HeNe laser at 15798 cm^{-1} modulated by the spectrometer's interferometer, the mirror velocity can be expressed as frequency of the HeNe laser oscillations. If the mirror has a 'velocity' of a kHz, a signal at b cm^{-1} is thus sampled at a frequency of $b/15798\,\mathrm{cm}^{-1} \times a$ kHz. As the IFS66 allows for scan velocities of up to 100 kHz and the measured signals are around 7000 cm^{-1}, this method works for modula-

tion frequencies up to around 50 kHz.

For higher frequencies and more precise results, samples were illuminated with a modulated semiconductor laser emitting at 1.55 µm (6450 cm^{-1}). As the electric cabling of the cryostat strongly influences the signal for frequencies above 0.1 MHz, temperature control is abandoned for high frequency measurements and the sample on its copper mount is soldered to a BNC mount. One contact is directly soldered to the BNC center pin, the other is connected via the copper mount to the BNC ground plate, as shown on the top right panel of figure 5.6. This measurement requires that the PV response of the investigated sample at the laser wavelength of 1.55 µm is sufficiently strong at room temperature.

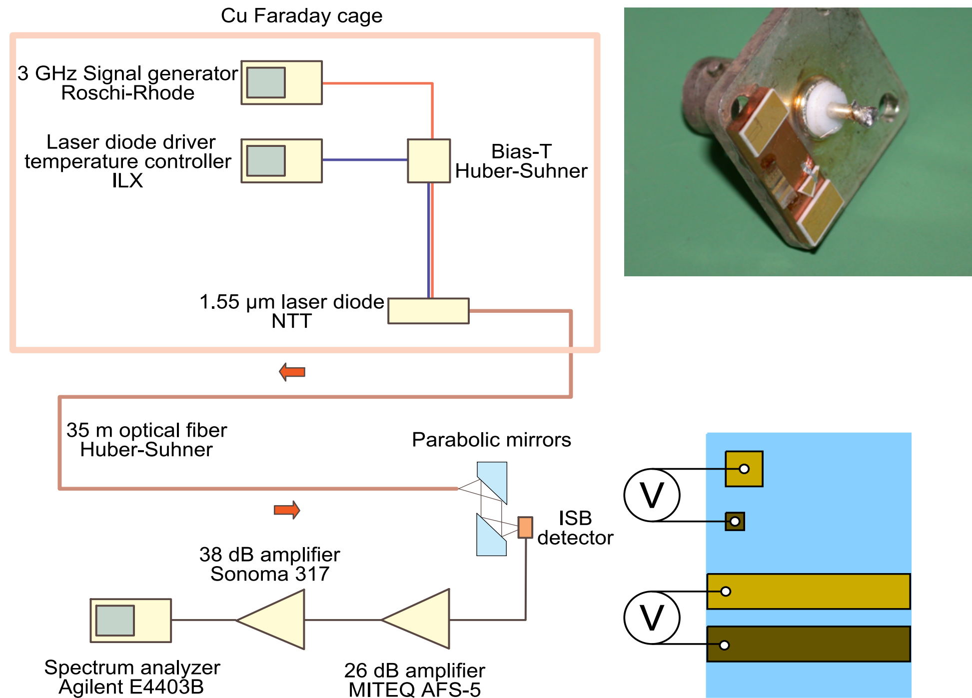

Figure 5.6: Left: frequency response measurement setup. The radiation of the modulated semiconductor laser is guided through an optical fiber and focused on the sample with parabolic mirrors. The PV signal is amplified and visualized by a spectrum analyzer. Right: picture of BNC submount (top), schematic view of sample surface (bottom).

The left panel of figure 5.6 shows the measurement setup used for frequency response measurements: the semiconductor laser diode (NEL NLK1554STB DFB) is sinusoidally modulated through a bias-T (Huber and Suhner) with a Rhode & Schwarz SML signal generator. The signal generation part of the setup, consisting of laser diode, signal generator, ILX LDC 3724B laser diode driver and temperature controller, and a bias-T, is shielded by a copper Faraday cage at 30 m distance from the sample to prevent electrical crosstalk. The laser radiation is then guided through 35 m of optical single mode fiber and focused on the sample's 45° facet below the contact (either a mesa or a stripe) with a parabolic mirror. The PV signal detected by the sample is amplified by a 38 dB Sonoma 317 and, for frequencies above 100 MHz, a 26 dB Miteq AFS5-001-02000-30-10P-4 low noise preamplifier, and measured with an Agilent E4403B spectrum analyzer.

Chapter 6

Absorption Measurements

In this chapter the ISB absorption of MBE and MOVPE grown samples is presented and discussed.

6.1 Rapid scan absorption for MOVPE and PAMBE grown samples

The PAMBE and MOVPE samples listed in table 6.1 were measured in rapid scan transmission, as described in section 5.2.1, and compared with simulated ISBT energies. In table 6.1 the nominal growth parameters of the measured samples are summarized; there is an uncertainty of the doping level of a factor two for PAMBE and of ±25% for MOVPE. Samples whose name begins with A are grown by MOVPE in Lausanne; those whose name begins with E are grown by PAMBE in Grenoble. As mentioned before (see section 2.2), the active region of MOVPE samples (except A1334, which is grown on AlN) is grown on a thick GaN layer deposited directly on sapphire whereas the growth for PAMBE samples starts on an AlN on sapphire template. The active region is a 40 period MQW structure for the PAMBE samples, and 30 period MQW structure (except A767 and A1334 which have 10 periods) for the MOVPE samples.

Figure 6.1 shows the peak energy of the measured ISB absorption of the E_{12} transition as a function of the QW thickness as listed in table 6.1 along with transition energies obtained with *calcul-bande* simulations. From the simulations, a decrease of the peak energy with increasing QW thickness is expected. The decrease of E_{12} in the simulation for QW thinner than 7.5 Å is due to the fact that the second state is in the continuum, a further decrease of the QW thickness only shifts the ground state to higher energies.

The measurements roughly follow the simulation curve. The deviation between simulation and measurement is due to variations of the growth parameters, such as layer thicknesses and interface roughness. Furthermore, the strain state of the active region has an influence on the ISBT energy as well as on the FWHM of the absorption spectrum. To determine the strain state, the grade of relaxation was determined for some samples using high resolution X-ray and reciprocal space mapping. However, this work does not contain a systematic investigation of this subject.

In table 6.2, the ISBT peak position along with the FWHM are listed. The FWHM of the MOVPE samples were read out of the transmission measurements, the ones for

Sample	Buffer [µm], mat	QW [Å], mat, n [10^{18}cm^{-3}]	Barrier [Å], mat	Cap [nm], mat
A640	2, GaN	14, GaN, 5	20, $Al_{0.98}In_{0.02}N$	30, $Al_{0.98}In_{0.02}N$
A658	2, GaN	18, GaN, 5	20, AlN	30, AlN
A663	2, GaN	16, GaN, 5	20, AlN	30, AlN
A699	2, GaN	10, GaN, 5	50, AlN	30, AlN
A767	2, GaN	18, GaN, 5	20, $Al_{0.98}In_{0.02}N$	—
A1334	1, AlN	12, GaN, 2	30, AlN	45, AlN
E662	0.27, $Al_{0.35}Ga_{0.65}N$	25, GaN, 100	25, AlN	150, $Al_{0.35}Ga_{0.65}N$
E666	0.27, $Al_{0.35}Ga_{0.65}N$	17.5, GaN, 100	17.5, AlN	150, $Al_{0.35}Ga_{0.65}N$
E728	0.25, $Al_{0.35}Ga_{0.65}N$	10, GaN, 10	20, AlN	180, $Al_{0.35}Ga_{0.65}N$
E1293	1.1, AlN	15, GaN, 10	50, AlN	50, AlN
E1296	1.1, AlN	20, GaN, 10	50, AlN	50, AlN
E1291	1.1, AlN	25, GaN, 10	50, AlN	50, AlN
E1297	1.1, AlN	30, GaN, 10	50, AlN	50, AlN
E1295	1.1, AlN	35, GaN, 10	50, AlN	50, AlN

Table 6.1: Nominal growth parameters of PAMBE (Exxx) and MOVPE (Axxx) samples.

PAMBE samples from the absorbance. E666 shows a double peak spectrum, so in this case the FWHM was taken from a Lorentzian spanning both peaks. As seen in figure 6.1, rapid scan absorptions taken from MOVPE samples (on GaN) show smaller ISBT peak energies than from PAMBE samples (on AlN) with the same QW thickness. This is seen for example for sample A640 which has a 14 Å QW and peaks at an ISBT energy of 5307 cm^{-1} in comparison to E1293, QW thickness of 15 Å and an ISBT at 5940 cm^{-1}. A possible reason for the lower E_{12} in MOVPE sample is the sharper QW/barrier interface of PAMBE samples. This results in a lower QW ground state for the latter as compared to MOVPE samples with rougher interfaces. The difference in the interface quality is caused by different growth conditions on GaN on sapphire substrate [Nicolay et al., 2007] and can be resolved by choosing AlN on sapphire template for MOVPE .

To achieve ISBT at 6450 cm^{-1}(800 meV, 1.55 µm) in MOVPE samples, several approaches besides thinner QW were investigated. Active regions with high AlN concentration were grown, sample A699 has 50 Å AlN barriers (10 Å GaN QW) and peaks at an ISBT of 6725 cm^{-1}. The active region can additionally be grown on an AlN on sapphire template, as it is usually done for PAMBE samples. Using this approach, an ISBT energy of 6125 cm^{-1} was achieved for a QW of 12 Å (A1334).

To obtain a clearer picture of the QW thickness influence on the sample characteristics, a series (E1291–E1297) of samples only differing in the QW thickness was grown. The 1.1 µm buffer and 50 nm cap layers as well as the 50 Å barriers are AlN. Figure 6.2 shows the TM polarized transmission (top) and the corresponding absorbance (bottom)

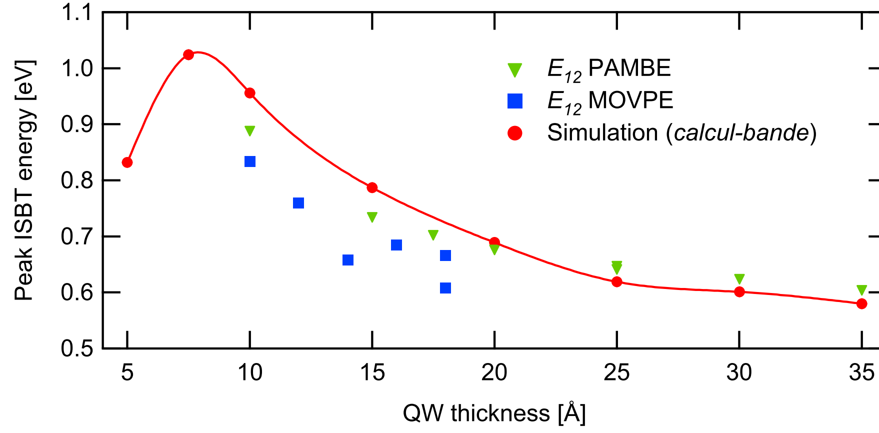

Figure 6.1: Rapid scan ISB absorption peak energies E_{12} as function of QW thickness of various PAMBE and MOVPE samples along with a *calcul-bande* simulation. The red line connecting the simulation data points is a guide to the eye.

Sample	Peak absorption position			FWHM
	[cm^{-1}]	[meV]	[μm]	[cm^{-1}]
A640	5307	658	1.88	680
A658	5370	666	1.86	925
A663	5525	685	1.81	800
A699	6725	834	1.49	1230
A767	4920	608	2.04	470
A1334	6125	760	1.6	1020
E662	5184	643	1.93	680
E666	5677	704	1.76	987
E728	7200	890	1.39	880

Table 6.2: Rapid scan absorption peak position E_{12} and FWHM of the MOVPE (Axxx) and PAMBE (Exxx) samples shown in figure 6.1.

of this series, with different ISB absorption peaks corresponding to the E_{12}, E_{13}, and E_{14} transitions. The higher order transitions are stronger in thick QWs as the absorption α_{1f} is proportional to the dipole matrix element $\mu_{1f}^2 \propto 1/E_{1f}^2$, wherefore E_{13} is not visible for the 15 Å QW and E_{14} for both the 20 Å and 15 Å QWs. Furthermore, those transmission spectra show that the parity rule is not valid for asymmetric QWs, allowing the E_{13} ISBT.

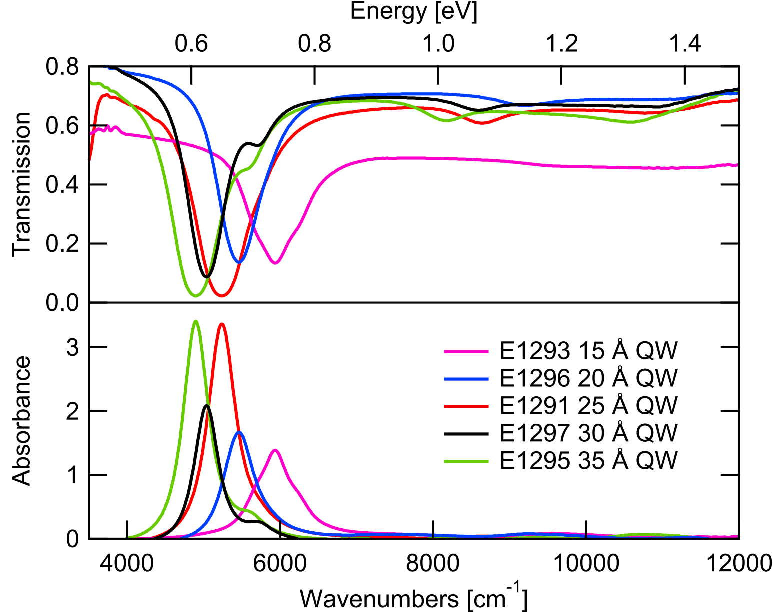

Figure 6.2: TM transmission (top) and corresponding absorbance (bottom) of the PAMBE grown sample series with different QW thicknesses.

Table 6.3 lists the peak absorption and linewidth energies of this sample series. Due to their strong ISB absorption, the absorption approximation $1 - e^{-\alpha L} \simeq \alpha L$, which is valid only for $\alpha L \ll 1$ can not be applied here; as the transmission is therefore no longer Lorentz shaped, the listed ISBT linewidths were taken from the absorbance (see bottom panel of figure 6.2). The relative linewidth $2\Gamma/E_{12}$ of the absorbance is increasing with decreasing QW thickness: for the sample with the thinnest QW it is 11%, for the sample with the thickest QW it is 8%; this is due to the greater effect of interface roughness on transition energy for thinner QWs. The samples differ by 5 Å ($\approx$ 2 ML) in QW thickness. As the spectrum for a given QW width has its peak at the energy where the adjacent QWs' spectrum is at half its maximum value, the interface roughness is estimated to be in the range of 1 ML. The sheet carrier densities listed in table 6.3 were calculated with Fermi's golden rule using the integrated measured absorbance $I_{\alpha L}$ and the dipole matrix elements μ_{12} calculated with *calcul-bande*.

The bottom panel of figure 6.2 depicts the absorbance of the different samples. Although the dipole matrix element μ increases for decreasing QW thicknesses, this trend is not clearly seen in the measurements due to the nonuniform doping density of the series: sample E1291 (25 Å QW) has the highest sheet carrier density of 9.2×10^{12} cm^{-2}, and sample E1297 (30 Å QW) has the lowest of 5×10^{12} cm^{-2}.

Figure 6.3 gives a summary of the measured ISBT peak positions for the different

Sample		E1293	E1296	E1291	E1297	E1295
QW	[Å]	15	20	25	30	35
E_{12}	[cm^{-1}]	5940	5460	5230	5045	4890
	[meV]	736	678	649	626	606
	[µm]	1.68	1.83	1.91	1.98	2.046
FWHM E_{12}	[cm^{-1}]	632	478	432	385	400
$I_{\alpha L}$	[cm^{-1}]	950	986	1950	1015	1835
μ_{12}	[Å]	3.5	3.7	4.2	4.3	4.4
n_s	[$10^{12}\,\mathrm{cm}^{-2}$]	5.7	6	9.2	5	8.6
n_{3D}	[$10^{19}\,\mathrm{cm}^{-3}$]	3.8	3	3.7	1.7	2.5
E_{13}	[cm^{-1}]	-	9195	8640	8600	8177
FWHM E_{13}	[cm^{-1}]	-	700	570	500	470
E_{14}	[cm^{-1}]	-	-	10800	10900	10580

Table 6.3: Peak absorbance of samples with different QW thicknesses. The peak energies for higher ISBT were read out of the TM transmission; due to undulation of the transmission, the FWHM of those weak absorptions are only accurate to 10%. $I_{\alpha L}$ is the integrated absorbance from the measurement, μ_{12} the computed dipole matrix element and n_s the sheet carrier density calculated with Fermi's golden rule using $I_{\alpha L}$ and μ_{12}.

samples as a function of QW thickness along with theoretical ISBT obtained with *calcul-bande*. For the E_{12} transition, simulation and experiment are in good agreement. For higher states they are correct to within 10%. This discrepancy can be explained by the neglected depolarization shift and the uncertainties concerning the non-parabolicity effects.

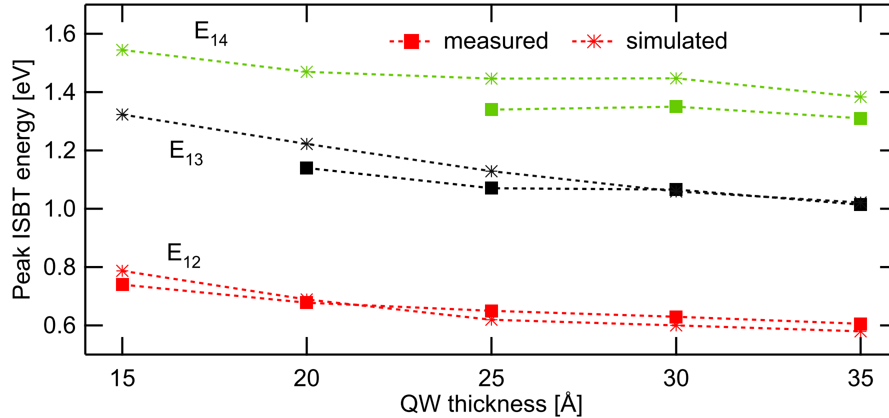

Figure 6.3: E_{12}, E_{13}, E_{14} of E1293, E1295, E1291, E1297, and E1295 along with computed ISBT energies obained with *calcul-bande*. The lines are a guide to the eye.

Conclusion The transmission of samples with different QW thicknesses was measured. For PAMBE samples, the obtained E_{12} ISBT energies are consistent with *calcul-bande* simulations. Compared to simulations, MOVPE samples had lower transition energies when grown on GaN buffers; later it was found that this discrepancy disappeared for

samples grown on an AlN buffer [Nicolay et al., 2007].

The relative absorbance linewidths of the first PAMBE samples investigated in this work were around 17%; later PAMBE samples had relative linewidths of down to 11% at 800 meV. To achieve such characteristics, a QW layer thickness of about 6 ML or 15 Å, along with an interfacial roughness below one ML is required. Although this relative linewidth is still wide when for example compared to the 4.7% of an InP based 5 μm QCD [Graf et al., 2006], a clear improvement was observed.

High ISBT energies of 834 meV (MOVPE) and 890 meV (PAMBE) were observed. Therefore, both growth techniques are adequate to obtain ISBTs at the telecommunication wavelengths of 1.55 μm (800 meV).

6.2 Rapid scan absorption of samples with $Al_xGa_{1-x}N$ barriers

As already discussed in chapter 4 a classical QWIP has a bound-to-quasi-bound transition with the second electron level being in resonance with the continuum. However such a resonant state is not easily obtained in a GaN QW due to the sawtooth potential of the barriers.

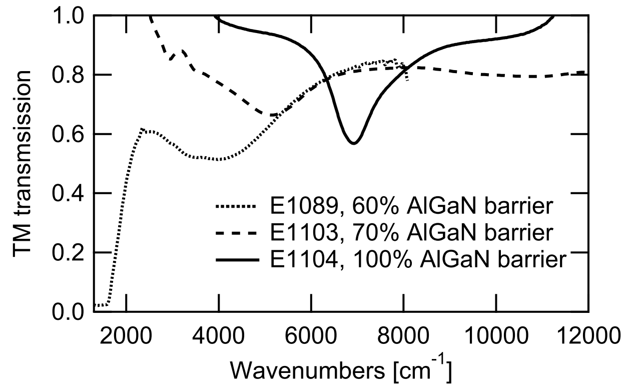

Figure 6.4: TM transmission taken with the spectrometer internal NIR source and the CaF_2 beam splitter for samples with 100% and 70% $Al_xGa_{1-x}N$ barriers and measured with the MIR source and KBR beamsplitter for the sample with 60% $Al_xGa_{1-x}N$ barriers.

In order to investigate the feasibility of a quasi-bound upper state in a $GaN/Al_xGa_{1-x}N$ heterostructure, PAMBE grown samples with different Al content in the barriers were investigated. The GaN QW thickness was held constant at 12.5 Å whereas the barrier Al concentration was 60% for E1089, 70% for E1103, and 100% for E1104. As seen in figure 6.4, the ISBT energy shifts as expected from 6927 cm^{-1} to 5180 cm^{-1} to about 3700 cm^{-1} with decreasing AlN content. The ISBT spectrum broadens with decreasing peak energy, which is an indication that the second state is approaching the continuum [Liu, 1993]. Additionally, there are higher levels contributing to the absorption spectrum in E1089. The sharp decrease of the transmission for this sample towards lower energies is caused by the absorption edge of sapphire; therefore it is also useless to continue the series towards lower

barrier Al contents, as the ISBT originating from a 12.5 Å QW would then be masked by the sapphire absorption.

Conclusion It was shown that the ISBT energy decreases for decreasing Al content in the barrier. For a barrier Al content of 60%, the ISB transmission is widely broadened as the upper level is getting closer to the continuum. However a clear bound-to-continuum transition was not observed due to the triangular barriers formed by the internal fields, impeding the design of a QWIP structure.

6.3 Electromodulated absorption of MOVPE samples

An alternative technique to normal rapid scan transmission measurements is the EMA technique described in section 5.2.1. To obtain significant results with EMA, it is crucial that the cap layer of the sample is an insulator to prevent a short-circuit between the two contacts where the modulation voltage is applied. The optimal situation is therefore a thin AlN cap layer; however, for samples with thin (about 5 nm) non-insulating $Al_xGa_{1-x}N$ caps, an absorption modulation could still be achieved if the external field was applied to a Schottky contact.

EMA measurements depend also on the internal fields. As discussed in section 2.1.2, a 2DEG forms at Ga-face AlN/(Al)GaN interfaces, including the AlN cap/active region interface. This 2DEG may screen the externally applied electrical field from the free carriers in the active region, thereby strongly decreasing their modulation. The experiment showed that for an active region grown on GaN, an AlN cap layer up to 30 nm still allows to probe the active region using EMA, resulting in a Lorentzian shaped ISB absorption. A sample with a 100 nm AlN cap however resulted in a broad EMA spectrum at around 4000 cm^{-1} which originates from the 2DEG at the interface between the active region and the cap.

In this section the EMA spectra of the three MOVPE grown samples described in table 6.4 are discussed. The QWs are Si-doped to nominally $5\times10^{18}cm^{-3}$ while the barriers are nominally undoped. Given that the MQW active region is grown on a GaN buffer, all three samples are tensile strained with the AlN content of the active regions being 80% AlN (A699), 56% AlN (A663), and 53% $Al_{0.98}In_{0.02}N$ (A767). Under inspection with a microscope, samples A633 and A699 show cracks, implying a partial relaxation of the epilayers, as opposed to sample A767 which has no cap layer and therefore a lower AlN content; the left panel of figure 6.5 shows an optical microscope image of A699 where the cracks are clearly visible.

Sample	Cap	QW / barrier [Å]	# periods	Barrier
A699	30 nm AlN	10 / 50	30	AlN
A663	30 nm AlN	16 / 20	30	AlN
A767	No cap	18 / 20	10	$Al_{0.98}In_{0.02}N$

Table 6.4: Structure parameters for MOVPE samples investigated by EMA.

For EMA absorption measurements all three samples were polished in 45° MPWs. On sample A663 and A699, two Ti/Al/Ti/Au (15/200/15/400 nm) ohmic contact stripes

of 0.5×6 mm^2 were evaporated and annealed followed by the evaporation of a Ti/Au (10/400 nm) contact of the same size in between. On sample A767, two Ti/Au contact stripes served as reference contacts. As A767 does not have an insulating AlN cap, the third contact evaporated between those two contacts was underlayed by a Si_3N_4 layer which was once 50 nm thick and once 100 nm thick (see section 5.2.1).

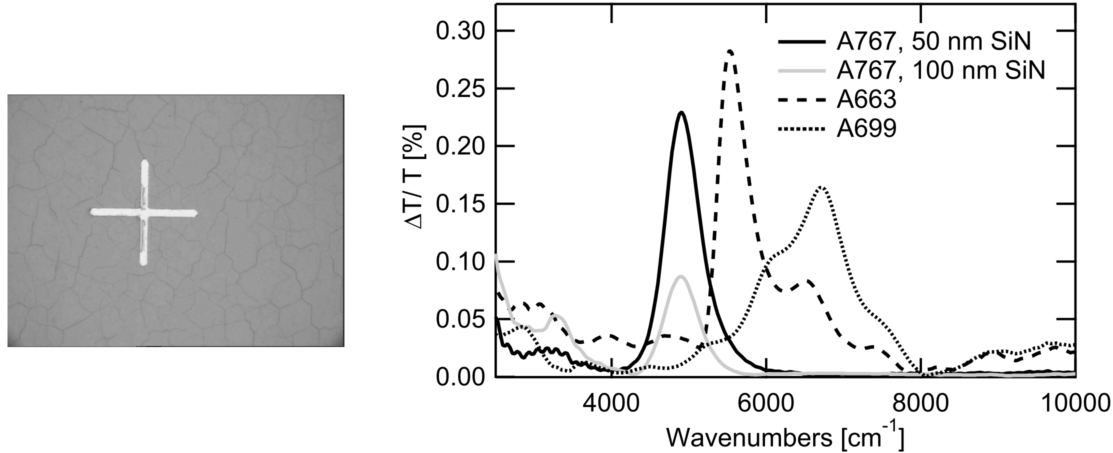

Figure 6.5: Left: optical microscope picture of the surface of A699; the cross is an alignement mark. Right: EMA of samples A767, A663 and A699 at 300K measured with a modulation amplitude of -2 V. Sample A767 was measured once with a 50 nm Si_3N_4 layer and once with a 100 nm Si_3N_4 layer on the cap.

Figure 6.5 shows the EMA spectra of all three samples measured with a modulation amplitude of -2 V. Sample A699 peaks at the highest wavenumber (6726 cm^{-1}), followed by sample A633 (5523 cm^{-1}) and sample A767 (4906 cm^{-1}), corresponding to the expected correlation with the nominal QW thicknesses of 10 Å (A699), 16 Å (A663), and 18 Å (A767). The FWHM of the absorption curves are 1170 cm^{-1} (A699), 630 cm^{-1} (A663), and 490 cm $^{-1}$ (A767). The absorption spectrum of the uncracked sample A767 is symmetric as opposed to the asymmetric spectra of the cracked samples A663 and A699. The different absorption strengths are caused by the varying insulator thickness between the metal contact and the active region, the decreasing oscillator strength for higher ISBT energies and the standing wave intensity (SWI) in the QWs probed by EMA. In the case of A767, the EMA signal is three times stronger when measured with a 50 nm cap compared to a 100 nm cap. This factor is to one part due to the linear potential drop of the external field across the insulator, to the other part due to the lower overlap between the SWI and the active region: as the SWI has a maximum at the metal/cap interface and a minimum 150 nm below, this overlap is lower for a 100 nm cap than for a 50 nm cap given that only the topmost QWs are probed by EMA.

Conclusion EMA of MOVPE samples peaking at wavenumbers up to 6726 cm^{-1} is demonstrated. Two different metalizations were used for the reference contacts: Ti/Au and Ti/Al/Ti/Au. Both resulted in comparable EMA spectra, wherefore the (more complex) Ti/Al/Ti/Au metalization was abandoned in later processes. Furthermore it was seen that a thinner insulating cap leads to stronger EMA absorption.

6.4 Electromodulated absorption for different external fields

During EMA measurements an external field is periodically applied to the sample. A higher voltage amplitude not only enhances the absorption strength but also modifies the already built-in electric field, which in turn can change the ISBT energy via Stark shift.

EMA measurements were carried out with sample A767: it is uncracked and therefore strained pseudomorphically to the buffer; its cap layer consists of a 100 nm insulating Si_3N_4 layer resulting in a low leakage current of about 0.1 nA in reverse direction, permitting efficient carrier modulation by the applied external field.

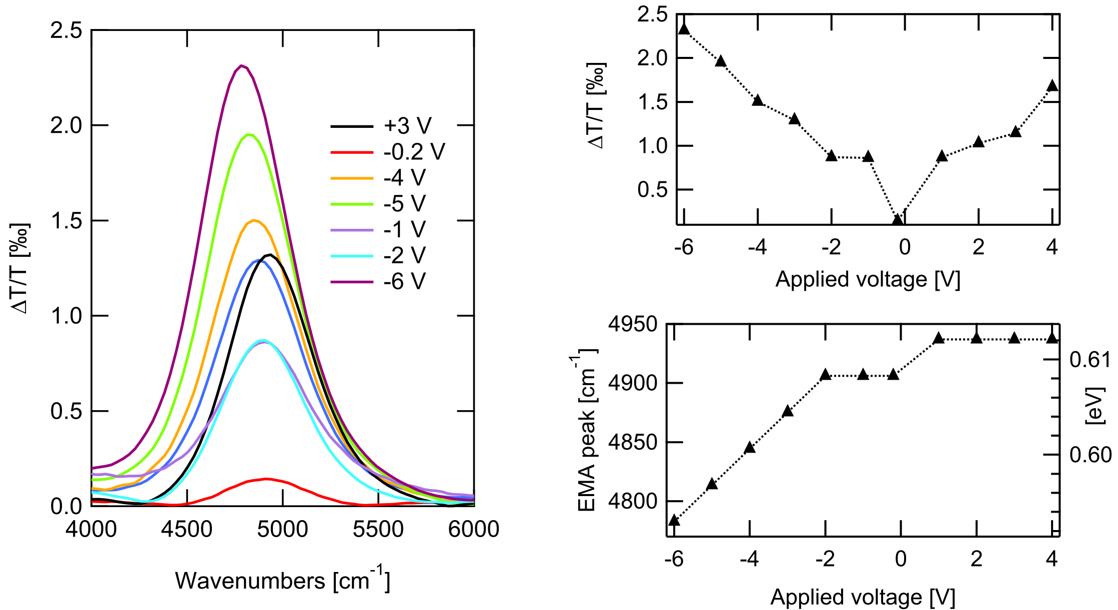

Figure 6.6: Left: EMA spectra of A767 for different voltage amplitudes. Right: Peak EMA (top) and EMA peak position energy (bottom) as a function of applied bias.

Figure 6.6 shows the EMA spectra of A767 for various voltage amplitudes from 3 to -6 V. The EMA gets stronger with increasing amplitudes (negative or positive) as seen in the top right panel of the same figure; this is due to the greater modulation depth and the increased modulation edge in the structure. There is a shift in the EMA peak position for voltage amplitudes from -2 to -6 V because of a partial screening of the internal field and hence a reduced Stark shift; for positive voltages, there was no measurable shift (see bottom panel) due to the increased leakage current in this direction and hence less efficient carrier modulation. Due to the differential measurement method ($(T_{xV} - T_{0V})/T_{0V}$) the increase of the EMA signal or the shift can not directly be read out of the slopes shown in figure 6.6 to the right.

6.5 Comparison of electromodulated and rapid scan absorption

As shown in section 3.1.3, the absorption strength depends on the doping level in the active QW. This is why for samples with a low QW doping density the ISBT absorption can be too weak to be characterized by a rapid scan 45° MPW measurement, requiring the more sensitive, but also more complex EMA method. To compare those two techniques two samples (E728 and E740) with an identical active region of 40 periods of 20 Å thick AlN barriers and 10 Å thick GaN QWs, but with different doping levels in the QWs were grown on a Si-doped $Al_{0.35}Ga_{0.65}N$ buffer layer. The QWs of E728 are nominally doped to $5{\times}10^{19}\,cm^{-3}$ whereas the QW doping level for E740 is nominal $1{\times}10^{19}\,cm^{-3}$; both samples are capped by an $Al_{0.35}Ga_{0.65}N$ layer, which is 5 nm thick for the lower doped E740 and 180 nm thick for E728. The conductive $Al_{0.35}Ga_{0.65}N$ cap layer for E740 needs to be thin in order to allow EMA measurements. An AlN concentration of 35% was choosen so that the growth can still be performed under Ga-rich conditions (see section 2.2.1), which facilitates the growth process.

Figure 6.7 shows high resolution X-ray diffraction of the two samples along with sample E739, which differs from E740 by a thicker cap layer of 140 nm $Al_{0.35}Ga_{0.65}N$. The nearly identical 0002 reflection of the three samples reveal the good reproducibility of the growth, and its distinct SL satellites are a sign for good material quality. Also, the extracted average period of $2.93{\pm}0.04$ nm is in good agreement with the nominal value of 3 nm. As the average Al-content of the SL is close to the one of the cap and buffer layers, the zeroth order of the SL is overlapping with peaks of the $Al_{0.35}Ga_{0.65}N$ layers. Reciprocal space mapping revealed that the whole structure is strained to the AlN layer deposited before the $Al_{0.35}Ga_{0.65}N$ layer on the sapphire substrate.

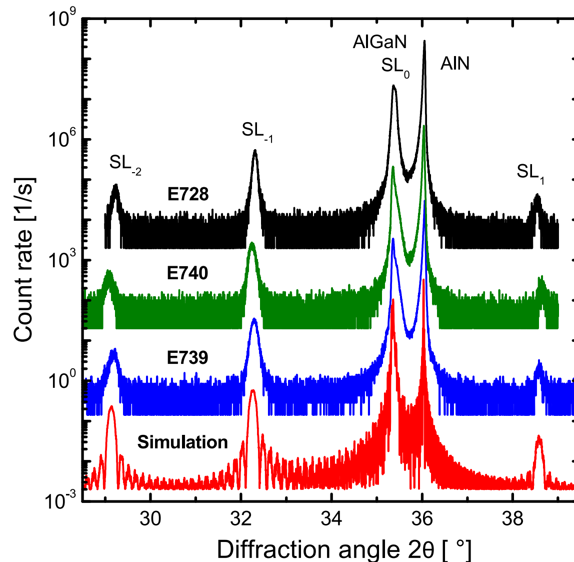

Figure 6.7: High resolution X-ray diffraction $\omega - 2\Theta$ scans of the (0002) reflection of samples E728, E739 and E740 along with a simulation.

Samples E728 and E740 were then polished into the standard 45° MPW geometry.

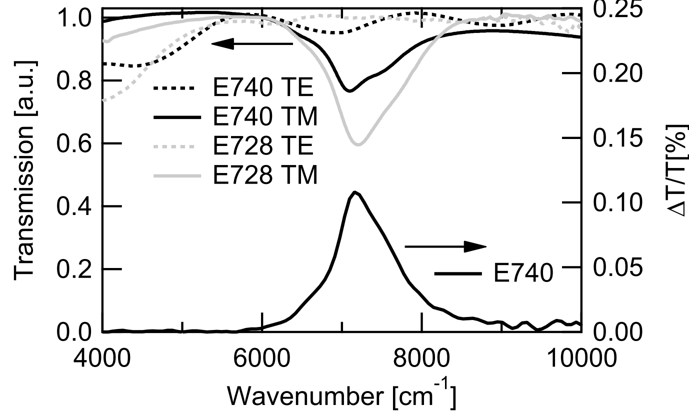

Figure 6.8: Top: polarized rapid scan transmission measurement for samples E728 and E740. Bottom: EMA of E740 taken beneath a MIS contact. All measurements are taken at room temperature.

Two Cr/Au electrical contacts were evaporated directly on the cap of the lower doped E740 and a third in between on a 50 nm thick intermediate SiO_2 layer. In figure 6.8 the room temperature absorption spectra of E728 and E740 are shown, measured in rapid scan transmission using a polarizer in between the spectrometer NIR source and the samples. As expected, the transmissions are fully TM polarized. Additionally, the EMA of E740 was measured using a rectangular voltage pulse train with a 50% duty cycle, a repetition rate of 13 kHz, a baseline of 0 V and a peak to peak amplitude of -2 V. The absorption peak energies of the two samples lie in good agreement at 7200 cm^{-1} (893 meV, 1.39 µm) for E740 and at 7100 cm^{-1} (880 meV, 1.41 µm) for E728. The FWHM of the rapid scan absorption is 880 cm^{-1} (110 meV, $2\Gamma/E_{12} = 12.3\%$) for E728 and 1000 cm^{-1} (120 meV, $2\Gamma/E_{12} = 14.1\%$) for E740, whereas the EMA of E740 has a slightly smaller FWHM $2\Gamma = 780\,cm^{-1}$ (98 meV, $2\Gamma/E_{12} = 10.9\%$).

The absorbance αL of the rapid scan absorption measurements is twice as strong for E728 than for E740. Given that the number of passes through a QW $N_P \times N_{QW} = 10 \times 40$, the ISBT oscillator strength $\mu_{12} = 3.06$ Å and the optical overlaps with the SWI (C =1.486 for E740 and C =1.43 for E728 beneath an air/semiconductor interface) are almost identical for both samples, this implies that their electron sheet carrier density n_s differs by a factor of two, which disagrees with the factor of five between the nominal doping densities. Calculating αL at the resonance based on the nominal sheet carrier density n_s using Fermi's golden rule results in $\alpha_{max} L = 0.55$ for E728, which is in good agreement with the measured value $\ln(T_{TE,max}/T_{TM,max}) = 0.51$. For E740, this calculation results in $\alpha_{max} L = 0.11$, which differs from the measured $\ln(T_{TE,max}/T_{TM,max}) = 0.26$. This implies that the doping of E740 is 2.4 times higher than the nominal value.

The absorbance of E740 obtained with EMA is about 260 times weaker than the one obtained with rapid scan transmission. This is due to an only partial depletion of the QWs and a probing of only the first few periods, which also explains the smaller linewidth of the EMA spectrum: due to inhomogeneities between individual QWs, SL structures tend to have broader linewidths with increasing number of contributing QWs.

Conclusion Although the samples E728 and E740 were fabricated 12 growth runs apart from each other, their absorbance spectra agree, which indicates good material quality and reproducibility. The spectral shape obtained from EMA and rapid scan measurements correspond well to each other; the EMA absorption strength is difficult to compare with the one obtained with rapid scan transmission due to EMA's partial depletion of the active region. However, this shallow depletion can be helpful to obtain additional information on the conduction band profile, as discussed in the following chapter.

Chapter 7

Probing the Band Structure using Electromodulated Absorption

As brought up in the previous chapter, this chapter discusses absorption measurements of short (two to ten period) SL PAMBE samples. It is shown that the free carrier density in the top most QWs can be modulated and the band structure can be probed by an external electrical field. ISBT energies of samples having an identical active region but different strain states are compared. In the second part a possible application of a five period sample as electro-optical modulator is discussed.

7.1 Electromodulated absorption of samples with two, five and ten periods

As already mentioned in the previous sections two assumptions are taken when comparing EMA signal strength to the computed absorption strength: the QWs are not fully depleted, whereby just a part of the sheet carrier density contributes to the EMA and only the topmost section of the active region is probed by the external electric field. To get a better insight in the EMA method, two sets of samples described in figure 7.1 and table 7.1 with two, five, and ten periods were grown by PAMBE on a sapphire substrate; once on an AlN template, once on a GaN template. One period consists of a 15 Å AlN barrier and a 15 Å GaN QW nominally doped to $10^{19}\,\mathrm{cm}^{-3}$. Between the template and the active region, a 300 nm thick GaN contact layer doped to $5 \times 10^{17}\,\mathrm{cm}^{-3}$ was deposited for both sets; this results in compressive strain for the samples grown on an AlN template and in tensile strain for the samples grown on a GaN template, except for E890 (ten periods on GaN), which shows cracks on the surface, indicating a partial relaxation of the active region. The samples were then polished into 45° MPWs followed by the evaporation of an metal semiconductor (MS) contact stripe directly on the last AlN layer and a metal insulator semiconductor (MIS) contact stripe on an intermediate 100 nm thick Si_3N_4 layer (see also section 5.2.1); both contacts have a Ti/Au (5/200 nm) metalization.

EMA of MIS contact Figure 7.2 shows EMA measurements of the GaN template samples illuminated below the MIS contact while applying a modulated square voltage with an amplitude of -2V; here, negative voltage stands for a lower potential at the illuminated

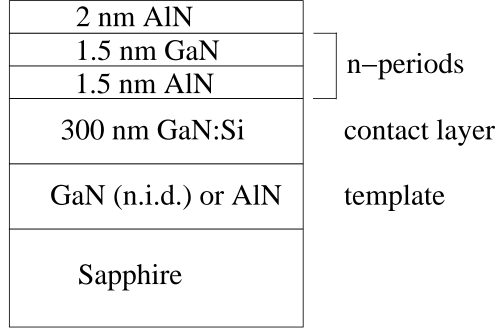

Figure 7.1: Structure of the short SL samples; the active region is either grown on a 10 µm GaN or on a 1 µm AlN template.

Sample	E882	E885	E887	E888	E889	E890
Periods	5	2	5	10	2	10
Template	AlN	GaN	GaN	AlN	AlN	GaN

Table 7.1: Template material and number of periods of the short SL samples. One period contains a 15 Å GaN QW and a 15 Å AlN barrier.

contact compared to the dark reference contact. Although the QW and barrier thicknesses and doping of the three samples are identical, two different absorption peak energies are measured: the samples with five and ten periods have a narrow absorption peak at $6850\,\mathrm{cm}^{-1}$ (850 meV, 1.46 µm) with a FWHM of $509\,\mathrm{cm}^{-1}$ and $523\,\mathrm{cm}^{-1}$ corresponding to the simulated E_{12} ISBT energy of a 15 Å GaN QW; the two period sample, on the other hand, exhibits a broader absorption peaking at $4500\,\mathrm{cm}^{-1}$ (560 meV, 2.2 µm). This absorption is attributed to the 2DEG located at the interface between the lowest AlN barrier and the underlying GaN contact layer and is therefore named 2DEG absorption.

As these samples resemble a GaN channel HEMT with its $Al_xGa_{1-x}N$ barrier replaced by an AlN/GaN SL, approximate values for the 2DEGs E_{12} transition can be calculated with the triangular potential approximation (3.36). Assuming a strained $Al_{0.5}Ga_{0.5}N$/GaN interface and a constant electric field F in the active region results in $F = 5.3\,\mathrm{MV/m}$ and $E_{12} = 620\,\mathrm{meV}$ ($5000\,\mathrm{cm}^{-1}$). This is in reasonable agreement with the measured EMA peaking at 520 meV ($4500\,\mathrm{cm}^{-1}$). The large linewidth of the measured 2DEG absorption spectrum is caused by additional 2DEG transitions into higher lying states.

The different absorption spectra with respect to the number of QWs can be explained by conduction band bending and total SL thickness. Contacts on the AlN cap lead to an upward band bending at the top of the SL, and the area probed by EMA corresponds to the edge of the depletion region below the contact. Figure 7.3 shows the schematic conduction band of a two period sample (left) and a five period sample (right).

For the two period sample, the upward band bending due to the Schottky barrier fully depletes both QWs already at zero applied field, so that free electrons are transferred to the 2DEG: the external electric field modulates the charge in the 2DEG and only the ISB absorption in the 2DEG is observed. For the five and ten period samples, the two topmost QWs are also fully depleted by the upward band bending, whereas the rest of

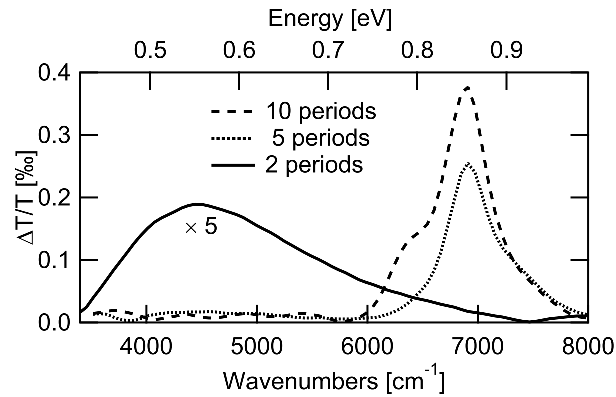

Figure 7.2: Room temperature EMA measured with the MIS contact for the two, five, and ten period samples grown on a GaN template

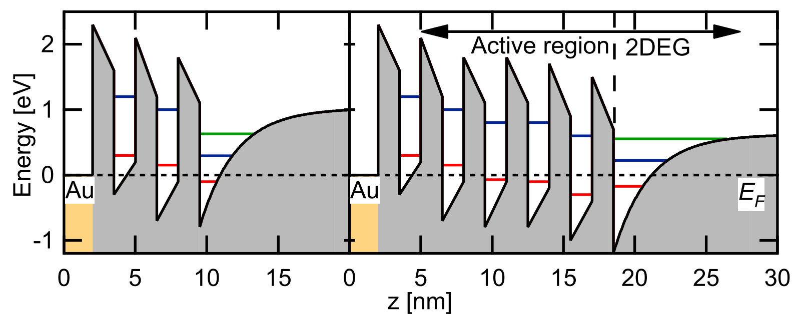

Figure 7.3: Schematic drawing of the conduction band of a sample with a two period (left) and five period (right) SL. Due to the Schottky barrier on the sample surface and the resulting upward band bending, ISB absorption only takes place in the 2DEG (single 'QW') for the two period structure, whereas for the five period structure ISB absorption mainly takes place in the SL, where a total of three QW contribute to the absorption.

the SL remains in 'flat band' condition. In this case, the external electric field modulates the charge in a minimum of three QWs. We conclude this because the 2DEG absorption is not observed for the ten period sample, and shows up only weakly for the five period sample.

EMA of MS contact In the following experiment the MS contact was illuminated and the MIS served as reference contact. In this configuration the Schottky barrier of the MS contact leads to an even more distinctive upward band bending of the topmost QWs. Figure 7.4 shows the normalized EMA measurements of the samples grown on a GaN (left) and on an AlN template (right). For the two period samples the measurements obtained while illuminating the MIS contact are also depicted. By comparing those spectra the following statements can be made: for the sample with ten periods, the ISB absorption in the QWs is dominant and the 2DEG absorption is not observed up to a modulation amplitude of −6 V; the depletion region remains therefore always smaller than the SL thickness (32 nm). For the MS measurement of the five period sample with a 17 nm thick active region, absorption in both the SL and the 2DEG are visible, hence the depletion region reaches the 2DEG. In the two period sample, finally, the 2DEG signal becomes

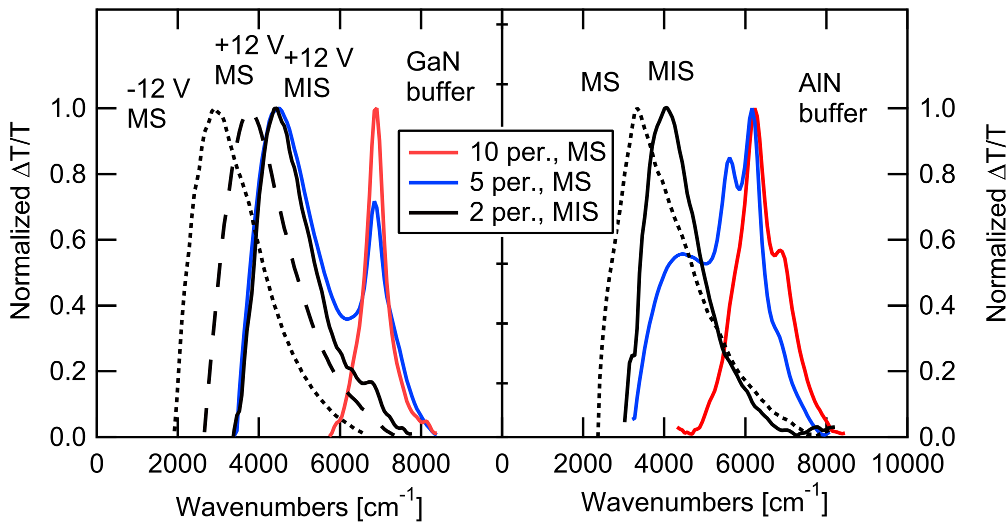

Figure 7.4: EMA of the samples having a QW of 15 Å grown on a GaN (left) and on an AlN template (right). For the two period samples EMA measured with illumination of the MIS and MS contact is shown. For five and ten period samples only EMA measured while illuminating the MS contact are shown.

the dominant feature of the absorption spectrum, whereas the SL signal is almost entirely absent. For the samples grown on GaN buffer a high positive voltage amplitude of 12 V applied to the MIS contact introduces a reduction of the conduction upward bending in the SL, electrons are moving towards the sample surface. Those electrons give now rise to an absorption shoulder around 6850 cm^{-1} in the SL.

The 2DEG signal beneath the MS contact peaks at a lower energy than the one below the MIS contact. This is due to a decrease of the Stark shift beneath the MS contact,

which is caused by the increased conduction upward band bending in comparison to the MIS contact. Additionally, the 2DEG EMA peak shifts as function of the external voltage amplitudes. This can be assigned to an increase (positive amplitudes) or decrease (negative amplitudes) of the zero field Stark shift (see section 6.4).

This effect was not measured for the ISB transition at 6850 cm^{-1}. This indicates that the states in a triangular potential are easier Stark shifted in comparison to a state in a rectangular QW. This feature is explained by the substantial diagonal component of the ISBT in the 2DEG.

EMA as a function of modulated charge density Figure 7.5 shows the integrated EMA I_a as a function of the sheet carrier density n_s, calculated following Fermi's golden rule using the measured peak absorption E_{peak}, the simulated dipole matrix elements $\mu_{12,sim}$ and the number of passes $N_P = 10$. The lower curve represents a single absorbing QW at 600 meV, corresponding to the two period sample with the completely depleted SL; the upper curve is calculated for a SL with four QWs absorbing at 850 meV, corresponding to the ten period sample with its two topmost QWs completely depleted (see also figure 7.3) under the assumption of a 20 nm modulation depth.

Sample	$I_{a,meas}$ [eV]	E_{peak} [eV]	$\mu_{12,sim}$ [Å]	n_s [cm^{-2}]
E885 (2 periods)	2.7×10^{-4}	0.60	3.88	2.2×10^{13}
E890 (10 periods)	2.1×10^{-4}	0.85	3.54	1.5×10^{12}

Table 7.2: Parameters used for the calculation of the absorbance for the two and ten period samples with a GaN template under an MS contact. $I_{a,meas}$ is the measured integrated EMA, E_{peak} the measured peak EMA energy, $\mu_{12,sim}$ the simulated dipole matrix element and n_s the sheet carrier density.

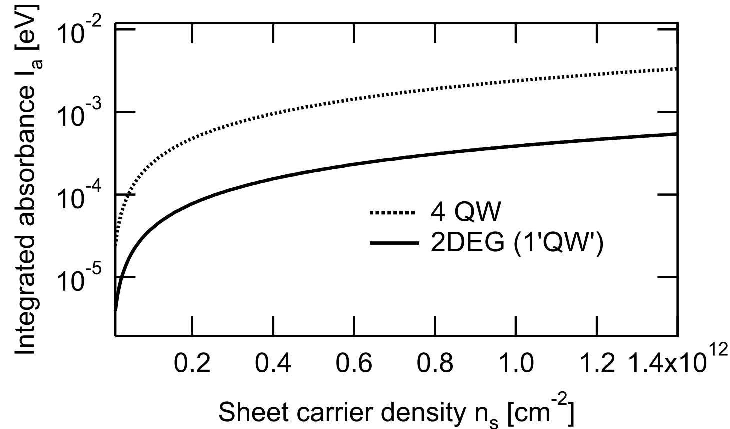

Figure 7.5: Computed value of the integral over the absorbance as a function of sheet carrier density.

As $I_{a,meas} = 2.7 \times 10^{-4}$ eV for the two period sample and $I_{a,meas} = 2.1 \times 10^{-4}$ eV for the ten period sample, the sheet carrier density n_s taken from figure 7.5 is approximately

$9 \times 10^{10}\,\mathrm{cm}^{-2}$ for four QWs contributing to EMA and $1.25 \times 10^{12}\,\mathrm{cm}^{-2}$ for the two period sample's 2DEG. The nominal n_s of the ten period sample is however $1.5 \times 10^{12}\,\mathrm{cm}^{-2}$, and the n_s of the 2DEG is $2.2 \times 10^{13}\,\mathrm{cm}^{-2}$ according to CV measurements (refer to appendix E). This leads to the conclusion that only about 6% of the free carriers are modulated by the applied field and therefore contribute to the EMA, both for the SL and the 2DEG.

Conclusion It was shown that besides measuring weak absorptions, the EMA technique can also be used to investigate the conduction band profile close to the surface and to influence its shape. It was seen that only carriers in a well defined depth that depends on the insulator thickness, contact conduction band bending, and external field modulation amplitude contribute to the signal. These findings are later used to design an electro-optical modulator described in section 7.2.

7.1.1 Comparison of samples grown on GaN and AlN template

As mentioned above, two different sets of samples were grown, one on a GaN and the other on an AlN template. The samples grown on AlN template have a broader EMA spectral shape in comparison to samples grown on GaN (figure 7.4). Although both sets have the same nominal QW thickness of 15 Å , the EMA of the five period GaN template sample peaks at $6850\,\mathrm{cm}^{-1}$ whereas the five period AlN template sample peaks around $6170\,\mathrm{cm}^{-1}$, as is seen in figure 7.6. The ISBT of E966, an AlN template sample with a reduced QW thickness of 12.5 Å, peaks at nearly the same energy than the 15 Å QW GaN template sample E887; this further corroborates the influence of the template material on the ISBT energy.

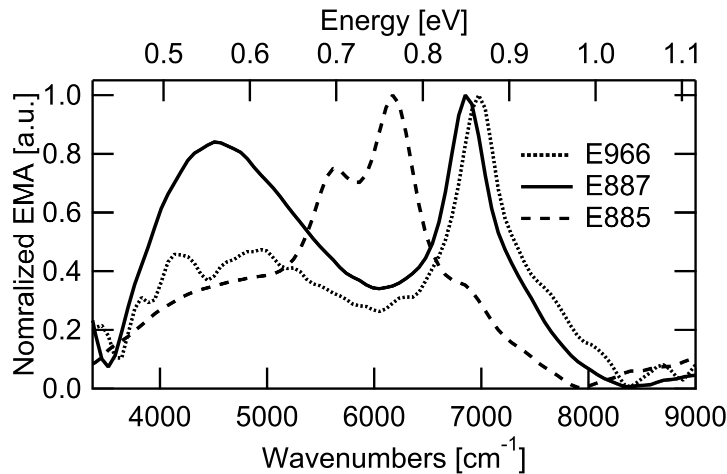

Figure 7.6: EMA measurements showing an ISBT shift between E885 (AlN buffer) and E887 (GaN buffer) for a QW thickness of 15 Å. E966 (AlN buffer) has nominal a 12.5 Å QW. The low energy peak is the 2DEG absorption.

The direction of this shift qualitatively agrees with an estimated Stark shift caused by the internal fields. In GaN QWs grown on GaN the internal fields and thus the Stark shift are maximal. In a strained GaN QW grown on AlN the spontaneous polarization P_{sp}

and the piezoelectric polarization P_{piezo} attenuate each other, resulting in a weaker Stark shift.

Computing the ISBT energy E_{12} for a 15 Å QW with *calcul-bande*, once with an internal field $F_{int} = 6.95$ MV/cm (GaN template) and once for $F_{int} = 6.14$ MV/cm (AlN template), results in a shift of only 12 meV. In comparison to the measured shift of 84 meV, this shift is 7 times smaller. There are other effects, which may red-shift the ISBT energy in a strained QW in comparison to a relaxed QW. In the case of biaxial strain the ratio c/c_0 (see (2.7)) for a strained GaN QW increases, leading to about 1% thicker QW. This template dependent red-shift was however not further investigated because E885, E887, and E890 were the only available PAMBE samples grown on GaN templates investigated at the time.

Note that the described phenomena lead to a smaller ISBT energy for a PAMBE grown sample on AlN. With MOVPE the opposite is the case: samples grown on AlN templates show higher ISBT energies than those on GaN/sapphire. The AlN buffer leads to better interface quality; the QW ground state is not lifted up [Nicolay et al., 2007]. This effect is stronger than the Stark shift, explaining the discrepancy between MOVPE and MBE.

7.2 Modulator prototype

In figure 7.7 the EMA of the five period sample E887 is shown for a modulation voltage amplitude of −1 V. It is largest around the ISBT at 6850 cm^{-1} (850 meV). To find out which bias polarity reduces the ISB absorption, rapid scan transmission measurements where carried out while applying a DC bias voltage to the sample. To compensate the lower sensitivity compared to EMA measurements, the voltage amplitude was set to ±6 V; the obtained differential transmission $(T_{-6} - T_{+6})/T$ shown in figure 7.7 is however still noisier than the −1 V amplitude EMA measurement. At the ISBT energy, the negative bias

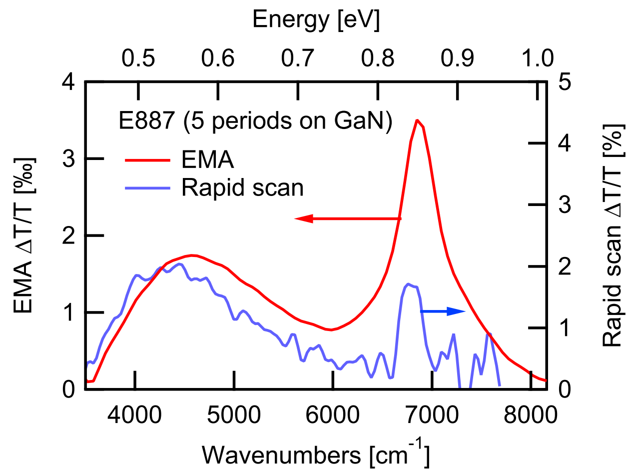

Figure 7.7: Differential transmission of E887 measured at the MS contact. The EMA ΔT is obtained with a voltage square wave with −1 V amplitude and a 0 V baseline, the rapid scan ΔT by subtracting the transmission measured with a +6 V bias from the one measured with a −6 V bias.

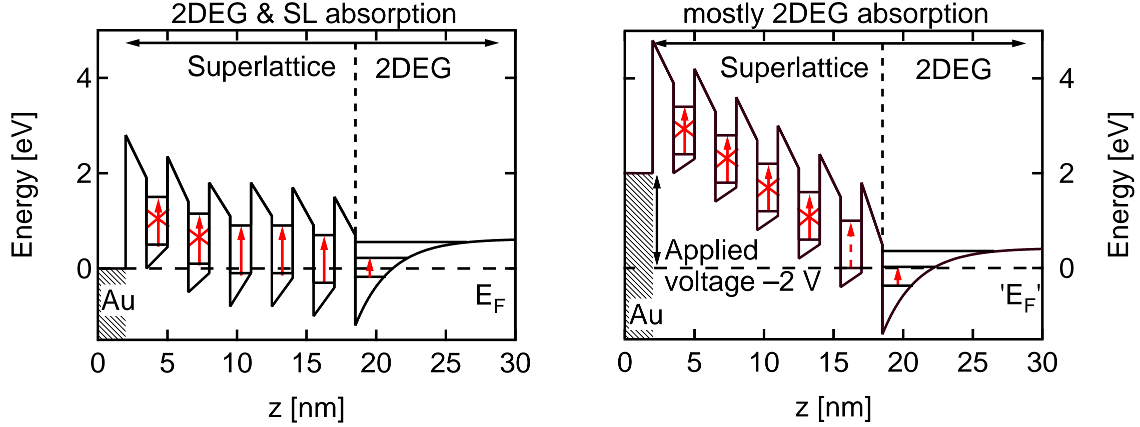

Figure 7.8: Schematic conduction band diagram of an electro-optical modulator using ISB transitions in a GaN/AlN SL. The applied voltage is 0 V for the left panel, −2 V for the right panel.

rapid scan transmission T_{-6} is higher compared to the positive bias rapid scan transmission T_{+6}, meaning that negative bias voltages quench the ISB absorption. This is consistent with the band bending induced by the bias voltage: as seen in figure 7.8, the conduction band is already slightly lifted towards the contact at zero bias due to the Schottky barrier; therefore, the topmost QWs are above the Fermi level, have a negligible ground state population and do not contribute to the ISB absorption. When a negative voltage is applied to the contact, this upward bending is enhanced, more QWs are lifted above the Fermi level and the ISB absorption is weaker compared to zero bias. This behavior can be used as electro-optical modulator: at 0 V, the absorption at the ISB energy is stronger, the modulator is in its off-state (normally off). When applying a negative bias voltage, the absorption diminishes, the modulator is in its on-state. A speciality of this design is its spectral selectivity: the transmitted light is only modulated at energies close to the ISBT energies (both from the QW and the 2DEG).

Based on the spectral EMA measurements, the range for the number of periods of such a modulator can be determined: as seen in figure 7.4, the 2DEG at the active region/buffer interface is not modulated for bias voltages up to 6 V in the case of a ten period sample. In a thick SL of ten or more periods, the lowest lying QWs (towards the buffer) do not contribute to the EMA. For the two period sample, the ISBT absorption is only weakly modulated, the conduction band bending (introduced by the Schottky barrier) lifts up the ground states of the QWs close to the surface. Consequently, a sample having between five and ten periods is an appropriate choice.

A rough estimation of the 'on-off ratio' is obtained from the rapid scan transmission measurement: for a −6 V bias, the transmission is 1.5% lower than for a +6 V bias, corresponding to an on-off ratio of $20 \times \log(1/0.985) = 0.13$ dB. This value can be improved using an appropriate waveguide, as discussed in the next section.

7.2.1 Waveguide

To increase the on-off ratio of the SL/2DEG electro-optical modulator presented in the previous section, the five period SL can be embedded in a ridge waveguide. Although this does not improve the absorbance difference $\Delta\alpha = \alpha_{on} - \alpha_{off}$, the ratio between the on- and off-state absorption ($e^{-\Delta\alpha\times L}$) becomes considerably larger due to the increased optical interaction length L between the optical field and the active region in a ridge waveguide compared to an MPW.

In a lateral ridge waveguide, which can be described as a laterally confined dielectric slab waveguide, the active region is embedded in a core layer sandwiched between two layers with lower refractive indices in order to confine the radiation. For the modulator, the GaN contact layer (n=2.3) is the dense waveguide core (to which the SL is attached). The confinement on the substrate side is provided by an AlN (n=2.1) buffer layer. On top of the active region, an SiO_2 (n=1.47) insulator layer is deposited, followed by a Ti/Au metalization.

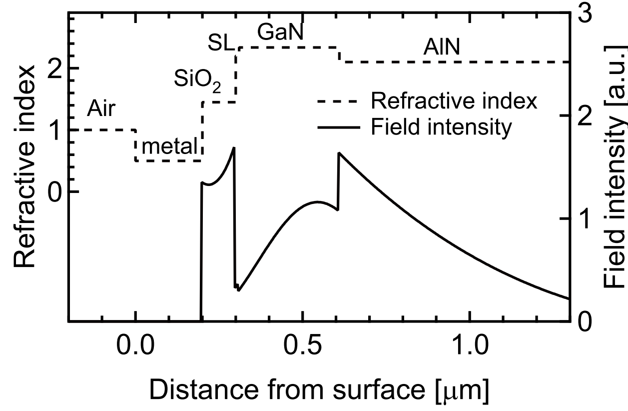

Figure 7.9: Simulation of the fundamental TM mode for E966.

Due to the AlN buffer and the five period repetitions, E966 is a promising candidate for a ridge waveguide modulator. Figure 7.9 shows a one dimensional slab waveguide simulation of sample E966 calculated with the Schrödinger solver *calcul-bande* adapted to solve the one-dimensional wave equation of a TM mode obtained from Maxwell's equations in the absence of sources. According to the simulation, only one TM mode propagates in this waveguide. It has an effective refractive index $n - i\,k = 2.10 - i\,4.01 \times 10^{-4}$ resulting in waveguide losses of $\alpha_{wg} = 4\,\pi/\lambda \times k = 35.2\,\mathrm{cm}^{-1}$ for $\lambda = 1.43\,\mu$m. The overlap between the active region and the TM mode is C=0.36%; this low value is not surprising comparing the SL thickness of 12.5 nm to the effective wavelength in the active region, which is 1430 nm/2.2=650 nm (2.2 is the refractive index of the active region). To estimate the performance of the modulator, the 3D modulation absorbance difference $\Delta\alpha_{3D}$ is calculated based on the rapid scan transmission of sample E966 in figure 7.7, from which the differential absorption efficiency is taken to be $\Delta\eta = 0.02$. Using

$$\Delta\eta = \Delta\alpha_{2D} \times \frac{\sin^2\Theta}{\cos\Theta} \times N_p \times N_{QW} \tag{7.1}$$

results in a dimensionless differential QW absorbance $\Delta\alpha_{2D} = 1.55 \times 10^{-3}$, where $\Theta = 37°$ is the propagation angle in the active region for a 45° MPW, $N_p = 10$ is the number of passes and $N_{QW} = 3$ is the number of periods affected by the applied voltage. The factor $\cos\Theta$ seems to give an unphysical result when $\Theta \to 90°$, as is the case in a ridge waveguide; this is because α_{2D} is the absorption constant for light passing through one QW, resulting in an infinitely long passing length for $\Theta = 90°$. Therefore, a bulk absorption constant $\Delta\alpha_{3D}$ with $\Delta\eta = \Delta\alpha_{3D} \times L/\cos\Theta$ is defined to calculate the differential absorption efficiency of a ridge waveguide [Liu, 2000]. For one QW,

$$\Delta\alpha_{3D} \times \frac{L_p}{\cos\Theta} = \Delta\alpha_{2D} \times \frac{\sin^2\Theta}{\cos\Theta}, \tag{7.2}$$

results in $\Delta\alpha_{3D} = 5167\,\mathrm{cm}^{-1}$, where $L_p = 3 \times 10^{-7}\,\mathrm{cm}$ is the length of one period, and $\Theta = 90°$ is the propagation angle in the ridge waveguide. For a waveguide length of $L_{wg} = 0.2\,\mathrm{mm}$, the on-off ratio is calculated to be $20 \times \log(e^{N_{QW}\,\Delta\alpha_{3D}\,C\,L_{wg}}) = 9.7\,\mathrm{dB}$, and the waveguide losses $20 \times \log(e^{-\alpha_{wg}\,L_{wg}}) = -6\,\mathrm{dB}$.

Conclusion An electro-optical modulator was proposed based on a transistor like structure. Although the device was tested in MPW geometry, this modulator could clearly influence the transmission of light in a narrow band around 800 meV. To improve the modulation depth of this prototype, future work will concentrate on placing the modulator structure in a ridge waveguide.

Chapter 8

Photodetectors

In this chapter, samples giving rise to a photovoltaic response are discussed. Most of them were grown by PAMBE. As shown in section 3.2.1, the photovoltage is proportional to the number of QWs N_{QW}, the QW thickness t_{QW}, the QW 3D doping density n_{3D}, and the figure of merit $\Pi\,\tau$. To verify this theoretical dependences and to investigate the influence of individual structure parameters on $\Pi\,\tau$, three sample series, each with a single varying parameter, were grown.

As PV measurements on processed mesa structures resulted in weaker signals with nearly identical spectral shape compared to unetched stripe contact structures, most samples were not etched into mesa structures, so that no conducting $Al_xGa_{1-x}N$ or GaN buffer layer is required. However PV measurements across two top contacts require that the cap has a low conductivity, otherwise the contacts are short circuited. The growth conditions of both PAMBE and MOVPE changed several times, wherefore a comparison across different sample series is not always possible; a short discussion on the influence of the PAMBE growth temperature on the PV signal strength can be found in appendix I.

8.1 Comparison of mesa and stripe process

In this section, the PV measurements of a sample processed into mesas with an etched bottom contact and into stripes without etching are compared.

The investigated sample E740 has an active region consisting of a 40 period SL with 10 Å GaN QWs doped to $2.4{\times}10^{19}\,\mathrm{cm}^{-3}$ and 20 Å AlN barriers sandwiched between a 5 nm cap and a 250 nm buffer, both $Al_{0.35}Ga_{0.65}N$. This conductive buffer layer allows a vertical contacting of the active region with a mesa process. One half of E740 was processed into $(200 \times 400)\,\mu\mathrm{m}^2$ mesas; a Ti/Au contact was evaporated on the mesas and an ohmic Ti/Al/Ti/Au on the etched area in between. On the other half, Cr/Au contact stripes were evaporated on the unetched sample surface. Both pieces were then polished into 45° MPWs for optical characterization.

Figure 8.1 shows the normalized PV signal for both the mesa and the stripe process along with the TM polarized transmission measured with a 45° MPW. The two processes give rise to a PV signal of almost the same spectral shape, despite the different contact areas and number of passes in the active region.

At 10 K the PV peaks at $7320\,\mathrm{cm}^{-1}$ (915 meV, 1.39 µm) for both processes and has a

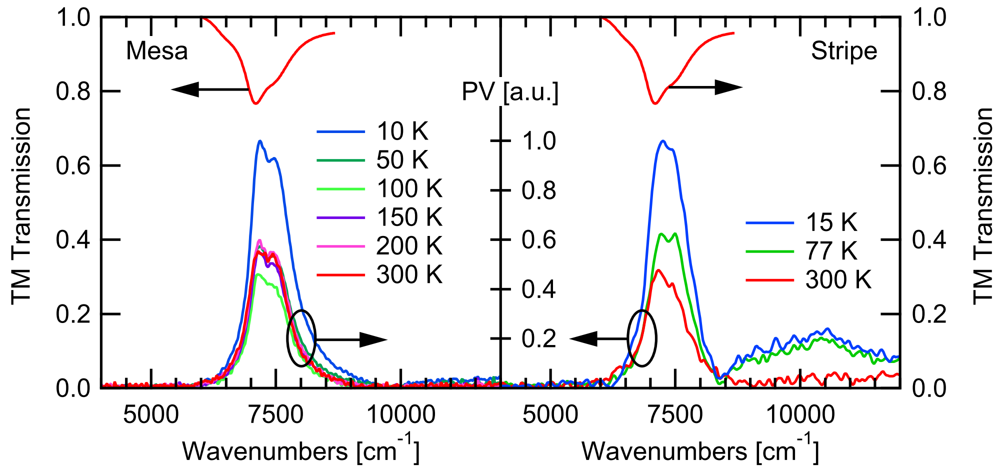

Figure 8.1: Normalized PV and TM transmission of E740 at different temperatures. Left: mesa process PV. Right: stripe process PV. For comparison, the transmission is shown in both panels.

FWHM of 720 cm^{-1} (90 meV). The PV signal for the mesa process is smaller than for the stripe process (not visible in figure 8.1), which is consistent with the stripe process's higher number of passes in the active region. The defect signal at 10000 cm^{-1} is stronger for the stripe process, which is possibly due to the thicker $Al_xGa_{1-x}N$ buffer layer in comparison to the remaining buffer for the etched mesa process. The transmission peaks close to the PV and has an asymmetric shape, the latter being an indication of a small growth rate drift (see also section 6.5), which also explains the twin peaks of the PV signal. The PV is highest at 10 K, and drops to about half of this peak value at 50 K, where it remains for higher temperatures. At 300 K, the PV of the mesa process is redshifted by 50 cm^{-1} with respect to the stripe process.

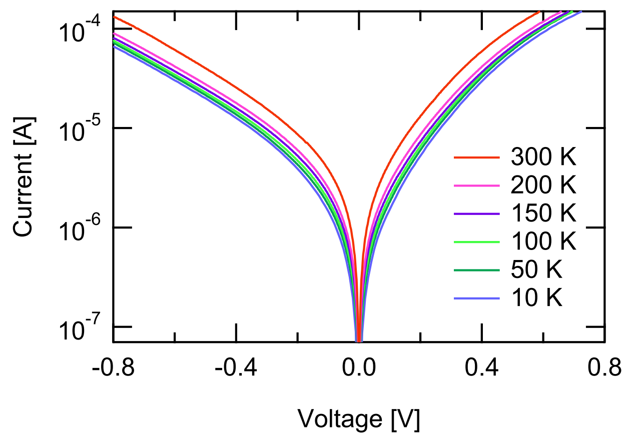

Figure 8.2: I-V measurement of the E740 mesa process at different temperatures.

Figure 8.2 shows the measured I-V curves of the mesa process for different temper-

atures; they are determined by the active region (not like in the stripe process). As expected, the resistance decreases with increasing temperature. Additionally, photoconductive measurements were taken while applying a bias voltage across the active region; no PC gain was seen, however the noise increased significantly.

Conclusion The PV signal of a mesa process has a nearly identical shape compared to the one measured with a stripe process, but the stripe process leads to a stronger signal due to its larger area and longer interaction length, wherefore most subsequent samples were not processed into mesa structures.

8.2 Different thickness of AlN barriers

To study the influence of different AlN barrier thicknesses on PV, a series of samples was grown by PAMBE with identical structure parameters except for the barrier thickness, as listed in table 8.2. The QWs are 15 Å thick and nominally doped to 10^{19} cm^{-3}, the buffer (1.1µm) and cap (50 nm) material is AlN, and the number of QW/barrier periods is 40. To mask the influence of growth conditions changing with time, the series was not grown in sequence with increasing barrier thickness. It was however not possible to have identical growth conditions for all samples, as a higher overall Al content in the active region requires a higher growth temperature as well as growth interruptions between consecutive layers: whereas the 7.5 Å and 15 Å samples E1206 and E1209 were grown without interruption, samples E1211 (30 Å) and E1210 (70 Å) have an interruption of 1 s and sample E1208 (150 Å) one of 5 s (see also section 2.2).

Sample	E1206	E1208	E1209	E1210	E1211
Barrier width [Å]	15	150	7.5	70	30
Peak position [cm^{-1}]	6350	6370	6700	6350	6295
FWHM [cm^{-1}]	1065	1030	1680	770	1050
MQW AlN content	50%	90%	33%	82%	67%

Table 8.1: Nominal AlN barrier thickness and measured PV peak position and FWHM of E_{12} taken from the right panel of figure 8.3 for samples E1206 – E1211. The last line gives the overall AlN content of the active region.

Measured spectral PV For temperature dependent PV measurements, the samples were cooled down to 10 K and then heated to the measurement temperature. Figure 8.3 shows the measured PV signal at 150 K, where the signal is strongest for all samples but E1211. On the left panel, the spectra are shown as semilogarithmic plot, the right panel shows the main peak normalized to one on a linear scale. All samples have a PV peak at about 6350 cm^{-1}, which is in good agreement with the simulated $E_{12} = 6340\,\mathrm{cm}^{-1}$ of a 15 Å QW. The shoulder around 10000 cm^{-1} is due to an ISBT into a higher lying state in the QW and the peak at 12600 cm^{-1} is a replica of the $1 \rightarrow 2$ ISBT. Those features are discussed in section 8.9. The broad peak around 20000 cm^{-1} is due to the yellow band in the GaN QW [Reshchikov and Morkoc, 2005]. The PV signal is strongest

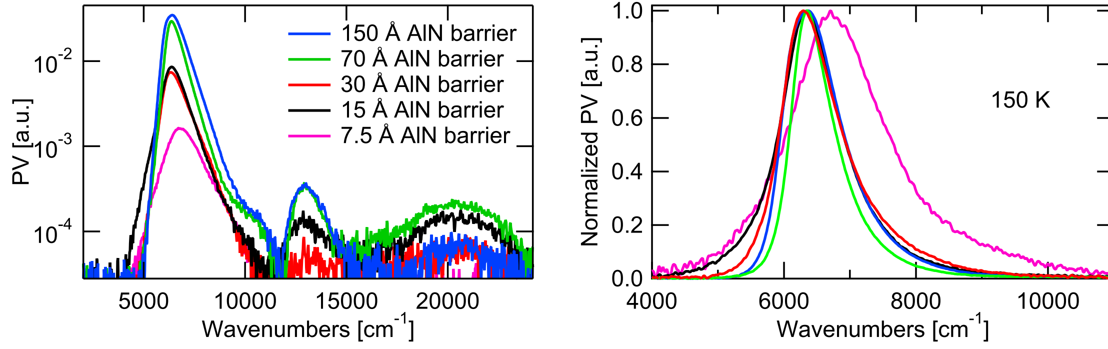

Figure 8.3: Left: measured PV spectra at 150 K of the sample series with barrier thickness ranging from 7.5 Å to 150 Å. Right: the same spectra normalized by the blackbody of the spectrometer NIR source and normalized to one.

for samples E1210 (70 Å) and E1208 (150 Å); this shows that the PV is not connected to interwell tunneling processes, as the tunneling probabilities across one barrier for the second electron level estimated using (4.1) is negligibly small: 2.4×10^{-39} for the 150 Å barrier respectively 7.5×10^{-19} for the 70 Å barrier.

As seen in the right panel of figure 8.3, the PV of sample E1209 (7.5 Å barrier) peaks at 6700 cm^{-1}, whereas all other samples peak around 6350 cm^{-1}. This shift is caused by the relaxation of E1209's active region: it has an overall AlN content of 33%, and is therefore highly strained to the AlN buffer as opposed to samples with thicker barriers having a higher overall AlN content. Relaxation of a GaN QW grown pseudomorphically on AlN reduces the magnitude of the piezoelectric field F_{piezo} in the QW, leading to a stronger internal field in the QW (see also (3.39)) and thus a higher ISBT energy. The larger amount of broadening of sample E1209 also indicates a gradual relaxation.

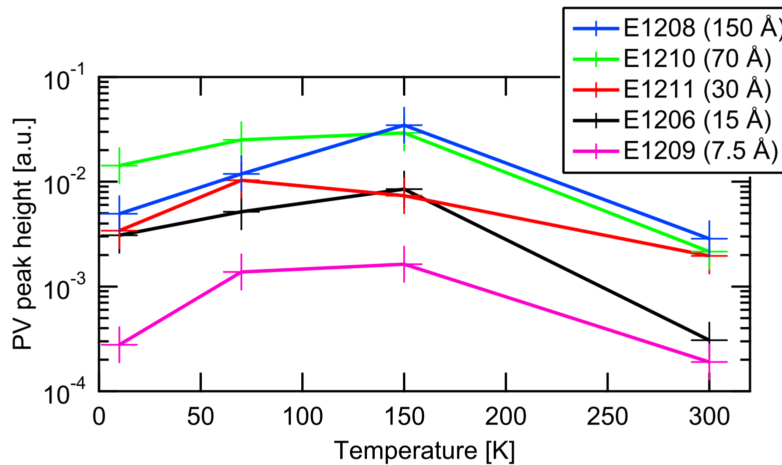

Figure 8.4: Peak ISBT height for samples with different AlN barrier thicknesses as a function of temperature.

In figure 8.4 the temperature dependence of the E_{12} transition peak height is depicted.

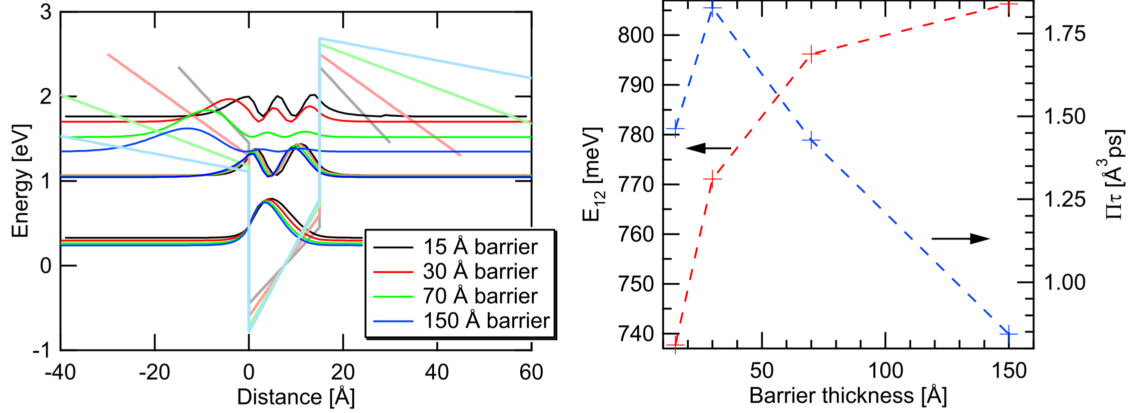

Figure 8.5: *calcul-bande* simulation of a 15 Å GaN QW between AlN barrier of different widths. Left: conduction band and squared electron wavefunctions. Right: ISBT peak energy position E_{12} and figure of merit $\Pi\tau$.

For all but one sample (E1211), the PV is strongest around 150 K. This temperature dependence often occurs for PAMBE grown sample on AlN. A possible explanation is that due to photoionization of metastable defects in the AlN barriers and cap layer the conductivity varies with temperature. However transmission measurements taken in the Brewster angle configuration at different temperatures did not show any temperature dependent features (see figure B.1 in appendix B).

Comparison of measurements and simulations Figure 8.5 shows *calcul-bande* conduction band profile simulations for samples E1206, E1208, E1210, and E1211. Sample E1209 with the thinnest barriers of 7.5 Å is not discussed, since its thin AlN barriers allow the states to couple, leading to a higher tunneling probability and leakage currents and therefore to a lower device performance. The conduction band potential was obtained using (3.39), under the assumption that the active region is fully strained to the underlying AlN buffer. As expected, a thicker barrier leads to a stronger internal field F_{int} in the QW and to a weaker F_{int} in the barriers, resulting in a weaker confinement of the higher states. The more pronounced triangular shape of the QW potential lowers the QW's ground state. This also leads to a redshift of the QW interband transitions which is visible in the photoluminescence measurements presented in appendix D. Given the computed increase of the internal field in fully strained GaN QWs for increasing AlN barrier thickness, one would expect an analogous increase of the ISBT peak position energy, as seen in the right panel of figure 8.5. The measured peak position does indeed blue shift for increasing AlN barrier thickness; however with 7 meV between E1211 (30 Å barrier) and E1210 (70 Å barrier), and 2.5 meV between E1210 and E1208 (150 Å barrier), those shifts are weaker than the computed ones of 25 meV respectively 10 meV. This discrepancy may be explained by different growth parameters and a partial relaxation of MQW structures with lower overall AlN content.

The PV amplitude is proportional to the figure of merit $\Pi\tau$ (see also section 3.1.3), of which the computed values for this sample series are shown on the right panel of

figure 8.5. For barrier thicknesses above 30 Å, $\Pi\tau$ decreases due to the smaller displacement between the wavefunctions caused by the lowering of the left barrier which shifts the upper wavefunction to the left. For identical sample dimensions and doping density, only $\Pi\tau$ and the optical overlap C of the active region with the SWI needs to be taken into account. For the samples with 15 Å and 30 Å thick barriers, C is approximately 0.5; for samples with thicker barriers, C is close to 1, as the SWI's nodes and antinodes are averaged out. A multiplication of the factor $\Pi\tau$ with C would predict a signal increase of 21%, 90% and 15% for the samples with barriers widths of 30 Å , 70 Å and 150 Å as compared to the 15 Å barrier sample. Although this trend is visible in the experiment (see figure 8.4), it varies with temperature. This could be caused by the impedance mismatch between the current amplifier and the samples; the measured temperature dependence of the sample impedance differs between the individual samples of the series. This however cannot easily be modeled due to the complex current path between the two contacts evaporated on the sample cap. An adapted process consisting of an epitaxial lift-off would allow to contact the active region from the cap as well as from the buffer side. This would most likely result in a reduced device capacitance and parasitic resistances and hence in an increase in device performance as compared to the planar process.

Conclusion Both theory and experiment show that the PV signal strength depends on the barrier thicknesses. The reason for this is the dependence of $\Pi\,\tau$ on the internal field in the QWs, which again depends on the barrier thickness. For the investigated series with 15 Å thick GaN QWs and AlN barriers ranging from 15 Å to 150 Å, the PV is maximal for barrier thicknesses around 70 Å.

8.3 Different number of periods

In an ideal MQW structure, neglecting the conduction band bending at MQW and buffer/cap interfaces, all QWs are subject to the same internal electric field and strain; the illumination induced polarization P is identical in each QW. For a structure with N_{QW} QWs, the macroscopic photovoltage is thus proportional to $P \times N_{QW}$. To investigate this relation in the experiment a series of samples with 10 periods (E1133), 40 periods (E1131) and 100 periods (E1132) was grown. The QW and barrier thicknesses are 15 Å, the AlN buffer and cap layers are 1.1 µm respectively 50 nm thick.

Figure 8.6 shows the TM polarized transmission and the PV signal of all three samples. As expected, both the absorption and the PV amplitude get stronger with increasing number of periods. Due to the active region relaxation process becoming stronger for SLs containing more GaN, there is high energy tail in both PV and transmission forming for samples E1131 and E1132. A relaxation of the GaN QWs leads to a decrease of the internal fields and hence to an increase of the ISBT. This broadening is maximal for E1132 and minimal for E1133.

With identical sample structures and dimensions, the absorbance should increase linearly with the number of periods (factors 1, 4, 10 in comparison to the 10-period sample). However, the measured absorbance area is 2.7 times larger for the 40-period sample and 8.5 times larger for the 100 period sample, as seen in the right panel of figure 8.6. The increase of the integrated PV signal is even less linear: compared to the ten period sample,

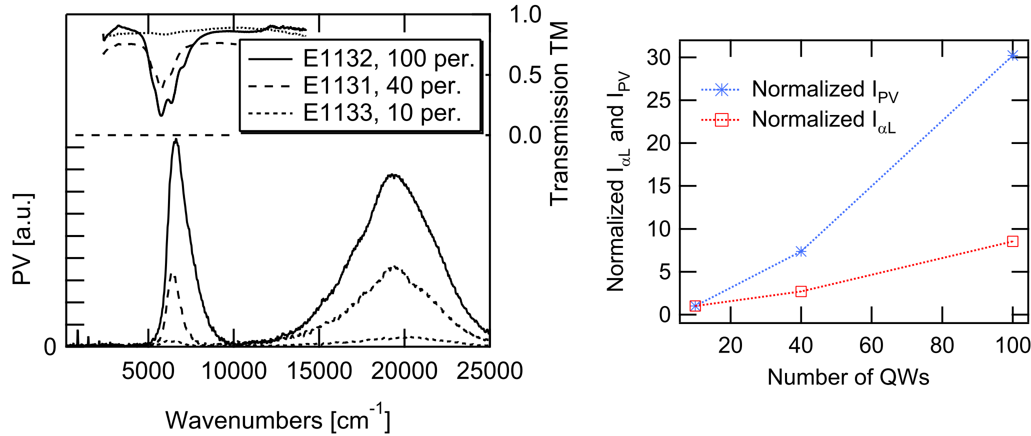

Figure 8.6: Left: TM transmission and PV of samples with 10 (E1133), 40 (E1131) and 100 (E1132) periods, measured at room temperature. Right: normalized integrated absorbance and PV as a function of number of periods.

the PV is 7.4 times stronger for the 40-period sample and 30 times stronger for the 100 period sample.

Periods	Ideal factor	Norm. I_α	Norm. I_{PV}
10 (E1133)	1	1	1
40 (E1131)	4	2.7	7.4
100 (E1132)	10	8.5	30

Table 8.2: Overview of integrated absorbances and PV signals. The measured integrated absorbance and PV spectra are normalized to the value obtained with the 10-period sample.

As the internal fields have an impact on the PV (see section 8.2), the explanation for this behavior is most probably found in the different field domains of the SL. There is an additional band bending at the interfaces to the cap and buffer layer, which depends on the choice of buffer and cap layer and hence internal fields. Here (AlN buffer and cap) the first few QWs (towards the buffer) are lifted up, whereas the top most QWs immerse in the 2DEG at the cap/SL interface. Those field variations will have a stronger impact on a few period sample than on one with 100 periods, which is consistent with the stronger deviation from PV$\propto N_{QW}$ between 10 and 40 periods (factor 1.85) compared to the one between 40 to 100 periods (factor 1.6). This indicates also that the PV signal mostly originates from the domain where the internal field is uniform in the sample.

Conclusion It was shown in theory and experiment that, as opposed to QWIPs and QCDs, not only the absorbance, but also the PV signal and hence the responsivity increases with the number of QW/barrier periods. This shows that for a detector based on photoinduced polarization, a high number of periods is crucial to obtain a strong PV signal.

8.4 Different GaN QW thickness

In this section a series of MBE samples grown at Cornell University, Ithaca, USA, is presented. Growth started with a 500 nm thick $Al_xGa_{1-x}N$ buffer (Si doped to $5\times10^{19}cm^{-3}$), whose Al content was determined with high-resolution X-ray diffraction. The active region consists of a regular SL of 20 periods with AlN barriers and doped GaN QWs, and is partly relaxed. The cap layer is 100 nm thick and has the same Al content as the buffer layer. Buffer and cap Al content, QW and barrier thickness, and QW doping density are listed in table 8.4. For the measurements, the samples were polished into 45° MPWs and two ohmic contact stripes (Ti/Al, 40/400 nm) were evaporated onto the cap layer.

Sample	Buffer / cap Al content	QW [Å]	Barrier [Å]	QW doping [cm^{-3}]
gs1709	90%	22	23	5×10^{19}
gs1752	98%	38	19	8×10^{19}
gs1758	100%	17	18	1×10^{20}

Table 8.3: Buffer/cap Al content, QW and barrier thicknesses and QW doping concentration of samples gs1709, gs1752 and gs1758 grown at Cornell University.

Measured spectral PV Figure 8.7 presents the ISB room temperature absorbance along with the PV measured at 10 K of gs1709, gs1752 and gs1758. For a broad PV spectrum such as obtained for gs1752, the influence of the FTIR blackbody spectral shape can not be neglected anymore, so all PV spectra were normalized with the blackbody spectrum of the FTIR internal NIR source.

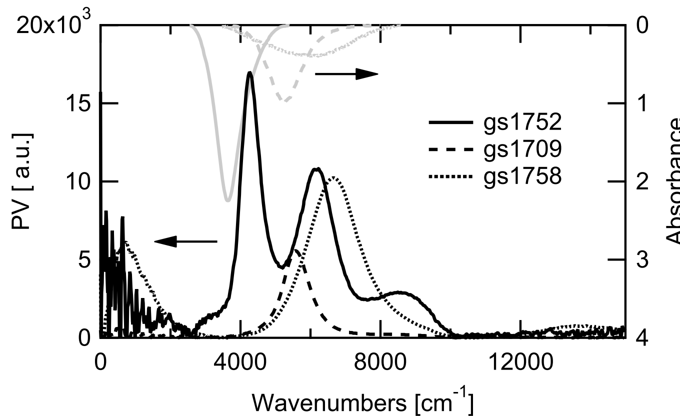

Figure 8.7: Room temperature absorbance (hanging from the top axis) and PV normalized with the blackbody of the FTIR internal NIR source (10 K) for samples gs1709 (22 Å QW), gs1752 (33 Å QW) and gs1758 (17 Å QW).

For the two samples with thinner QWs, the PV as well as the absorbance have one distinct peak; for gs1752 with a QW thickness of 38 Å the PV spectrum has three peaks,

but the absorbance has only one. The PV peaks can be assigned to the transitions from the first into the second, third and fourth state respectively in the wide QW. The decrease of the PV amplitude for higher final states f is less pronounced than the one of the absorbance. This is because the PV is proportional to the squared dipole matrix element μ_{1f}^2 (lower for higher final states f) and also to the displacement times the scattering time $|\langle\psi_f|z|\psi_f\rangle - \langle\psi_1|z|\psi_1\rangle| \times \tau_{1f}$ ($\Pi_{1f}\tau_{1f}$). E_{13} shows up as a small shoulder in the PV spectrum of gs1709. In the spectrum of gs1758, this transition is not visible anymore.

Based on the theory presented in section 3.2, the PV amplitude between the first and the second state should scale with the QW thickness; it should be maximal for gs1752 and minimal for gs1758. As seen in figure 8.7, the measurement does not quite follow this picture: gs1709 with a QW thickness of 22 Å has a lower PV than gs1758 with a QW thickness of 17 Å. This can be explained partly by the lower doping density of gs1709; also, the interface quality differs between the individual samples, possibly due to the different Al contents of cap and buffer layer.

Especially for samples gs1752 and gs1758, absorption and PV (not shown in the figure) did not disappear for TE polarized radiation. This deviation from the polarization selection rule also indicates a high interface roughness.

Influence of defects on the PV Unlike the PAMBE samples grown at CEA in Grenoble, the Cornell samples showed temperature dependent transient behavior during onset of illumination with the spectrometer NIR source. These effects are possibly related to persistent photoconductivity (PPC) and optical quenching (OQ). At low temperatures, electrons can be photoionized from deep defect levels in the bandgap into the conduction band. Once an electron is optically excited into the conduction band, the deep level undergoes a lattice relaxation, forming an energy barrier which hinders the excited electron to return to its original state; a PPC is created. OQ arises when valence band electrons are optically excited into mid-gap states. When such a defect has trapped a valence band electron, it relaxes and builds up an energy barrier, hindering the recombination of the trapped electron with a valence band hole; the thus created holes can now recombine with conduction band electrons. At higher temperatures (above 60 K–150 K) those defects are not metastable, and have no impact on the PV anymore.

Zeisel et al. [2000] has studied PPC in AlN, where the deep levels were assigned to Si. Ursaki et al. [2003] investigated PPC and OQ in GaN, and suggests that the deep defect involved in PPC is situated about 2 eV below the conduction band and the one involved in OQ about 1 eV above the valence band edge. They also found that the defect related to PPC undergoes a larger structural transformation after the excitation of an electron than the one related to OQ. Additionally they observed that OQ takes place on a faster time scale than PPC. Finally Li et al. [1998] concluded that in an $Al_xGa_{1-x}N/GaN$ heterostructure the electrons giving rise to PPC are photoionized from deep level impurities in the $Al_xGa_{1-x}N$ barrier band gap.

Figure 8.8 (left half) shows the PV of gs1758 at different temperatures as function of time. Time was measured from the onset of the illumination with the spectrometer's internal white light source. After each measurement, the sample was heated up to 313 K in order to maintain identical starting conditions. At temperatures below 100 K, the PV jumps abruptly to about half of its maximum value upon illumination, increases more slowly up to a maximum, and decreases with an even higher time constant again. Those

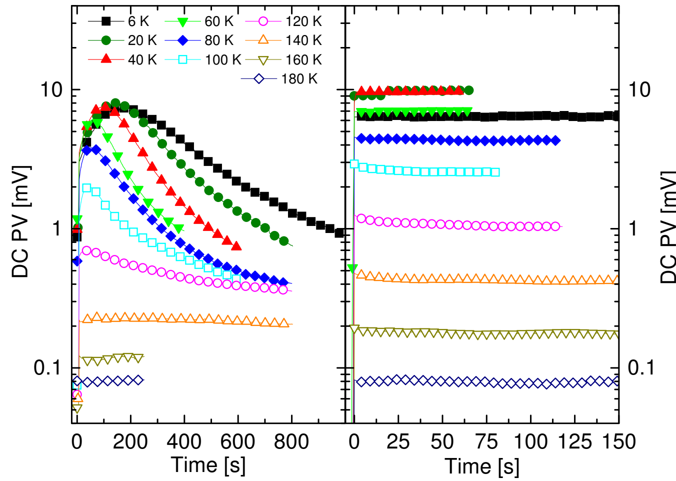

Figure 8.8: Left: transient PV of gs1758 for different temperatures while illuminating the sample with a halogen lamp. Right: idem with a silicon wafer used as optical filter. Sample illumination starts at t=0.

transients have the signature of two different time constants and disappear at temperatures above 120 K.

The same experiment was carried out a second time, while the impinging light was filtered with a Si wafer. Only light with energies up to 9091 cm^{-1} (1.127 eV) reached the sample, deep defects with energies greater than 1.127 eV were hence not activated. As seen in the right half of figure 8.8 the transient effects disappeared, which is an indication for metastable mid-gap state in the active region.

Conclusion The Cornell series shows that for thicker QWs higher lying states contribute to the PV signal. However, it is not possible to directly compare those MBE grown samples with the ones grown by PAMBE due to the different material quality. The latter manifests itself dramatically by PPC and OQ effects observed with the Cornell series.

8.5 Different $Al_{1-x}Ga_xN$ barriers

To obtain photoconductive QWIP operation, a bound to quasi-continuum transition from the first to the second electron state in the QW is required. To bring the second state of a reasonably thick GaN QW ($\geq$ 10 Å) close to the continuum, a ternary $Al_xGa_{1-x}N$ barrier is required. This section presents the PV spectra of samples with different Al contents in the barrier. As absorption measurements already showed in section 6.2, it is however not possible to bring the second state of a GaN QW in clear resonance with the continuum due to the saw tooth shape of the conduction band edge.

All samples consist of 40 periods and are grown on an 85 nm thick GaN contact layer deposited on an AlN/sapphire template. The barriers are 75 Å thick to exclude coupling between the ground states. The QWs are nominally 12.5 Å (5 ML) thick and are moderately doped (10^{19} cm^{-3}) in order to allow a potential drop over the active region if an external field is applied. The growth ended with a 75 Å $Al_xGa_{1-x}N$ barrier. No additional

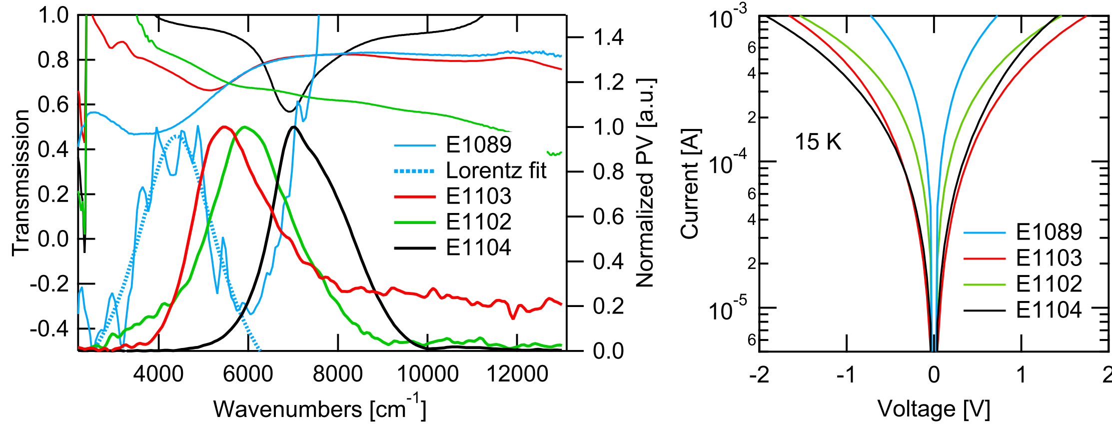

Figure 8.9: Left: TM transmission (300 K, hanging from the top axis) along with normalized PV spectra at 10 K, for samples with different $Al_{1-x}Ga_xN$ barriers. For sample E1089 a Lorentz fit spanning the ISB signal is also shown. The signals at higher energies are defect signals. Right: I-V measurements taken at 15 K.

cap layer was grown to allow for annealed ohmic top contacts which diffuse into the active region and reduce the band bending at the top of the active region. Table 8.5 lists the nominal Al content of the $Al_xGa_{1-x}N$ barriers for the investigated series.

Sample	E1089	E1102	E1103	E1104
Al content	60%	80%	70%	100%

Table 8.4: Nominal barrier Al content for samples with $Al_{1-x}Ga_xN$ barriers.

Stripe contacts In a first process, Ti/Au contact stripes were evaporated directly on the sample surface; the samples were then polished into 45° MPWs. The left panel of figure 8.9 shows the normalized PV response obtained at 15 K between two such contact stripes, along with the TM transmission presented in section 6.2. Sample E1102 has an inferior $Al_xGa_{1-x}N$ barrier material quality, leading to a grayish sample color and therefore no measurable absorption.

The PV signal of sample E1104 (AlN barrier) which has a clear bound-to-bound transition is the strongest. For E1103 (70% Al), the PV signal is five times lower, for E1102 (80% AlN, inferior material quality) it is eight times lower. For E1089 (60% AlN), the PV is dominated by defects and the ISBT signal is only a small shoulder; it has a broad absorption, indicating that the QW's second state is close to the continuum. For E1103 (70% AlN), defects are still visible in the PV spectrum but are weaker than the ISBT signal. For the two samples with higher AlN content in the barrier, the defect signal is not visible at 15 K. Lowering the Al content in the barrier introduces additional defect levels causing the high energy PV signal.

The I-V curves in the right panel of figure 8.9 show that a decreasing Al content leads to a lower resistivity, due to the lower barrier height and the increased barrier

material conductivity. Since the I-V curves were measured in the lateral stripe contact configuration, the resulting resistance is not only determined by vertical transport in the active region. As the barrier Al content is the only difference between the samples, the differences in the IV characteristics are due to the different barrier Al contents.

Except for E1102, which has an inferior material quality, the PV signal is stronger for samples with higher Al content in the barrier. A PV signal based on the dipoles formed during a photoinduced polarization process is smaller for a more conducting barrier which favors recombination of the dipole charges between the QWs. If the second states is close to the continuum, as for E1089, this effect is even stronger: the low barrier height further enhances the leakage current.

Mesa process This series was also processed in small mesa structures to measure a photoconductive signal. Mesa diameters of 6–12 µm were chosen to reduce the number of defect states in a single device. However, no PC signal could be measured across the available temperature range from 10 K up to room temperature.

Conclusion The PV signal is strongest for pure AlN barriers, where the resistance is maximal and the defect density minimal. However, no photoconductive signal was measured, as samples with their upper state close to resonance with the continuum had a low Al content in the barrier and therefore a high defect density and low resistance. This shows that photoinduced polarization is a robust and reliable detection mechanism for group III nitride ISB photodetectors.

8.6 Different cap thicknesses

In the previous sections, only the influence of parameters describing the active region such as number of periods, barrier and QW thicknesses, and barrier material have been discussed. Here, the influence of how the PV signal is measured at the surface is discussed. Figure 8.10 shows a possible equivalent circuit of a typical sample grown on an AlN buffer and capped with another AlN layer, with an illuminated signal contact and a dark reference contact. The active region is modeled by a capacitance C_a in parallel to a resistance R_a. While the region beneath one contact is illuminated, dipoles are forming, giving rise to a PV. Due to the insulating AlN buffer and cap layer the active regions under the contacts are capacitively coupled. This circuit is however only a draft and not sufficient to conduct meaningful simulations. In this section only the capacitance C_{cap} of the cap and therefore the capacitive coupling between the active region and the contact is investigated. For this purpose a series of samples with different AlN cap layer thicknesses listed in table 8.5 was grown; all samples have the same active region with 15 Å GaN QWs and 50 Å AlN barriers grown on a 1.1 µm thick AlN buffer.

Figure 8.11 shows the TM polarized room temperature transmission along with the PV obtained for samples having a 25 nm or thicker cap at 150 K. For the sample with a 7 nm cap, no PV was observed. The PV shoulder at 10000 cm^{-1} is due to the higher order E_{13} and the peak at 13000 cm^{-1} is a replica of the E_{12} ISBT, whereas the broad peak around 20000 cm^{-1} is a defect signal. In transmission, the E_{12} ISBT absorbance is in good agreement with the E_{12} PV peak. The integrated absorbance of sample E1301

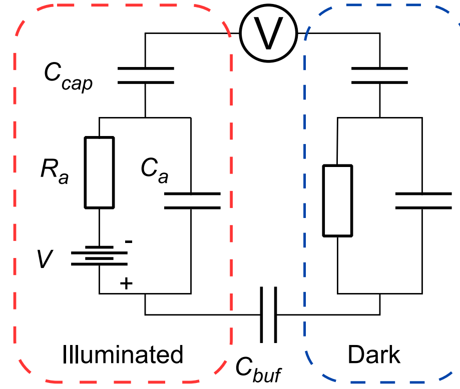

Figure 8.10: Equivalent circuit for an illuminated sample with AlN buffer and cap layers.

Sample	E1300	E1301	E1297	E1299
Cap [nm]	7	25	50	100
Integrated absorbance I_a [cm^{-1}]	740	2850	1130	997

Table 8.5: Nominal cap layer thickness and integrated absorbance of E1300, E1301, E1297 and E1299.

(25 nm cap) is 2.5 times larger than for the other samples (see table 8.5), indicating a higher doping density.

The signal measured at the contact is $V = q/C_{tot}$, where q is the photoinduced polarization electron charge and C_{tot} is the combined capacitance consisting of C_{buf}, C_a and the cap capacitance $C_{cap} = \epsilon_0 \epsilon_{AlN} A/t_{cap}$ with an area A and a cap thickness t_{cap}. For identical active region, ISBT energy, absorbance, cap material, and contact area A, the PV is proportional to $1/C_{cap} \propto t_{cap}$. The left panel of figure 8.12 shows the PV peak response as function of temperature for a 25 nm, 50 nm, and 100 nm AlN cap, the right panel shows the PV peak response as function of cap thickness at 150 K and 300 K. Given the higher absorbance of E1301, its PV peak value was divided by 2.5. For temperatures above 70 K, the expected increase of PV signal for thicker caps is observed. At lower temperatures, the PV peak response of the 25 nm cap sample E1301 is strongest. As already seen in section 8.2, the PV is strongest between 70 K and 150 K.

Conclusion In the device configuration with two contacts on an insulating cap layer, the capacitive coupling between active region and contact layer is a function of the cap layer thickness. It was shown that, as predicted by theory, the PV signal increases if the cap layer thickness is augmented.

8.7 PV response measured with a laser

To measure the frequency response of a sample, the setup described in section 5.3 is used. The measurement was done with sample E1065, as it fulfills the setup requirements: the sample does not need to be cooled down and is sensitive at 1.55 µm. E1065 was grown by PAMBE and its active region consists of a 40 period SL of GaN QWs and AlN barriers

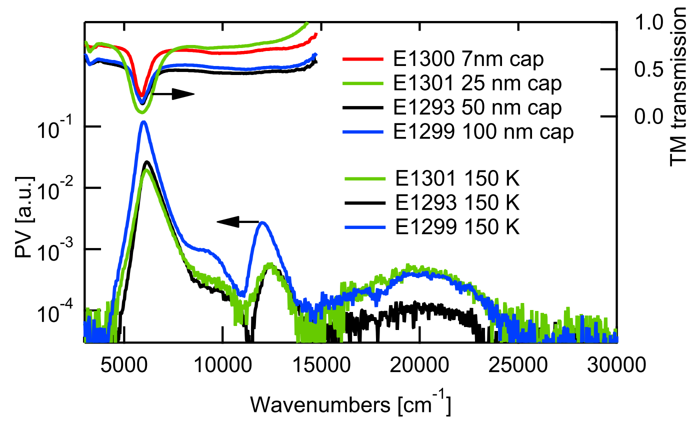

Figure 8.11: Spectra of linear TM transmission at 300 K and logarithmic PV at 150 K of samples with varying AlN cap thicknesses.

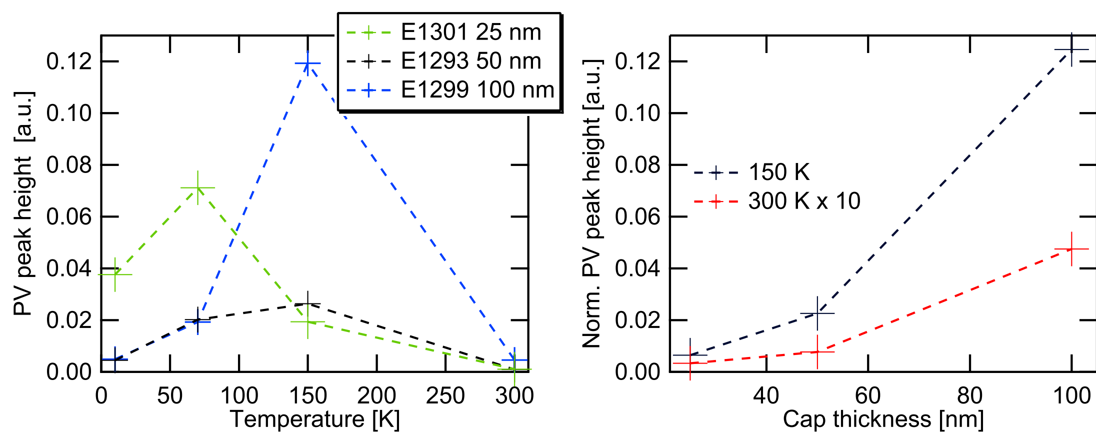

Figure 8.12: Left: PV peak response of E_{12} versus temperature. Right: PV peak response of E_{12} as function of cap thickness at 150 K and 300 K. The peak value of sample E1301 was normalized with a factor 2.5.

with a nominal thickness of 15 Å. The Si doping density in the QWs is 10^{20} cm^{-3}. This active region is sandwiched between a 1.1 μm thick AlN buffer and a 50 nm thick AlN cap. High resolution X-ray diffraction measurements of the SL confirmed a period of 3.1 nm (see appendix C); reciprocal space mapping showed an average relaxation of about 80%. Figure 8.13 shows the spectral PV obtained from a stripe contact along with the TE and TM transmission. The transmission is fully TM polarized, peaks at 6300 cm^{-1} (1.58 μm, 785 meV) and has a FWHM of 216 meV; the PV peaks at 6650 cm^{-1} (1.5 μm, 825 meV) and has a FWHM of 119 meV. Also, the room temperature PV signal is sufficiently large for frequency response measurements.

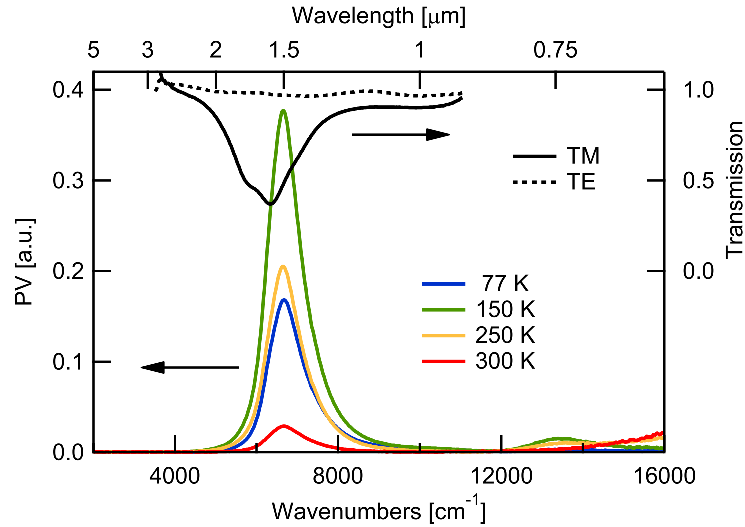

Figure 8.13: PV at different temperatures and room temperature transmission of E1065.

After evaporation and connection of additional mesa contacts (no etch process) the sample was mounted on a BNC connector and placed in the measurement setup as described in section 5.3. The left panel of figure 8.14 shows the normalized frequency response obtained for various signal (illuminated) and reference (dark) contacts. While illuminating the stripe contact using a (300 μm)^2 mesa as reference, no distinct corner frequency is observed and the response decreases over the whole investigated frequency range. When the (300 μm)^2 mesa is illuminated using the stripe as reference, the response is flat up to about 1 MHz. Illuminating the (300 μm)^2 mesa using a (200 μm)^2 mesa as reference results in an initial increase of the response towards higher frequencies up to about 10 MHz, followed by a decrease from 40 MHz on. Illuminating the (200 μm)^2 mesa using the (300 μm)^2 mesa as reference results in a similar response, except that the initial signal increase is not present in this case. For frequencies above 100 MHz, the measurement noise increases significantly; this is because of the lower gain of the amplifier used for frequencies above 100 MHz as well as the increased crosstalk at higher frequencies.

Given the complex shape of the frequency response and the complicated current path between two contacts evaporated on the sample cap, the measured data is not sufficient to extract an unambiguous equivalent circuit describing the frequency response.

When illuminating a mesa contact, the signal drops by roughly 20 dB per frequency decade above a certain corner frequency, despite the different low frequency responses. In

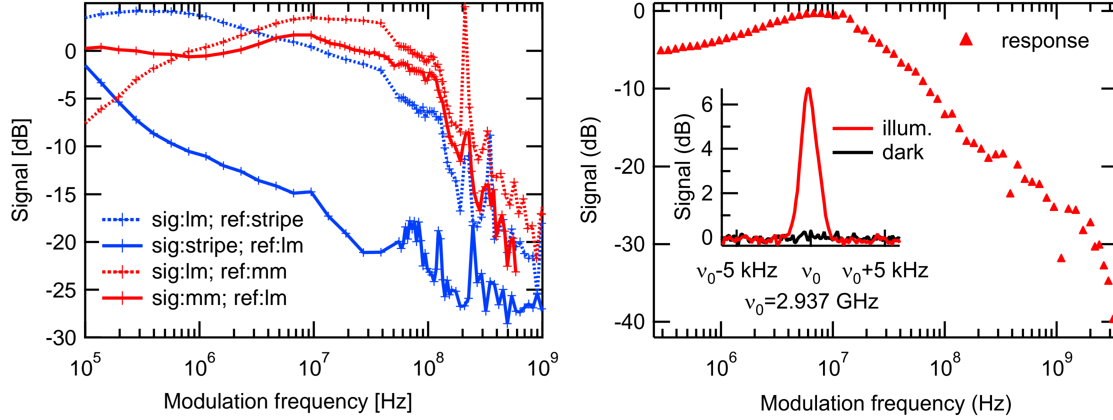

Figure 8.14: Frequency response of E1065. Left: various contacts (lm: $(300\,\mu\text{m})^2$, mm: $(200\,\mu\text{m})^2$, stripe: $(0.8\times 3)\,\text{mm}^2$). Right: detailed mm mesa spectrum measured with an external modulator; the inset shows the spectrum analyzer trace at 2.937 GHz.

figure 8.14 to the right the frequency response of a $(200\,\mu\text{m})^2$ signal mesa with a $(300\,\mu\text{m})^2$ mesa as reference taken with a long integration time is depicted; for this measurement, the laser diode was not modulated directly, but with an external electro-optical Mach-Zehnder modulator. Although the signal decreases for frequencies above 20 MHz, it was visible up to 3 GHz, which is the upper limit of the Agilent E4403B spectrum analyzer's measurement range. The FWHM of the signal is determined by the resolution of the spectrum analyzer.

Conclusion Illuminating a $(200\,\mu\text{m})^2$ mesa contact, a PV signal is seen up to frequencies of 3 GHz. The shape of the frequency response strongly depends on the contact configuration and size. For the larger stripe contact, the response is significantly weaker towards high frequencies due to its higher contact capacitance. Considering that the investigated samples where not at all optimized for high frequency operation and had a significant impedance mismatch towards the readout circuit, this is a promising result for high frequency photodetectors in the NIR based on ISB photoinduced polarization in group III nitride MQW structures.

8.7.1 Rectification voltage amplitude

In this section an estimation of the PV signal amplitude due to photoinduced polarization is presented based on the theory discussed in section 3.2.1.

In figure 8.15 the rectification voltage is plotted as function of intensity using

$$V_{rect} = \frac{2N_{QW}N_P t_{QW}}{\epsilon_{s,GaN} n_{GaN}} \chi^{(2)}_{0,max} Z_0 I \, \frac{\sin^2\Theta}{\cos\Theta} \tag{8.1}$$

$$\chi^{(2)}_{0,max} = \frac{e^3}{2\epsilon_0\hbar} n_{3D} \frac{\tau}{\Gamma} \mu_{12}^2 \delta_{12}, \tag{8.2}$$

where $N_P = 10$ is the number of passes, $N_{QW} = 40$ the number of QWs, $t_{QW} = 15\,\text{Å}$ the

QW thickness, $\Theta = 37°$, $\epsilon_{s,GaN} = 10.2$, the static dielectric function of GaN, $n_{GaN} = 2.33$ the refractive index of GaN, $n_{3D} = 10^{20}\,\mathrm{cm}^{-3}$ the 3D carrier density, $\tau = 370\,\mathrm{fs}$ the scattering time, $\Gamma = 40\,\mathrm{meV}$ the ISBT HWHM, $\mu_{12} = 3.5\,\mathrm{Å}$ the dipole matrix element and $\delta = 1.7\,\mathrm{Å}$ the displacement between the electron wavefunctions.

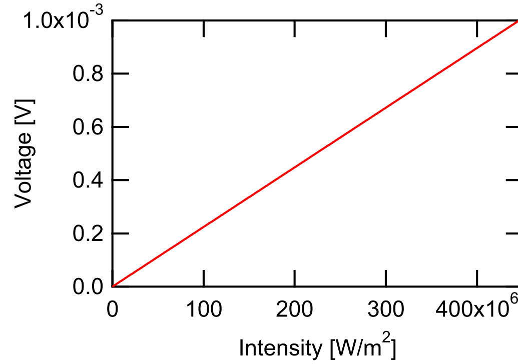

Figure 8.15: Computed rectification voltage as function of intensity.

An input intensity of $6\times10^7\,\mathrm{W/m^2}$ given by a 6 mW laser focused on a spot of $10\times10\,\mu\mathrm{m}^2$ results in a computed value of $135\,\mu\mathrm{V}$; experimentally, a room temperature voltage signal amplitude of about $10\,\mu\mathrm{V}$ was measured under laser illumination for E1065. As the maximal PV signal of E1065 at 150 K is 13 times stronger than at 300 K, the corresponding PV response under laser illumination illumination at 150 K is $130\,\mu\mathrm{V}$; this is in good agreement with the computed value of $135\,\mu\mathrm{V}$.

8.8 MOVPE samples

Besides the PAMBE grown samples discussed so far, samples grown by MOVPE at the EPF Lausanne aiming at short wavelength ISBT photodetection were characterized. For this, three different active regions were designed, as shown in figure 8.16.

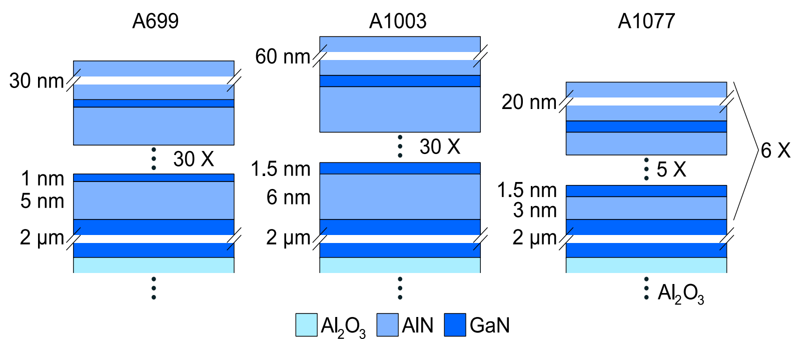

Figure 8.16: Structure of MOVPE samples A699, A1003 and A1007.

All samples are grown on a 2 µm thick GaN buffer, but the active region consists of different overall $\mathrm{Al}_x\mathrm{Ga}_{1-x}\mathrm{N}$ contents. A699 has a 30 period active region of 50 Å AlN barriers and 10 Å thick GaN QWs with an overall AlN content of 83%. For the similar

A1003, the active region consists of 60 Å AlN barriers and 15 Å thick GaN QW. A1077 has five periods of 30 Å AlN barrier and 15 Å GaN QW followed by a 20 nm AlN layer to keep the AlN content at an acceptably high value of 82%; this stack is then repeated six times. All three samples where processed into 45° MPW with contact stripes on the surface. A699 was additionally etched into a mesa structure with the bottom contact on the etched surface. For A1077 mesa contacts were evaporated on the cap without etching.

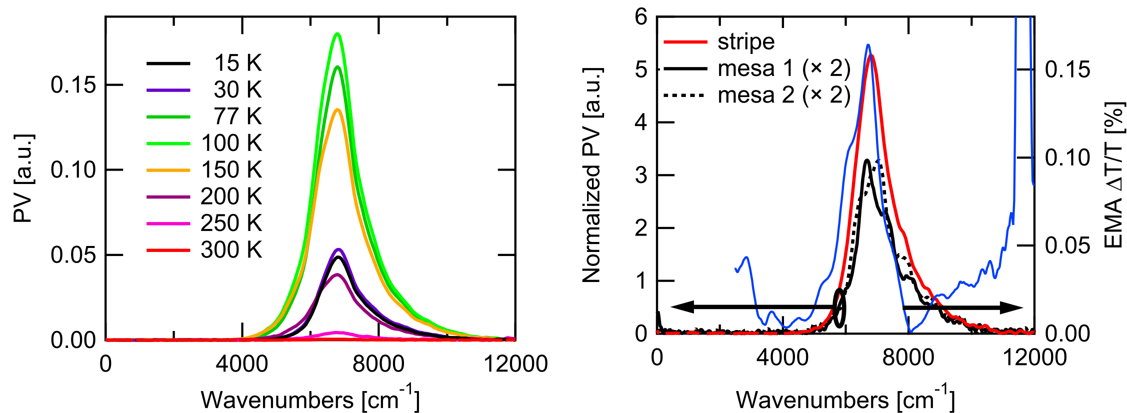

Figure 8.17: Left: PV response of A699 measured with the stripe process for different temperatures. Right: normalized PV response of A699 of the stripe process in comparison with the signal obtained with different mesas (at 15 K), along with the EMA (300 K) of the stripe process.

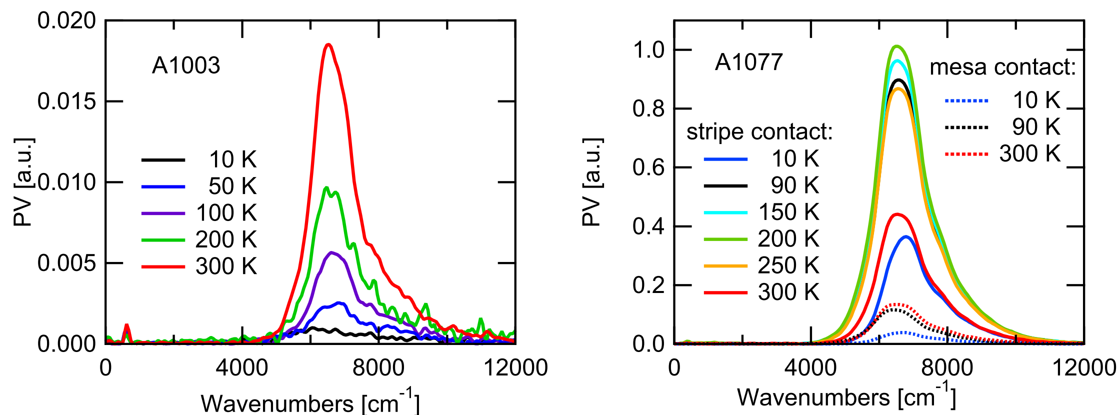

Figure 8.18: PV response for different temperatures. Left: stripe contact on A1003. Right: stripe and mesa contact on A1077.

PV spectra The spectral PV responses shown in this section are measured under identical conditions. The left panel of figure 8.17 shows the PV spectra of sample A699

using a stripe contact configuration. At 100 K, where the PV is strongest, the signal peaks at 6780 cm^{-1} and has a FWHM of 1400 cm^{-1}. The right panel shows again PV spectra of A699, but this time for two processed mesas. Mesa 2 is about 1 cm farther from the 2" wafer center than mesa 1; the differing spectral shapes of their PV indicate a spatial inhomogeneity of the wafer's layer thicknesses. For the larger stripe contact, those inhomogeneities are averaged out, resulting in a smoother, broader and more symmetric signal. Due to the shorter interaction length, the PV is weaker for the mesa process than for the stripe process. The electromodulated absorption of A699, also shown on the right panel, is in good agreement with the PV.

The left panel of figure 8.18 shows the PV of sample A1003 obtained with the stripe contact configuration. At 300 K, where the signal is strongest, the signal peaks at 6480 cm^{-1} and has a FWHM of 1360 cm^{-1}. The right panel shows the PV of sample A1077. The signal is maximal at 200 K, where it peaks at 6540 cm^{-1} and has a FWHM of 1600 cm^{-1}. For A1077, PV was measured for a stripe and for a mesa configuration (without etching); the spectra are identical, except that the signal is weaker for the smaller mesa contact.

Sample	A699	A1003	A1077
Peak E_{12}[cm^{-1}]	6780	6480	6540
FWHM [cm^{-1}]	1400	1360	1600

Table 8.6: Measured peak position and FWHM of MOVPE samples A699, A1003 and A1077.

Table 8.6 recapitulates the peak energies and the FWHMs of the three MOVPE samples. The relative spectral linewidth is about 22% for those samples, which is higher than for most PAMBE grown samples.

This is probably caused by the different strain relaxation for samples grown on GaN (as it is the case for the MOVPE samples presented in this section). High resolution X-ray measurements of sample A699 performed at the Fraunhofer IAF (shown in appendix C) showed a gradual relaxation of the MQW region. Although not investigated, this is most probably also the case for the other two MOVPE samples, as their overall AlN content in the active region is similar to A699.

Frequency response The MOVPE samples were mounted on a BNC adapter in order to investigate their frequency response using the setup described in section 5.3. Figure 8.19 shows the responses obtained for the stripe contact for sample A1003 and A1077 along with the response obtained for a mesa contact on the border of A1077. The weak signal of A1003 is nearly buried in the noise floor. A1077 has a strong signal for low modulation frequency and a slow roll-over for frequencies above 1 MHz, which can not be fitted by a first order low pass (see figure 8.19). This behavior which is not consistent with the responses obtained from E1065 (see figure 8.14) can be explained by the active region of A1077. There is an additional capacitive coupling between the five period MQW regions caused by the intermediate 20 nm thick AlN layer, which influences the frequency response.

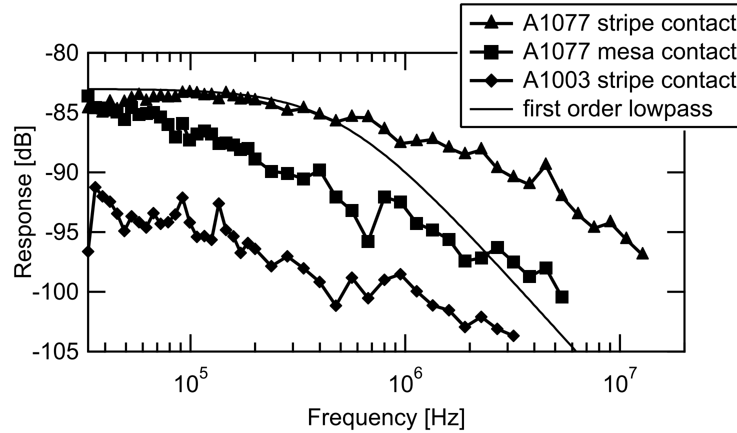

Figure 8.19: Frequency response obtained from a stripe contact of A1003 and of a stripe contact and mesa contact of A1077. The curved line depicts a first order low pass.

Conclusion PV signals around 6600 cm^{-1} (818 meV) were measured up to room temperature for MOVPE grown samples with a high overall Al content in the active region. For one sample (A1077), the frequency response at room temperature is flat up to 1 MHz and a signal is observed up to 15 MHz. Future work concentrates on the improvement of the frequency response by optimizing the growth conditions using an AlN buffer.

8.9 PV originating from higher levels

As seen in many PV spectra so far, there is sometimes an additional shoulder, or peak, or both at energies above the E_{12} ISBT energy. Samples grown on AlN having thicker AlN barriers, for example E1208 (150 Å), E1210 (70 Å) or samples E1293, E1299 and E1301 having all 50 Å thick barriers but different cap thicknesses show a distinct shoulder around 9500 cm^{-1} and an additional peak at twice the E_{12} ISBT energy. The shoulder has its origin in the E_{13} ISBT; it is most dominant in samples with thick barriers, because the figure of merit $\Pi\tau$ of the optical rectification for an E_{13} ISBT in a 15 Å QW is increasing with increasing barrier width: for thicker barriers, the displacement δ_{13} as well as the dipole matrix element μ_{13} and the scattering time τ_{31} are larger. The left panel of figure 8.20 shows the calculated values of $\Pi\tau$ and E_{13} of a 15 Å QW for different barrier thicknesses.

The right panel of figure 8.20 shows the normalized (with the blackbody of the internal spectrometer NIR source) PV spectrum of the sample E1299 at 150 K in a logarithmic scale. The exact energy of the E_{13} ISBT cannot be extracted unambiguously since the shoulder is nearly buried in the E_{12} signal slope.

The signal peak at twice the energy of E_{12} could be caused by the E_{14} ISBT. However, given the equal energies of E_{12} and E_{24}, also two photon absorption (TPA, see section 3.2.1) with a real (E_2) in-resonance mid-state may take place. Although this effect absorbs photons at the E_{12} ISBT energy, its nonlinear nature leads to additional signals at harmonics of E_{12} in the FTIR spectrum. Thus, the presence of a PV signal at 0 cm^{-1} further corroborates the assumption that TPA occurs.

A TPA absorption with a real resonant mid-state can not easily be measured since

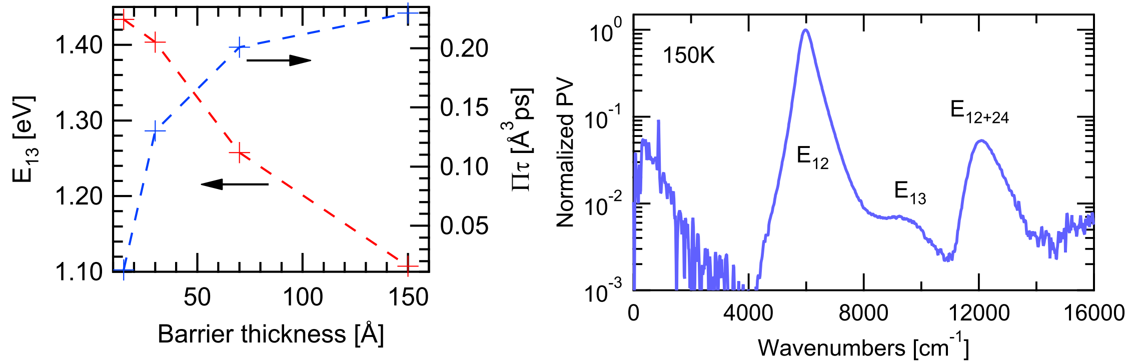

Figure 8.20: Left: computed (*calcul-bande*) $\Pi\tau$ and E_{13} of a 15 Å QW for different barrier thicknesses. Right: measured PV spectra at 150 K of E1299 with 50 Å AlN barriers and 15 Å GaN QWs.

the absorbed photons have the same energy ($E_{12} = E_{24}$) as the ones absorbed by the linear absorption E_{12}. Maier et al. [2004] measured photocurrent in a QWIP based on TPA. This special GaAs based QWIP has three equidistant levels, of which the third is in resonance with the continuum. At low bias voltages the QW can still be considered to be symmetric hence the linear E_{13} ISBT is forbidden; as electrons excited into the second state do not contribute to the photocurrent across the barriers due to their very small tunneling probability, the 3D QWIP photocurrent originates from electrons excited by a E_{12}, E_{23} TPA. In this low voltage regime, the photocurrent has a quadratic dependence on the illumination intensity. At higher bias voltages, the second state in the QW becomes resonant with the continuum, electrons excited to the second state tunnel through the low remaining barrier and contribute to the 3D photocurrent. Therefore, the high bias voltage regime photocurrent has a linear dependence on the intensity.

In the case of photoinduced polarization processes in AlN/GaN MQW structures such a separation of the two absorption processes and hence PV is not easy to achieve. Neither the PV signal coming from TPA nor from the linear absorption can be 'switched off' to investigate only one phenomenon. It is hence not straight forward to distinguish between a linear and a quadratic PV regime.

To separate fundamental (linear absorption) from the harmonic signal (TPA), the signal can be Fourier transformed as it is done by default in an FTIR. Assuming a monochromatic PV signal $F(\omega)$, its time domain counterpart $f(t)$ (corresponding to the Michelson interferogram measured by an FTIR spectrometer) can be written as

$$f(t) = (\alpha_{2D} I \sin(w_0 t) + c) \times (\beta I^2 \sin(w_0 t) + d), \tag{8.3}$$

where the first factor corresponds to a linear absorption with the absorption coefficient α_{2D}, the second factor to the quadratic TPA with the intensity independent absorption coefficient $\beta = \alpha_{2P}/I$, where α_{2P} describes the TPA process and is proportional to the intensity. A Fourier transformation of $f(t)$ results in a convolution of the two signals in

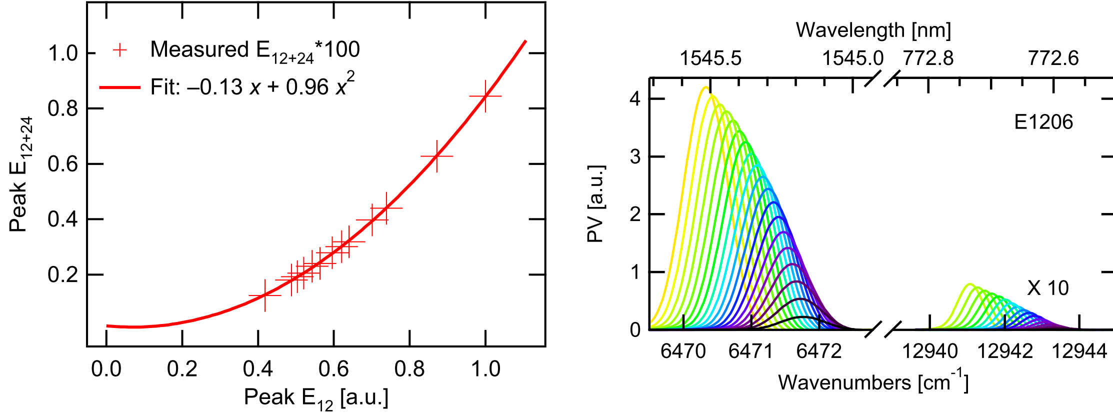

Figure 8.21: PV at E_{12} and $2 \times E_{12} = E_{14}$. Left: TPA PV peak at E_{12} and E_{24} as function of PV peak at E_{12} for sample E1208 under white light illumination. Right: PV spectrum for sample E1206 illuminated with a 1.55 µm DFB laser.

the frequency domain

$$F(\omega) = \frac{\pi}{i}\{\alpha_{2D} I[\delta(\omega - \omega_0) - \delta(\omega + \omega_0) + c] * \beta I^2[\delta(\omega - \omega_0) - \delta(\omega + \omega_0) + d]\}. \tag{8.4}$$

When calculating the convolution, the signal becomes:

$$\frac{i}{\pi} F(\omega) = 2\alpha_{2D}\, \beta + cd + (\alpha_{2D}\, d - \beta\, I\, c) \times I[\delta(\omega - \omega_0) - \delta(\omega + \omega_0)] - \alpha_{2D}\, \beta\, I^2\ [\delta(\omega - 2\omega_0) - \delta(\omega + 2\omega_0)] \tag{8.5}$$

For $\beta\, I = \alpha_{2P} \ll \alpha_{2D}$, the fundamental signal at ω_0 is proportional to I and the harmonic signal at $2\omega_0$ is proportional to I^2.

Comparing α_{2P} to α_{2D} leads to

$$\frac{\alpha_{2P}}{\alpha_{2D}} = \frac{I}{\hbar\omega} \frac{e^2 \omega_{23}}{\epsilon_0 c n} \mu_{23}^2 \frac{\tau_{12}}{\Gamma_{23}} \tag{8.6}$$

as was derived in chapter 3.2.1. For low intensities, $\alpha_{2D}/\alpha_{2P} = 100$-$1000$. The fundamental signal can hence indeed be assumed to be proportional to I and the harmonic signal to I^2.

In a first experiment the non-linear response of sample E1208 at 150 K under white light illumination (FTIR internal source) was investigated. To obtain various low input intensity levels, the NIR source was further attenuated using different metal grids. The left panel of figure 8.21 shows the peak value of the signal at the harmonic $2\omega_0 = E_{14}/\hbar$ as function of the peak value at the fundamental frequency $\omega_0 = E_{12}/\hbar$. The signal at E_{14} was multiplied by 100 in order to plot it on the same scale than the linear signal E_{12}. The quadratic dependence of the E_{14} signal is an indication that it is indeed caused by a nonlinear TPA process.

In a modified version of the above experiment, the FTIR white light source was replaced by a semiconductor laser operating at 1.55 µm (6470 cm^{-1}). For this experiment sample E1206 with barrier thicknesses of 15 Å AlN was used since E1208 (150 Å barrier) showed strong saturation effects while illuminated with the high laser intensity (20 mW focused on a 10 µm diameter spot). Figure 8.21 to the right shows the laser PV signal of E1206 for different laser drive currents. There is a PV signal at 6500 cm^{-1}, corresponding to the wavelength of the semiconductor laser, and an additional signal at its harmonic (13000 cm^{-1}, 775 nm), at which energy no 'real' light falls on the sample; the harmonic signal can thus not originate from a linear absorption process. The shift in the spectra are due to the warming of the laser caused by the increased drive current; the width of the peaks is given by the measurement resolution.

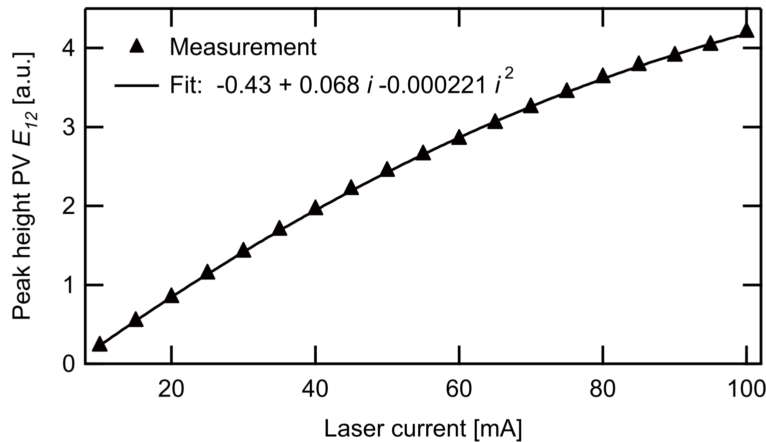

Figure 8.22: Fundamental peak energy as function of laser drive current along with a fit.

Figure 8.22 shows the peak value of the fundamental signal as a function of laser drive current. The fit shows a sublinear increase of the fundamental signal with increasing laser intensity. This is in agreement with the term $(\alpha_{2D}dI - \beta I^2c)$ of (8.5) assuming high intensities where βI^2c is not negligible anymore, and further corroborates that a TPA process takes place.

The attenuation of the fundamental signal increase can also be illustrated with two processes: assuming a two step absorption from E_1 through E_2 to E_4, electrons excited from the second state E_2 into the fourth state E_4 are missing in E_2, thus the E_{12} PV signal is attenuated. Furthermore, the photoinduced polarizations from the E_{12} and the E_{24} ISBT have opposite signs, wherefore the (stronger) E_{12} signal is attenuated by the E_{14} signal.

Conclusion In the spectral PV of samples having thicker barriers, different signals could be assigned to the E_{12} and the E_{13} ISBTs. In a 15 Å thick QW, there is a PV signal peak at twice the energy of E_{12} of the fundamental ISBT. This signal is an artifact caused by a nonlinear two photon absorption process into the fourth state E_4 via the resonant second state E_2 with $E_{12} = E_{24}$.

8.10 Photodetector design guidelines

Based on the previous section, the following guidelines for a detector based on photoinduced polarization at the fiber telecommunication wavelength of 1.5 µm can be given:

- For an AlN/GaN MQW structure, a GaN QW thickness of 15 Å results in a ISBT of 800 meV (section 6)
- For a thick MQW active region, a barrier thickness of 30 Å results in a maximal $\Pi\tau$ and thus a maximal PV signal (section 8.2)
- The PV signal strength is proportional to the number of QW/barrier periods in the active region (section 8.3)
- The PV signal strength is proportional to the doping density

Chapter 9

Conclusions

In this work, near infrared (NIR) intersubband transitions in GaN/AlN multi quantum wells (MQW) were investigated. The samples were grown by either plasma assisted molecular beam epitaxy (PAMBE) or metal-organic vapor-phase epitaxy (MOVPE). Strong and spectrally narrow intersubband absorption, light modulation, as well as fast photovoltage measurements confirmed that optoelectronic components in the fiber telecommunication wavelength range can be fabricated based on this material. Furthermore, our results indicate that both growth techniques are appropriate to achieve short wavelength ISBTs.

In contrast to most traditional applications of group III nitrides, the intrinsically asymmetric electron potential of GaN QWs, which is caused by strong internal piezo- and pyro-electric fields, could in this work be used to our advantage. The slight diagonality of ISBTs in group III nitride heterostructures gives rise to extremely interesting non-linear optical properties. As a first successful demonstration, we used this asymmetry for the design and the fabrication of photodetectors based on photoinduced polarization: due to the broken symmetry in a GaN QW, ISB photoexcited electrons form dipoles which lead to a measurable effect called optical rectification. In our sample geometry, optical rectification manifests itself as a photovoltage (PV), which can be detected up to room temperature. This is true for both PAMBE and MOVPE grown MQW structures. The size of the observed signals agrees well with theoretical predictions. In the course of the work, the influence of several device parameters on the photovoltage was investigated and design guidelines are presented.

More particularly, we achieved relative ISB absorption linewidths on the order of 11% for transition energies in the 800 meV (1.55 µm) range. To achieve such characteristics, a QW layer thickness of about 6 monolayers or 15 Å, along with an interfacial roughness below one monolayer is required. At 200 K, where photovoltage responses were maximal, a voltage of 130 μV could be achieved. In addition, we tested such a device under illumination with a modulated 1.55 µm laser diode and obtained a maximum frequency of 3 GHz at room temperature. Although our experiments did not involve a sophisticated reduction of parasitic effects, this result clearly demonstrates the high-speed capability of GaN-based intersubband devices. In future experiments, we therefore plan to further improve the device by acting on both the size of the produced signal (number of periods, doping) as well as on a reduction of the parasitics (cap and barrier layer thickness, epitaxial lift-off, RF strip-line contacts).

In a different line of research, we investigated the optical non-linearity of ISBTs in

GaN QWs in terms of two-photon absorption. Although the process involved in these experiments is an incoherent step-like process, it has a clear signature in the intensity dependent absorption coefficient. Since the spectral response of the photodetector was measured in a Fourier transform spectrometer, the non-linear absorption and detection process leads to a pronounced signal at twice the incoming photon energy. In addition, the signal at the fundamental frequency showed a large saturation effect which could be explained via a two-step absorption involving three resonant energy levels of the QW.

We finally demonstrated a prototype of an electro-optical modulator using a transistor like structure, whose $Al_xGa_{1-x}N$ barrier was replaced by a five period SL. Although the device was tested in multipass waveguide geometry, this modulator could strongly influence the transmission of light in a narrow band around 800 meV. To improve the modulation depth of this prototype, future work will concentrate on placing the modulator structure in a ridge waveguide.

Overall, this work contributed a substantial amount of work to reveal the fundamental working principles of optoelectronic ISBT structures in group III nitrides. The acquired know-how builds a base for future fast electro-optical devices in the NIR.

Acknowledgments

My gratitude goes to my thesis director Prof. Dr. Daniel Hofstetter for giving me the opportunity to do this work in his group. His patience with me, especially while revising my 'dry' manuscripts, his enthusiasm in research, and various discussions were a great support to me during the last four years.

I would like to express my gratitude to Fabrizio Giorgetta, my partner in life and at work. He processed several samples for me, assisted me during long measurements at night, critically corrected this work, and added wonderful figures.

My gratitude goes to Dr. Yargo Bonetti, who very carefully read the manuscript. He made us laugh with his fine sarcasm and kept me busy with crossword puzzles. Then I would also like to thank my former PhD colleague Dr. Marcel Graf for shared moments and discussions about physics and life in general.

I would like to thank Dr. Eva Monroy for her support; she was always there to answer my various questions, and for reading this thesis and acting as a co-examiner. I would also like to thank Prof. Dr. Hans Peter Herzig for being co-examiner of my jury.

Then I would like to thank Sylvain Nicolay for the good collaboration. My thanks goes to Dr. Sebastian Golka for good and fast collaboration; it was always helpful to have a second vegetarian around during the 'carnivorous' EU project meetings.

My thanks go also to the group of Prof. Dr. Jérôme Faist, for professional support but also for the various moments spent together having a beer or skiing. My thanks go also to Andreas Wittman, who assisted me during CV-measurement.

Thanks go also to Dr. Sven-Silvius Schad for helping with electro-modulated measurement in Ulm and for showing Fabrizio and me around Ulm.

Without the support from the electronics and mechanics workshop in building a lab and quickly (but not dirty!) creating some impossible measurement setups, this work would not have been possible.

Then I would also like to thank Roman Merz, Omar Manzardo, Iwan Märki and Xavier Niquille for lending me equipment and helping out with contact evaporation and S11 measurements. My thanks go also to Hansruedi Benedickter, who lend me several low noise amplifiers for frequency response measurements.

Finally I would like to thank my family including my grandmum Margrit Baumann for their support.

This work was supported by the European project NITWAVE (contract 004170) and the Swiss National Science Foundation.

Bibliography

a. URL `http://ece-www.colorado.edu/~bart/book/welcome.htm`.

b. URL `http://www.tydex.ru/materials/materials2/sapph_refr_ind.html`.

C. Adelmann, J. Brault, G. Mula, B. Daudin, L. Lymperakis, and J. Neugebauer. Gallium adsorption on (0001) GaN surfaces. *Phys. Rev. B*, 67(16):165419, 2003.

I. Akasaki, H. Amano, M. Kito, and K. Hiramatsu. Photoluminescence of Mg-doped p-type GaN and electroluminescence of GaN p-n-junction LED. *Journal of Luminescence*, 48(9):666–670, 1991.

H. Amano, M. Kito, K. Hiramatsu, and I. Akasaki. P-type conduction in Mg-doped GaN treated with low-energy electron-beam irradiation (LEEBI). *Jpn. J. Appl. Phys.*, 28 (12):L2112–L2114, 1989.

O. Ambacher. Growth and applications of group III-nitrides. *J. Phys. D: Appl. Phys*, 31: 2653–2710, 1998.

O. Ambacher, J. Smart, J. R. Shealy, N. G. Weimann, K. Chu, M. Murphy, W. J. Schaff, L. F. Eastman, R. Dimitrov, L. Wittmer, M. Stutzmann, W. Rieger, and J. Hilsenbeck. Two-dimensional electron gases induced by spontaneous and piezoelectric polarization charges in N- and Ga-face AlGaN/GaN heterostructures. *J. Appl. Phys.*, 85(6):3222–3233, 1999.

O. Ambacher, B. Foutz, J. Smart, J. R. Shealy, N. G. Weimann, K. Chu, M. Murphy, A. J. Sierakowski, W. J. Schaff, L. F. Eastman, R. Dimitrov, A. Mitchell, and M. Stutzmann. Two dimensional electron gases induced by spontaneous and piezoelectric polarization in undoped and doped AlGaN/GaN heterostructures. *J. Appl. Phys.*, 87(1):334–344, 2000.

O. Ambacher, J. Majewski, C. Miskys, A. Link, M. Hermann, M. Eickhoff, M. Stutzmann, F. Bernardini, V. Fiorentini, V. Tilak, B. Schaff, and L.F. Eastman. Pyroelectric properties of Al(In)GaN/GaN hetero- and quantum well structures. *J. Phys.: Condens. Matter*, 14:3399–3434, 2002.

A. F. M. Anwar, S. L. Wu, and R. T. Webster. Temperature dependent transport properties in GaN, $Al_xGa_{1-x}N$, and $In_xGa_{1-x}N$ semiconductors. *IEEE Transactions on Electron Devices*, 48(3):567–572, 2001.

T. Azuhata, T. Sota, K. Suzuki, and S. Nakamura. Polarized Raman-spectra in GaN. *J. Phys.: Condens. Matter*, 7(10):L129–L133, 1995.

G. Bastard. *Wave mechanics applied to semiconductor heterostructures.* Les éditions de physique, Les Ulis Cedex, 1988.

F. Bernardini and V. Fiorentini. Polarization fields in nitride nanostructures: 10 points to think about. *Appl. Surf. Sci.*, 166(1-4):23–29, 2000.

F. Bernardini and V. Fiorentini. Macroscopic polarization and band offsets at nitride heterojunctions. *Phys. Rev. B*, 57(16):R9427–R9430, 1998.

F. Bernardini, V. Fiorentini, and D. Vanderbilt. Spontaneous polarization and piezoelectric constants of III-V nitrides. *Phys. Rev. B*, 56(16):10024–10027, 1997.

R. W. Boyd. *Nonlinear optics.* Academic press, 2003.

D. Brunner, H. Angerer, E. Bustarret, F. Freudenberg, R. Hopler, R. Dimitrov, O. Ambacher, and M. Stutzmann. Optical constants of epitaxial AlGaN films and their temperature dependence. *J. Appl. Phys.*, 82(10):5090–5096, 1997.

C. Buchheim, R. Goldhahn, M. Rakel, C. Cobet, N. Esser, U. Rossow, D. Fuhrmann, and A. Hangleiter. Dielectric function and critical points of the band structure for AlGaN alloys. *Phys. Stat. Sol. (b)*, 242(13):2610–2616, 2005.

A. D. Bykhovski, B. L. Gelmont, and M. S. Shur. Current-voltage characteristics of strained piezoelectric structures. *J. Appl. Phys.*, 77(4):1616–1620, 1995.

A. D. Bykhovski, B. L. Gelmont, and M. S. Shur. Elastic strain relaxation and piezoeffect in GaN-AlN, GaN-AlGaN and GaN-InGaN superlattices. *J. Appl. Phys.*, 81(9):6332–6338, 1997.

F. Capasso, K. Mohammed, and A. Y. Cho. Resonant tunneling through double barriers, perpendicular quantum transport phenomena in superlattices, and their device applications. *IEEE J. Quantum Electron.*, 22(9):1853–1869, 1986.

N. E. Christensen and I. Gorczyca. Optical and structural properties of III-V nitrides under pressure. *Phys. Rev. B*, 50(7):4397–4415, 1994.

T. E. Cook, C. C. Fulton, W. J. Mecouch, R. F. Davis, G. Lucovsky, and R. J. Nemanich. Band offset measurements of the Si_3N_4/GaN (0001) interface. *J. Appl. Phys.*, 94(6): 3949–3954, 2003a.

T. E. Cook, C. C. Fulton, W. J. Mecouch, K. M. Tracy, R. F. Davis, E. H. Hurt, G. Lucovsky, and R. J. Nemanich. Measurement of the band offsets of SiO_2 on clean n- and p-type GaN(0001). *J. Appl. Phys.*, 93(7):3995–4004, 2003b.

R. Dingle, D. D. Sell, S. E. Stokowski, and M. Ilegems. Absorption, reflectance, and luminescence of GaN expitaxial layers. *Phys. Rev. B*, 4(4):1211, 1971.

R. Dingle, W. Wiegmann, and C. H. Henry. Quantum states of confined carriers in very thin $Al_xGa_{1-x}As$-GaAs-Al $_xGa_{1-x}As$ heterostructures. *Phys. Rev. Lett.*, 33(14):827–830, 1974.

L. Doyennette, L. Nevou, M. Tchernycheva, A. Lupu, F. Guillot, E. Monroy, R. Colombelli, and F.H. Julien. GaN-based quantum dot infrared photodetector operating at 1.38 μm. *Electron. Lett.*, 41(19):1077–1078, 2005.

E. Dupont, P. Corkum, H. C. Liu, P. H. Wilson, M. Buchanan, and Z. R. Wasilewski. 2-photon intersubband transitions in quantum-well infrared photoconductors. *Appl. Phys. Lett.*, 65(12):1560–1562, 1994.

S. Einfeldt, H. Heinke, V. Kirchner, and D. Hommel. Strain relaxation in AlGaN/GaN superlattices grown on GaN. *J. Appl. Phys.*, 89(4):2160–2167, 2001.

J. Faist, F. Capasso, C. Sirtori, D. L. Sivco, A. L. Hutchinson, S. N. G. Chu, and A. Y. Cho. Narrowing of the intersubband electroluminescent spectrum in coupled-quantum-well heterostructures. *Appl. Phys. Lett.*, 65(1):94–96, 1994a.

J. Faist, F. Capasso, D. L. Sivco, C. Sirtori, A. L. Hutchinson, and A. Y. Cho. Quantum cascade laser. *Science*, 264(5158):553–556, April 1994b.

V. Fiorentini, F. Bernardini, F. Della Sala, A. Di Carlo, and P. Lugli. Effects of macroscopic polarization in III-V nitride multiple quantum wells. *Phys. Rev. B*, 60(12):8849–8858, 1999.

Y. Gao, M. D. Craven, J. S. Speck, S. P. DenBaars, and E. L. Hu. Dislocation- and crystallographic-dependent photoelectrochemical wet etching of gallium nitride. *Appl. Phys. Lett.*, 84:3322, 2004.

N. Georgiev and T. Mozume. Photoluminescence study of InGaAs/AlAsSb heterostructure. *J. Appl. Phys.*, 89(2):1064–1069, 2001.

F. R. Giorgetta, E. Baumann, D. Hofstetter, C. Manz, Q. Yang, K. Köhler, and M. Graf. InGaAs/AlAsSb quantum cascade detectors operating in the near infrared. *Appl. Phys. Lett.*, 91:111115, 2007.

C. Gmachl, H. M. Ng, and A. Y. Cho. Intersubband absorption in GaN/AlGaN multiple quantum wells in the wavelength range of $\lambda \sim 1.75 - 4.2\mu$m. *Appl. Phys. Lett.*, 77(3): 334–336, 2000a.

C. Gmachl, H. M. Ng, S. N. G. Chu, and A. Y. Cho. Intersubband absorption at $\lambda \sim 1.55\mu$m in well- and modulation-doped GaN/AlGaN multiple quantum wells with superlattice barriers. *Appl. Phys. Lett.*, 77(23):3722–3724, 2000b.

C. Gmachl, H. M. Ng, and A. Y. Cho. Intersubband absorption in degenerately doped GaN/$Al_xGa_{1-x}N$ coupled double quantum wells. *Appl. Phys. Lett.*, 79(11):1590–1592, 2001.

N. Gogneau, D. Jalabert, E. Monroy, E. Sarigiannidou, J. L. Rouviere, T. Shibata, M. Tanaka, J. M. Gerard, and B. Daudin. Influence of AlN overgrowth on structural properties of GaN quantum wells and quantum dots grown by plasma-assisted molecular beam epitaxy. *J. Appl. Phys.*, 96(2):1104–1110, 2004.

S. Golka, C. Pflugl, W. Schrenk, G. Strasser, C. Skierbiszewski, M. Siekacz, I. Grzegory, and S. Porowski. Negative differential resistance in dislocation-free GaN/AlGaN double-barrier diodes grown on bulk GaN. *Appl. Phys. Lett.*, 88(17):172106, 2006.

W. Gotz, N. M. Johnson, H. Amano, and I. Akasaki. Deep level defects in n-type GaN. *Appl. Phys. Lett.*, 65(4):463–465, 1994.

W. Gotz, N. M. Johnson, M. D. Bremser, and R. F. Davis. A donorlike deep level defect in $Al_{0.12}Ga_{0.88}N$ characterized by capacitance transient spectroscopies. *Appl. Phys. Lett.*, 69(16):2379–2381, 1996a.

W. Gotz, N. M. Johnson, C. Chen, H. Liu, C. Kuo, and W. Imler. Activation energies of Si donors in GaN. *Appl. Phys. Lett.*, 68(22):3144–3146, 1996b.

M. Graf, N. Hoyler, M. Giovannini, J. Faist, and D. Hofstetter. InP-based quantum cascade detectors in the mid-infrared. *Appl. Phys. Lett.*, 88(24):241118, 2006.

J. Hamazaki, H. Kunugita, K. Ema, A. Kikuchi, and K. Kishino. Intersubband relaxation dynamics in GaN/AlN multiple quantum wells studied by two-color pump-probe experiments. *Phys. Rev. B*, 71(16):165334, 2005.

J. D. Heber, C. Gmachl, H. M. Ng, and A. Y. Cho. Comparative study of ultrafast intersubband electron scattering times at $\sim 1.55\,\mu$m wavelength in GaN/AlGaN heterostructures. *Appl. Phys. Lett.*, 81(7):1237–1239, 2002.

E. S. Hellman. The polarity of GaN: a critical review. *Mrs. Internet J. Nitride Semicond. Res.*, 3:11, 1998.

M. Helm. *The basic physics of intersubband transitions*, volume 62 of *Semiconductors and semimetals*. Academic press, London, UK, 2000.

A. Helman, M. Tchernycheva, A. Lusson, E. Warde, F. H. Julien, K. Moumanis, G. Fishman, E. Monroy, B. Daudin, D. L. Dang, E. Bellet-Amalric, and D. Jalabert. Intersubband spectroscopy of doped and undoped GaN/AlN quantum wells grown by molecular-beam epitaxy. *Appl. Phys. Lett.*, 83(25):5196–5198, 2003.

M. Hermann, E. Monroy, A. Helman, B. Baur, M. Albrecht, B. Daudin, O. Ambacher, M. Stutzmann, and M. Eickhoff. Vertical transport in group III-nitride heterostructures and application in AlN/GaN resonant tunneling diodes. *Phys. Stat. Sol. (c)*, 1(8):2210–2227, 2004.

D. Hofstetter, L. Diehl, J. Faist, W. J. Schaff, J. Hwang, L. F. Eastman, and C. Zellweger. Midinfrared intersubband absorption on AlGaN/GaN-based high-electron-mobility transistors. *Appl. Phys. Lett.*, 80(16):2991–2993, 2002.

D. Hofstetter, S.-S. Schad, H. Wu, W. J. Schaff, and L. F. Eastman. GaN/AlN-based quantum-well infrared photodetector for 1.55 μm. *Appl. Phys. Lett.*, 83(3):572–574, 2003.

R. Hui, S. Taherion, Y. Wan, J. Li, S. X. Jin, J. Y. Lin, and H. X. Jiang. GaN-based waveguide devices for long-wavelength optical communications. *Appl. Phys. Lett.*, 82 (9):1326–1328, 2003a.

R. Hui, Y. Wan, J. Li, S. X. Jin, J. Y. Lin, and H. X. Jiang. Birefringence of GaN/AlGaN optical waveguides. *Appl. Phys. Lett.*, 83(9):1698–1700, 2003b.

N. Iizuka, K. Kaneko, and N. Suzuki. Ultrafast intersubband relaxation ($\leq$ 150 fs) in AlGaN/GaN multiple quantum wells. *Appl. Phys. Lett.*, 77(5):648–650, 2000.

N. Iizuka, K. Kaneko, and N. Suzuki. Near-infrared intersubband absorption in GaN/AlN quantum wells grown by molecular beam epitaxy. *Appl. Phys. Lett.*, 81(10):1803–1805, 2002.

S. C. Jain, M. Willander, J. Narayan, and R. Van Overstraeten. III-nitrides: growth, characterization, and properties. *J. Appl. Phys.*, 87(3):965–1006, 2000.

W. C. Johnson, J. B. Parsons, and M. C. Crew. Nitrogen compounds of gallium III gallic nitride. *Journal of Physical Chemistry*, 36(7):2651–2654, 1932.

M. A. Khan, A. Bhattarai, J. N. Kuznia, and D. T. Olson. High-electron-mobility transistor based on a GaN-$Al_xGa_{1-x}N$ heterojunction. *Appl. Phys. Lett.*, 63(9):1214–1215, 1993a.

M. A. Khan, J. N. Kuznia, A. R. Bhattarai, and D. T. Olson. Metal-semiconductor field-effect transistor based on single-crystal GaN. *Appl. Phys. Lett.*, 62(15):1786–1787, 1993b.

J. B. Khurgin and S. Li. 2-photon absorption and nonresonant nonlinear index of refraction in the intersubband transitions in the quantum-wells. *Appl. Phys. Lett.*, 62(2):126–128, 1993.

A. Kikuchi, R. Bannai, and K. Kishino. AlN/GaN double-barrier resonant tunneling diodes grown by rf-plasma-assisted molecular-beam epitaxy. *Appl. Phys. Lett.*, 81(9): 1729–1731, 2002.

K. Kishino, A. Kikuchi, H. Kanazawa, and T. Tachibana. Intersubband transition in $(GaN)_m/(AlN)_n$ superlattices in the wavelength range from 1.08 to 1.61 μm. *Appl. Phys. Lett.*, 81(7):1234–1236, 2002.

C. Kittel. *Introduction to Solid State Physics*. John Wiley & Sons, 1996.

P. Lefebvre, B. Gil, J. Allegre, H. Mathieu, N. Grandjean, M. Leroux, J. Massies, and P. Bigenwald. Quantum-confined Stark effect and recombination dynamics of spatially indirect excitons in MBE-grown GaN-AlGaN quantum wells. *Mrs. Internet J. Nitride Semicond. Res.*, 4:G3.69, 1999.

B. F. Levine, K. K. Choi, C. G. Bethea, J. Walker, and R. J. Malik. Quantum well avalanche multiplication initiated by 10μm intersubband absorption and photoexcited tunneling. *Appl. Phys. Lett.*, 51(12):934–936, 1987.

M. E. Levinshtein, S. L. Rumyantsev, and M. S. Shur, editors. *Properties of advanced semiconductor materials: GaN, AlN, InN, BN, SiC, SiGe.* John Wiley and Sons, 2001.

J. Z. Li, J. Y. Lin, H. X. Jiang, and M. A. Khan. Effects of persistent photoconductivity on the characteristic performance of an AlGaN/GaN heterostructure ultraviolet detector. *Appl. Phys. Lett.*, 72(22):2868–2870, 1998.

A. S. Liu, S. L. Chuang, and C. Z. Ning. Piezoelectric field-enhanced second-order nonlinear optical susceptibilities in wurtzite GaN/AlGaN quantum wells. *Appl. Phys. Lett.*, 76(3):333–335, 2000.

H. C. Liu. Dependence of absorption-spectrum and responsivity on the upper state position in quantum-well intersubband photodetectors. *J. Appl. Phys.*, 73(6):3062–3067, 1993.

H. C. Liu. *Quantum well infrared photodetector physics and novel devices*, volume 62 of *Semiconductors and semimetals.* Academic press, London, UK, 2000.

H. C. Liu, E. Dupont, and M. Ershov. Nonlinear quantum well infrared photodetector. *Journal of Nonlinear Optical Physics & Materials*, 11(4):433–443, 2002.

T. Maier, H. Schneider, M. Walther, P. Koidl, and H. C. Liu. Resonant two-photon photoemission in quantum-well infrared photodetectors. *Appl. Phys. Lett.*, 84(25):5162–5164, 2004.

T. Maier, H. Schneider, H. C. Liu, M. Walther, and P. Koidl. Quantum-well infrared photodetector with voltage-switchable quadratic and linear response. *Appl. Phys. Lett.*, 88(5):051117, 2006.

H. P. Maruska and J. J. Tietjen. Preparation and properties of vapor-deposited single-crystalline GaN. *Appl. Phys. Lett.*, 15(10):327, 1969.

T. Mattila and A. Zunger. Predicted bond length variation in wurtzite and zinc-blende InGaN and AlGaN alloys. *J. Appl. Phys.*, 85(1):160–167, 1999.

S. N. Mohammad. Contact mechanisms and design principles for Schottky contacts to group-III nitrides. *J. Appl. Phys.*, 97(6):063703, 2005.

S. N. Mohammad. Contact mechanisms and design principles for nonalloyed ohmic contacts to n-GaN. *J. Appl. Phys.*, 95(9):4856–4865, 2004.

B. Monemar. Fundamental energy-gap of GaN from photoluminescence excitation-spectra. *Phys. Rev. B*, 10(2):676–681, 1974.

W. J. Moore, J. A. Freitas, R. T. Holm, O. Kovalenkov, and V. Dmitriev. Infrared dielectric function of wurtzite Aluminum Nitride. *Appl. Phys. Lett.*, 86(14):141912, 2005.

E. Munoz, E. Monroy, J. L. Pau, F. Calle, F. Omnes, and P. Gibart. III nitrides and UV detection. *J. Phys.: Condens. Matter*, 13(32):7115–7137, 2001.

S. Nakamura, T. Mukai, and M. Senoh. Candela-class high-brightness InGaN/AlGaN double-heterostructure blue-light-emitting diodes. *Appl. Phys. Lett.*, 64(13):1687–1689, 1994.

S. Nakamura, N. Senoh, N. Iwasa, and S. I. Nagahama. High-brightness InGaN blue, green and yellow light-emitting-diodes with quantum-well structures. *Jpn. J. Appl. Phys.*, 34 (7A):L797–L799, 1995.

S. Nakamura, M. Senoh, S. Nagahama, N. Iwasa, T. Yamada, T. Matsushita, H. Kiyoku, and Y. Sugimoto. InGaN-based multi-quantum-well-structure laser diodes. *Jpn. J. Appl. Phys.*, 35(1B):L74–L76, 1996.

T. Nakamura, S. Mochizuki, S. Terao, T. Sano, M. Iwaya, S. Kamiyama, H. Amano, and I. Akasaki. Structural analysis of Si-doped AlGaN/GaN multi-quantum wells. *J. Cryst. Growth*, 237:1129–1132, 2002.

L. Nevou, M. Tchernycheva, F. H. Julien, F. Guillot, and E. Monroy. Short wavelength ($\lambda = 2.13\,\mu$m) intersubband luminescence from GaN/AlN quantum wells at room temperature. *Appl. Phys. Lett.*, 90(12):121106, 2007.

S. Nicolay, E. Feltin, J. F. Carlin, M. Mosca, L. Nevou, M. Tchernycheva, F. H. Julien, M. Ilegems, and N. Grandjean. Indium surfactant effect on AlN/GaN heterostructures grown by metal-organic vapor-phase epitaxy: applications to intersubband transitions. *Appl. Phys. Lett.*, 88(15):151902, 2006.

S. Nicolay, E. Feltin, J.-F. Carlin, N. Grandjean, L. Nevou, F. H. Julien, M. Schmidbauer, T. Remmele, and M. Albrecht. Strain-induced interface instability in GaN/AlN multiple quantum wells. *Appl. Phys. Lett.*, 91:061927, 2007. To be published.

J. F. Nye. *Physical properties of crystals their representation by tensors and matrices.* Oxford: Clarendon, 1976.

J. I. Pankove, E. A. Miller, and J. E. Berkeyhe. GaN electroluminescent diodes. *RCA Review*, 32(3):383, 1971a.

J. I. Pankove, E. A. Miller, D. Richman, and J. E. Berkeyheiser. Electroluminescence in GaN. *Journal of Luminescence*, 4:63, 1971b.

S. J. Pearton, J. C. Zolper, R. J. Shul, and F. Ren. GaN: processing, defects, and devices. *J. Appl. Phys.*, 86(1):1–78, 1999.

P. B. Perry and R. F. Rutz. Optical-absorption edge of single-crystal AlN prepared by a close-spaced vapor process. *Appl. Phys. Lett.*, 33(4):319–321, 1978.

J. Radovanovic, V. Milanovic, Z. Ikonic, and D. Indjin. Quantum well shape optimization of continuously graded $\mathrm{Al_xGa_{1-x}N}$ structures by combined supersymmetric and coordinate transform methods. *Phys. Rev. B*, 69(11):115311, 2004.

R. Rapaport, Gang Chen, O. Mitrofanov, C. Gmachl, H. M. Ng, and S. N. G. Chu. Resonant optical nonlinearities from intersubband transitions in GaN/AlN quantum wells. *Appl. Phys. Lett.*, 83(2):263–265, 2003.

M. A. Reshchikov and H. Morkoc. Luminescence properties of defects in GaN. *J. Appl. Phys.*, 97(6):061301, 2005.

E. Rosencher and P. Bois. Model system for optical nonlinearities – asymmetric quantum-wells. *Phys. Rev. B*, 44(20):11315–11327, 1991.

E. Rosencher and B. Vinter. *Optoélectronique*. Masson, 1998.

E. Rosencher, P. Bois, J. Nagle, E. Costard, and S. Delaitre. Observation of nonlinear optical rectification at 10.6 μm in compositionally asymmetrical AlGaAs multiquantum wells. *Appl. Phys. Lett.*, 55(16):1597–1599, 1989.

E. Rosencher, P. Bois, B. Vinter, J. Nagle, and D. Kaplan. Giant nonlinear optical rectification at 8–12 μm in asymmetric coupled quantum-wells. *Appl. Phys. Lett.*, 56 (19):1822–1824, 1990.

J. L. Rouviere, M. Arlery, B. Daudin, G. Feuillet, and O. Briot. Transmission electron microscopy structural characterisation of GaN layers grown on (0001) sapphire. *Materials Science and Engineering B*, 50(1-3):61–71, 1997.

E. Sarigiannidou, E. Monroy, N. Gogneau, G. Radtke, P. Bayle-Guillemaud, E. Bellet-Amalric, B. Daudin, and J. L. Rouviere. Comparison of the structural quality in Ga-face and N-face polarity GaN/AlN multiple-quantum-well structures. *Semicond. Sci. Technol.*, 21(5):612–618, 2006.

H. Schneider, T. Maier, H. C. Liu, M. Walther, and P. Koidl. Ultrasensitive femtosecond two-photon detector with resonantly enhanced nonlinear absorption. *Optics Letters*, 30 (3):287–289, 2005.

H. Schneider, T. Maier, H.C. Liu, and M. Walther. Investigation of electron dephasing and intersubband relaxation in quantum wells via two-photon photocurrents. *Phys. Rev. B*, 2007. Submitted.

F. Schwabl. *Quantenmechanik*. Springer, 1998.

M. Seelmann-Eggebert, J. L. Weyher, H. Obloh, H. Zimmermann, A. Rar, and S. Porowski. Polarity of 001 GaN epilayers grown on a 001 sapphire. *Appl. Phys. Lett.*, 71:2635–2637, 1997.

M. P. Semtsiv, M. Wienold, S. Dressler, and W. T. Masselink. Short-wavelength ($\lambda \approx 3.05\,\mu$m) InP-based strain-compensated quantum-cascade laser. *Appl. Phys. Lett.*, 90 (5):051111, 2007.

S. Shokhovets, R. Goldhahn, G. Gobsch, S. Piekh, R. Lantier, A. Rizzi, V. Lebedev, and W. Richter. Determination of the anisotropic dielectric function for wurtzite AlN and GaN by spectroscopic ellipsometry. *J. Appl. Phys.*, 94(1):307–312, 2003.

C. Sirtori, F. Capasso, J. Faist, and S. Scandolo. Nonparabolicity and a sum-rule associated with bound-to-bound and bound-to-continuum intersubband transitions in quantum-wells. *Phys. Rev. B*, 50(12):8663–8674, 1994.

F. Stern and S. Das Sarma. Electron-energy levels in GaAs-$Ga_{1-x}Al_xAs$ heterojunctions. *Phys. Rev. B*, 30(2):840–848, 1984.

S. Strite and H. Morkoç. GaN, AlN, and InN: A Review. *Journal of Vacuum Science and Technology B*, 10(4):1237–1266, 1992.

M. Sumiya, T. Ohnishi, M. Tanaka, A. Ohtomo, M. Kawasaki, M. Yoshimoto, H. Koinuma, K. Ohtsuka, and S. Fuke. Control of the polarity and surface morphology of GaN films deposited on c-plane sapphire. *Mrs. Internet J. Nitride Semicond. Res.*, 6:23, 1999.

M. Suzuki, T. Uenoyama, and A. Yanase. First-principles calculations of effective-mass parameters of AlN and GaN. *Phys. Rev. B*, 52(11):8132–8139, 1995.

N. Suzuki and N. Iizuka. Feasibility study on ultrafast nonlinear optical properties of 1.55-μm intersubband transition in AlGaN/GaN quantum wells. *Jpn. J. Appl. Phys.*, 36(8A):L1006–L1008, 1997.

S. M. Sze. *Physics of semiconductor devices.* John Wiley & Sons, 2nd edition, 1981.

M. Tchernycheva, L. Nevou, L. Doyennette, F. H. Julien, E. Warde, F. Guillot, E. Monroy, E. Bellet-Amalric, T. Remmele, and M. Albrecht. Systematic experimental and theoretical investigation of intersubband absorption in GaN/AlN quantum wells. *Phys. Rev. B*, 73(12):125347, 2006.

E. Tiede, M. Thimann, and K. Sensse. Ueber phosphorecenzfaehiges, durch Silicium aktiviertes Aluminiumnitrid. *Chemische Berichte*, 61:1568, 1928.

V. V. Ursaki, I. M. Tiginyanu, P. C. Ricci, A. Anedda, S. Hubbard, and P. Pavlidis. Persistent photoconductivity and optical quenching of photocurrent in GaN layers under dual excitation. *J. Appl. Phys.*, 94(6):3875–3882, 2003.

C. G. Van de Walle and J. Neugebauer. First-principles calculations for defects and impurities: applications to III-nitrides. *J. Appl. Phys.*, 95(8):3851–3879, 2004.

I. Vurgaftman and J. R. Meyer. Band parameters for nitrogen-containing semiconductors. *J. Appl. Phys.*, 94(6):3675–3696, 2003.

I. Vurgaftman, J. R. Meyer, and L. R. Ram-Mohan. Band parameters for III–V compound semiconductors and their alloys. *J. Appl. Phys.*, 89(11):5815–5875, 2001.

J. M. Wagner and F. Bechstedt. Properties of strained wurtzite GaN and AlN: ab initio studies. *Phys. Rev. B*, 66(11):115202, 2002.

Z. Wang, K. Reimann, M. Woerner, T. Elsaesser, D. Hofstetter, E. Baumann, F. R. Giorgetta, H. Wu, W. J. Schaff, and L. F. Eastman. Ultrafast hole burning in intersubband absorption lines of GaN/AlN superlattices. *Appl. Phys. Lett.*, 89(15):151103, 2006.

L. C. West and S. J. Eglash. 1st observation of an extremely large-dipole infrared transition within the conduction-band of a GaAs quantum well. *Appl. Phys. Lett.*, 46(12):1156–1158, 1985.

W. L. Wolfe and G. J. Zissis, editors. *The inrared handbook*. Environmental Research Institute of Michigan, 2nd edition, 1985.

C. I. Wu, A. Kahn, E. S. Hellman, and D. N. E. Buchanan. Electron affinity at aluminum nitride surfaces. *Appl. Phys. Lett.*, 73(10):1346–1348, 1998.

J. Wu, W. Walukiewicz, W. Shan, K. M. Yu, J. W. Ager, S. X. Li, E. E. Haller, H. Lu, and W. J. Schaff. Temperature dependence of the fundamental band gap of InN. *J. Appl. Phys.*, 94(7):4457–4460, 2003.

W. M. Yim, E. J. Stofko, P. J. Zanzucch, J. I. Pankove, M. Ettenber, and S. L. Gilbert. Epitaxially grown AlN and its optical band gap. *J. Appl. Phys.*, 44(1):292–296, 1973.

S. Yoshida, S. Misawa, and S. Gonda. Improvements on the electrical and luminescent properties of reactive molecular-beam epitaxially grown GaN films by using AlN-coated sapphire substrates. *Appl. Phys. Lett.*, 42(5):427–429, 1983.

A. Yoshikawa and K. Xu. Polarity selection process and polarity manipulation of GaN in MOVPE and RF-MBE growth. *Thin Solid Films*, 412(1-2):38–43, June 2002.

G. Yu, G. Wang, H. Ishikawa, M. Umeno, T. Soga, T. Egawa, J. Watanabe, and T. Jimbo. Optical properties of wurtzite structure GaN on sapphire around fundamental absorption edge (0.78-4.77 eV) by spectroscopic ellipsometry and the optical transmission method. *Appl. Phys. Lett.*, 70(24):3209–3211, 1997.

A. Zavriyev, E. Dupont, P. B. Corkum, H. C. Liu, and Z. Biglov. Direct autocorrelation measurements of midinfrared picosecond pulses by quantum-well devices. *Optics Letters*, 20(18):1886–1888, 1995.

R. Zeisel, M. W. Bayerl, S. T. B. Goennenwein, R. Dimitrov, O. Ambacher, M. S. Brandt, and M. Stutzmann. DX-behavior of Si in AlN. *Phys. Rev. B*, 61:R16283–R16286, 2000.

S. B. Zhang. The microscopic origin of the doping limits in semiconductors and wide-gap materials and recent developments in overcoming these limits: a review. *J. Phys.: Condens. Matter*, 14:R881–R903, 2002.

I. S. Zheludev. *Physics of Crystalline Dielectrics Volume 1 Crystallography and Spontaneous Polarization*. Plenum press, New York, 1971.

Publication List

E. Baumann, F. R. Giorgetta, D. Hofstetter, F. Guillot, S. Leconte, E. Bellet-Amalric, and E. Monroy. GaN/AlN electro-optical modulator prototype at telecommunication wavelengths. *Phys. Stat. Sol. (c)*, 4:1621–1624, 2007.

F. R. Giorgetta, E. Baumann, M. Graf, L. Ajili, N. Hoyler, M. Giovannini, J. Faist, D. Hofstetter, P. Krötz, and G. Sonnabend. 16.5 μm quantum cascade detector using miniband transport. *Appl. Phys. Lett.*, 90(23):231111, 2007a.

F. R. Giorgetta, E. Baumann, D. Hofstetter, S. Leconte, F. Guillot, E. Bellet-Amalric, and E. Monroy. High frequency (f=2.37 GHz) room temperature operation of 1.55 μm AlN/GaN-based intersubband detector. *Electron. Lett.*, 43:185–186, 2007b.

F. R. Giorgetta, E. Baumann, D. Hofstetter, C. Manz, Q. Yang, K. Köhler, and M. Graf. InGaAs/AlAsSb quantum cascade detectors operating in the near infrared. *Appl. Phys. Lett.*, 91:111115, 2007c.

D. Hofstetter, E. Baumann, F. R. Giorgetta, F. Guillot, S. Leconte, and E. Monroy. Optically non-linear effects in intersubband transitions of GaN/AlN-based superlattice structures. *Appl. Phys. Lett.*, 91, 2007a.

D. Hofstetter, L. Despont, M. G. Garnier, E. Baumann, F.R. Giorgetta, P. Aebi, L. Kirste, H. Lu, and W. J. Schaff. Structural investigations of epitaxial InN by x-ray photoelectron diffraction and x-ray diffraction. *Appl. Phys. Lett.*, 90(19):191912, 2007b.

E. Baumann, F. R. Giorgetta, D. Hofstetter, S. Golka, W. Schrenk, G. Strasser, L. Kirste, S. Nicolay, E. Feltin, J. F. Carlin, and N. Grandjean. Near infrared absorption and room temperature photovoltaic response in AlN/GaN superlattices grown by metal-organic vapor-phase epitaxy. *Appl. Phys. Lett.*, 89(4):041106, 2006a.

E. Baumann, F. R. Giorgetta, D. Hofstetter, S. Leconte, F. Guillot, E. Bellet-Amalric, and E. Monroy. Electrically adjustable intersubband absorption of a GaN/AlN superlattice grown on a transistorlike structure. *Appl. Phys. Lett.*, 89(10):101121, 2006b.

E. A. DeCuir, Jr., E. Fred, O. Manasreh, J. Xie, H. Morkoc, E. Baumann, and D. Hofstetter. 1.37 - 2.90 micron intersubband transitions in GaN/AlN superlattices. In C.R. Abernathy, H. Jiang, and J. M. Zavada, editors, *Advances in III-V Nitride Semiconductor Materials and Devices*, volume 955E of *Mater. Res. Soc. Symp. Proc.*, pages 0955–I13–01, Warrendale, PA, 2006.

D. Hofstetter, E. Baumann, F. R. Giorgetta, M. Graf, M. Maier, F. Guillot, E. Bellet-Amalric, and E. Monroy. High-quality AlN/GaN-superlattice structures for the fabrication of narrow-band 1.4 μm photovoltaic intersubband detectors. *Appl. Phys. Lett.*, 88(12):121112, 2006.

E. Monroy, F. Guillot, S. Leconte, E. Bellet-Amalric, E. Baumann, F. R. Giorgetta, D. Hofstetter, L. Nevou, M. Tchernycheva, L. Doyennette, F. H. Julien, T. Remmele, and M. Albrecht. MBE growth of nitride-based photovoltaic intersubband detectors. *Superlattices Microstruct.*, 40(4-6):418–425, 2006a.

E. Monroy, F. Guillot, S. Leconte, E. Bellet-Amalric, L. Nevou, L. Doyennette, M. Tchernycheva, F. H. Julien, E. Baumann, F. R. Giorgetta, D. Hofstetter, and L. S. Dang. III-nitride nanostructures for infrared optoelectronics. *Acta Physica Polonica A*, 110 (3):295–301, 2006b.

Z. Wang, K. Reimann, M. Woerner, T. Elsaesser, D. Hofstetter, E. Baumann, F. R. Giorgetta, H. Wu, W. J. Schaff, and L. F. Eastman. Ultrafast hole burning in intersubband absorption lines of GaN/AlN superlattices. *Appl. Phys. Lett.*, 89(15):151103, 2006.

E. Baumann, F. R. Giorgetta, D. Hofstetter, L. Kirste, H. Wu, W. J. Schaff, and L. F. Eastman. Intersubband absorption in AlN/GaN-superlattice structures. *Phys. Stat. Sol. (c)*, 2(3):1014–1018, 2005a.

E. Baumann, F. R. Giorgetta, D. Hofstetter, H. Lu, X. Chen, W. J. Schaff, L. F. Eastman, S. Golka, W. Schrenk, and G. Strasser. Intersubband photoconductivity at 1.6 μm using a strain-compensated AlN/GaN superlattice. *Appl. Phys. Lett.*, 87(19):191102, 2005b.

E. Baumann, F. R. Giorgetta, D. Hofstetter, H. Wu, W. J. Schaff, L. F. Eastman, and L. Kirste. Tunneling effects and intersubband absorption in AlN/GaN superlattices. *Appl. Phys. Lett.*, 86(3):032110, 2005c.

Appendix A

Band Alignment and Metal Work Function

Metal-semiconductor contacts exhibit a certain electrical resistance. In the absence of any surface states and surface Fermi level pinning, the band structure at the metal-semiconductor interface aligns in a way that the Fermi level of the metal and the semiconductor are aligned. Depending on the work functions of both materials, this leads to a band bending of the semiconductor. This bending is described by

$$q\Phi_{SM} = q\Phi_M - \chi_S \tag{A.1}$$

where Φ_{SM} is the barrier height for a metal n-semiconductor interface, Φ_M the metal work function and χ_S the electron affinity of the semiconductor.

Metal	Φ_M [V]	Φ_{GaN-M} [V]
Ga	3.96	–
Al	4.28	0.17
Ti	4.33	0.17
Ni	5.15	1.04
Au	5.1	0.99

Table A.1: Metal work function and Schottky barrier height for a metal n-GaN interface taken from Mohammad [2004].

Table A lists the work function and barrier heights of metals normally used for electrical contacts on n-GaN.

The conduction band offset between n-GaN and and the insulators SiO_2 ($\chi = 1.1\,\mathrm{eV}$) and Si_3N_4 ($\chi = 1.8\,\mathrm{eV}$) was deduced to be 3.6 eV [Cook et al., 2003b] and 2.4 eV respectively [Cook et al., 2003a].

Appendix B

Brewster Angle Transmission

Sample E1208 (presented in table 8.2) with a MQW active region consisting of 15 Å GaN QW and 15 Å AlN barrier was measured in the Brewster angle configuration for different temperatures. Figure B.1 shows the obtained transmission spectra.

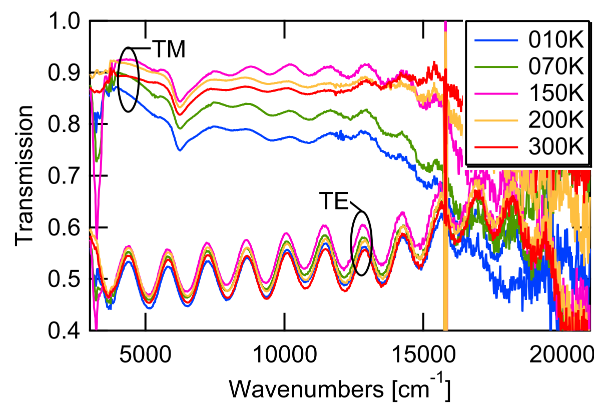

Figure B.1: Transmission in the Brewster angle configuration as a function of temperature for sample E1208.

Appendix C

X-ray

This appendix shows X-ray measurements of:

- Sample E1065 performed at CEA Grenoble; the sample is described in table 6.1.
- Sample A699 performed at IAF Freiburg; the sample is described in section 8.7.

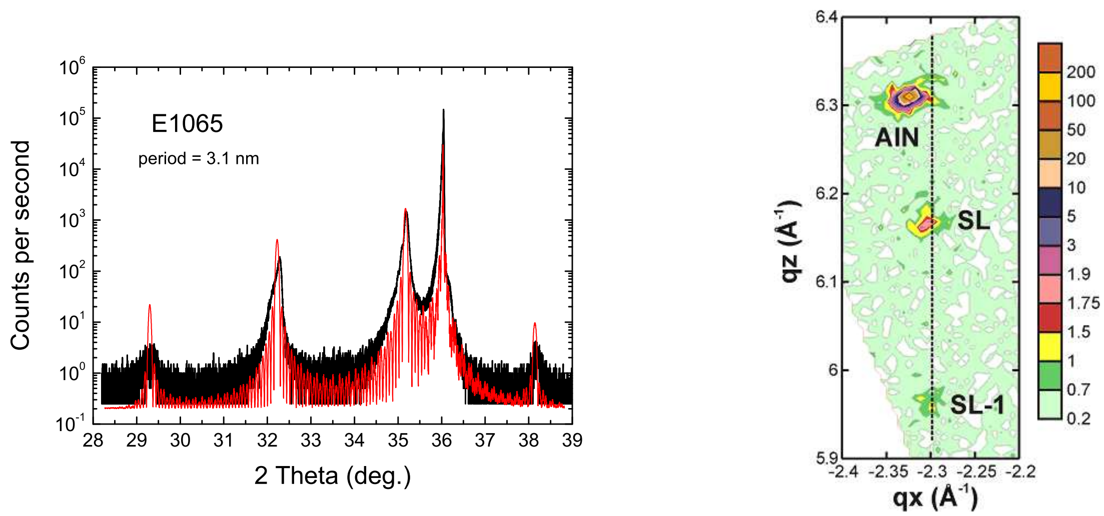

Figure C.1: Sample E1065. Left: X-ray measurement and fit. Right: reciprocal space mapping.

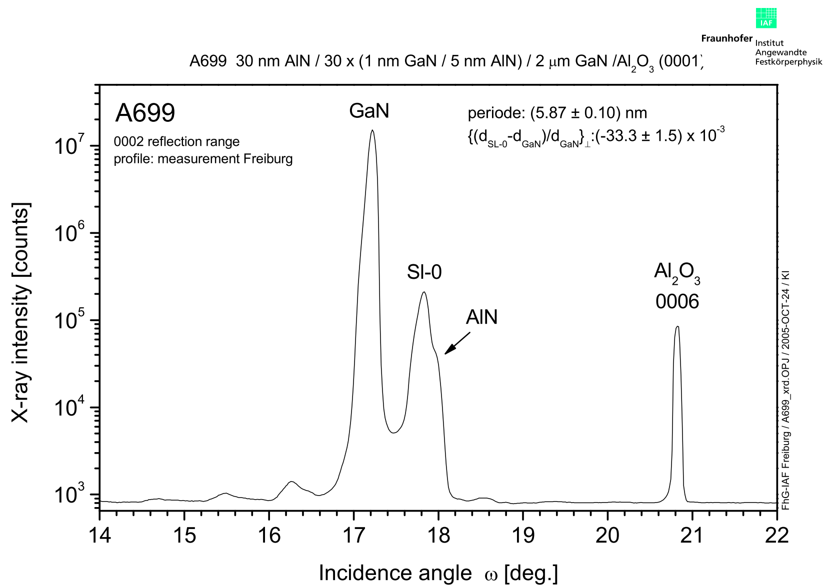

Figure C.2: X-ray measurement of sample A699.

Appendix D

PL Measurement

This appendix shows photoluminescence measurements of:

- The sample series with different number of periods presented in section 8.3.
- The sample series with different barrier thicknesses presented in section 8.2.
- The sample series with different well thicknesses presented in section 8.4.
- The sample series with different cap thicknesses presented in section 8.6.

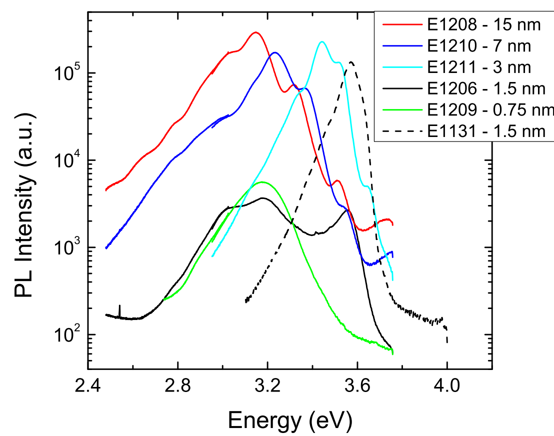

Figure D.1: Photoluminescence of sample series with different barrier thicknesses.

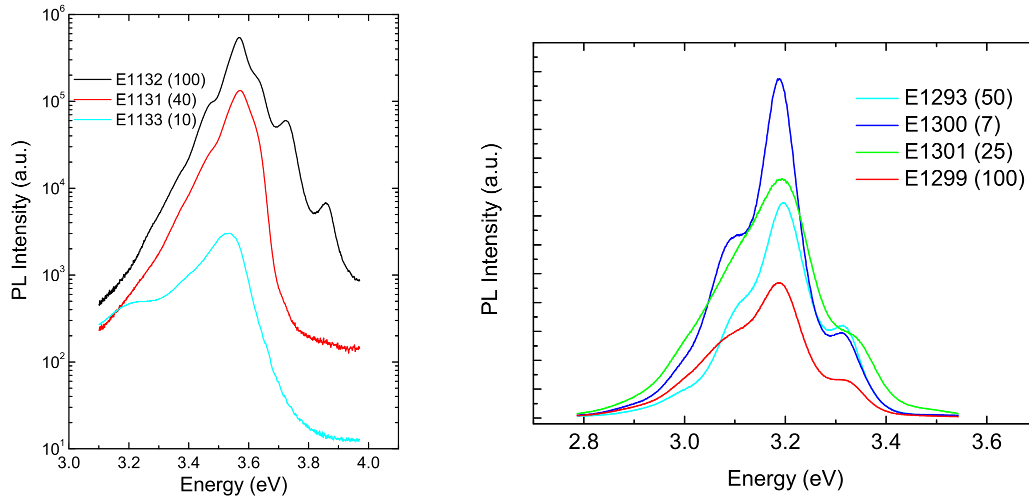

Figure D.2: Photoluminescence of sample series with different number of periods (left panel) respectively different cap thicknesses (right panel).

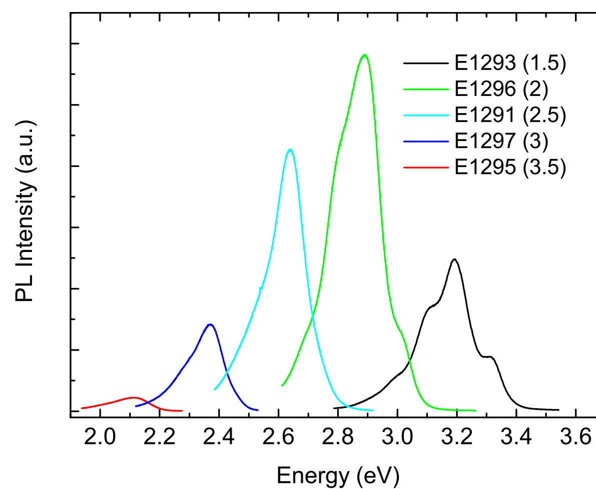

Figure D.3: Photoluminescence of sample series with different well thicknesses [nm].

Appendix E

CV Measurement

This appendix presents the capacitance-voltage (CV) measurements of sample E888 and E889 presented in table 7.1. The sample surface was contacted with KOH and no surface etching was performed. The CV measurements of sample E889, which has a 2 nm cap and a 6 nm GaN/AlN active region grown on GaN shows a carrier density peak at 8 nm corresponding to the 2DEG at the interface between the active region and the GaN bottom contact layer. The carrier density of sample E888, which has a 2 nm cap and a 30 nm GaN/AlN active region grown on a GaN contact layer, has no distinct features and lies around $1.2\times10^{19}\,\mathrm{cm}^{-3}$ corresponding to the QW doping of $1\times10^{19}\,\mathrm{cm}^{-3}$; as the resolution of the CV measurement is lower than the QW thickness of 1.5 nm, the measurement is basically a flat line.

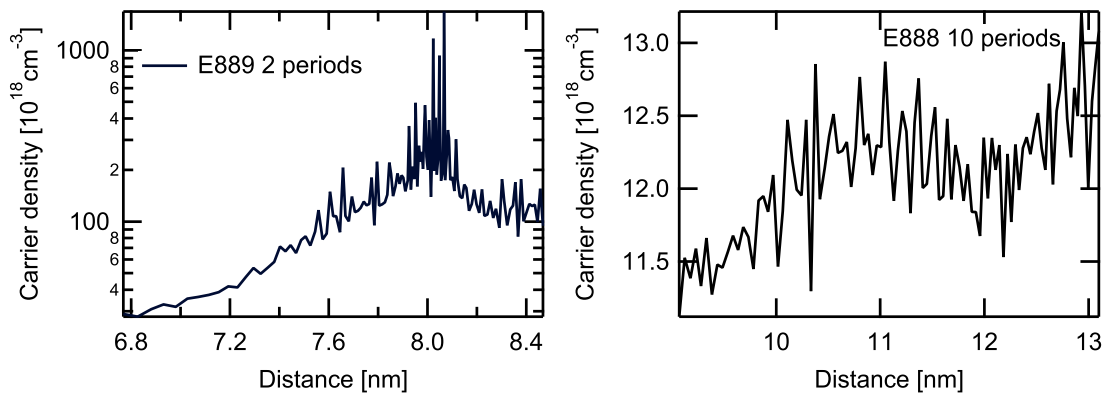

Figure E.1: CV measurement of samples E889 (left) and E888 (right).

Appendix F

Resonant Tunneling Diode Design

In figure F.1 the conduction band structure *cband* simulation of a resonant tunneling diode (RTD) is shown. In order to reduce the influence of the internal fields, the injector and collector are not made of GaN, but of a regular SL. There is a miniband forming in both the injector and the collector which is broken in the middle by a thinner QW. Under the application of an external bias, the injector and extractor miniband are brought in and out of resonance with the ground state of the thinner QW, and the electrons are tunneling through the 'first' barrier into the ground state of the thinner QW. Such a structure (E926)

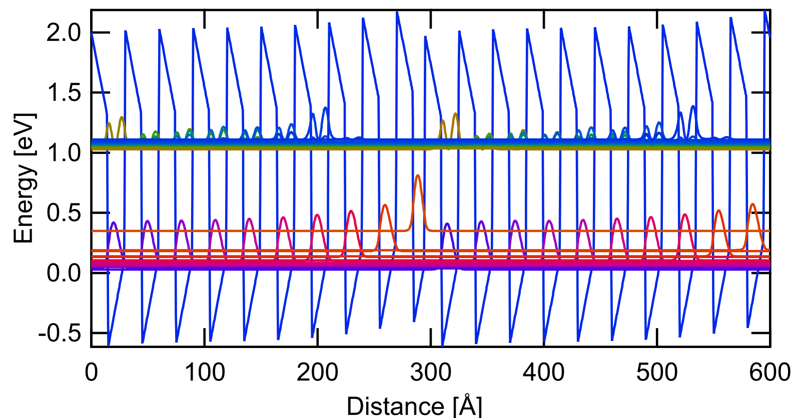

Figure F.1: *cband* simulation of the RTD structure E926.

was grown by PAMBE in Grenoble. Figure F.2 shows the sample structure and figure F.4 the X-ray measurements of E926.

The sample was then processed into small mesa structure with ohmic top and bottom contacts, which diffuse in the SL and minimize further conduction band bending. Unfortunately no negative differential resistance could be seen in the investigated temperature range from 10 K up to room temperature.

In figure F.4 the polarized transmission of the RTD sample is seen. The ISB absorption originates from the SL injector and collector region.

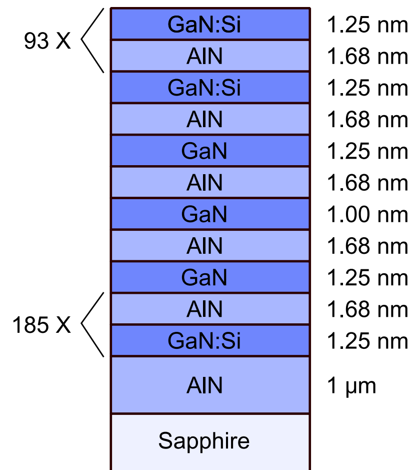

Figure F.2: Design of the RTD structure E926.

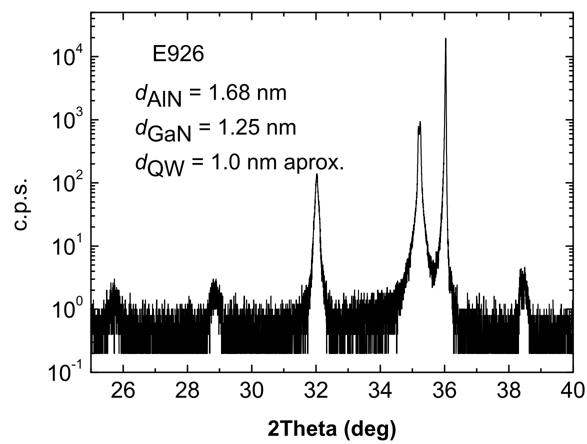

Figure F.3: X-ray measurement of sample E926.

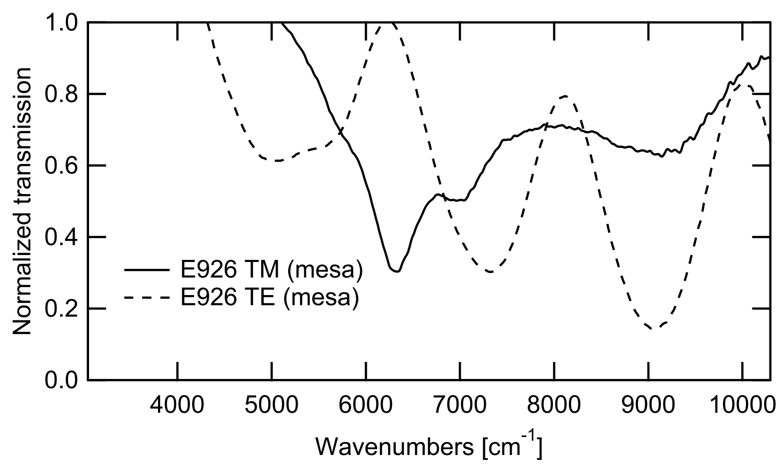

Figure F.4: Measured rapid scan transmission of the RTD structure E926.

Appendix G

Input return loss S11

For sample E1065 the electrical input return loss S11 was measured with a network analyzer. The sample was first mounted on an SMA (not the previously discussed BNC) adapter, then a $100\times100\,\mu\mathrm{m}^2$ mesa was soldered to the adapter signal and one stripe contact to the ground.

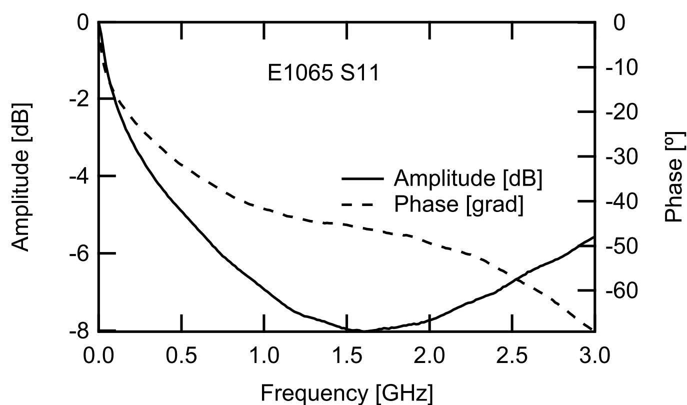

Figure G.1: Reflection amplitude and phase of E1065.

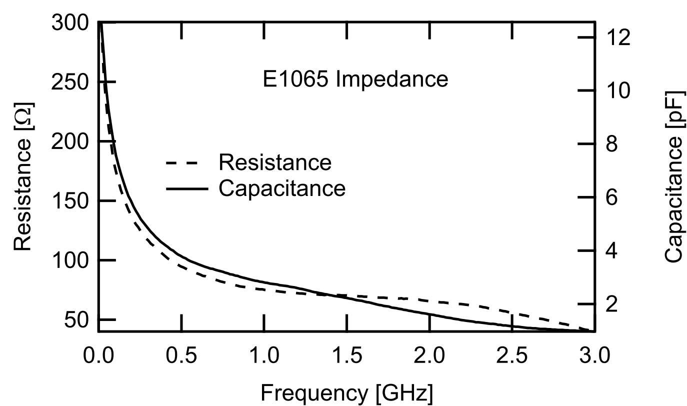

Figure G.2: Resistance and capacitance of E1065.

As seen in figure G.2 the device resistance is highest for low frequency. Its complex value is negative; it is therefore capacitive and probably determined by the cap layer.

Appendix H

Multipeak Absorption

Samples with a thick active region consisting of many SL periods often give rise to a multipeak absorption. The reason for this modulation of broad absorption spectra is not fully understood. Tchernycheva et al. [2006] assign this broadening to monolayer fluctuations in thin QWs.

Sample E1132 (described in table 8.3) with 100 periods has a broad multipeak transmission spectrum. To further investigate it, a 5 mm long 90° waveguide was polished. The NIR source was then focused on this facet via an external aperture to minimize stray light.

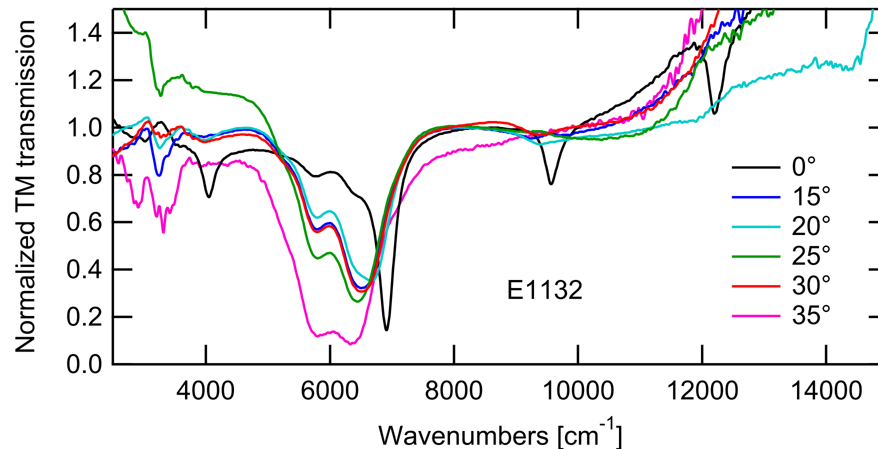

Figure H.1: TM transmission of E1132 at room temperature in a 90° waveguide for different angles of incidence.

The form of the dip in the TM transmission which is due to the ISB absorption is a function of the angle of incidence.

Appendix I

Different Growth Temperatures

Those samples were examined as a function of growth temperature. It was not important to obtain an overall high PV peak amplitude but to compare the PV strength among the three samples, so the backside was not polished (leading to a smaller peak value due to scattering).

The active region of those samples consists of 15 Å GaN QWs and AlN barriers. Buffer and cap layer are AlN. Ti/Au contact stripes were directly evaporated on the unetched cap.

Sample	E1174	E1176	E1178
Growth temperature [°C]	720	725	730

Table I.1: Growth temperature of samples E1174, E1176, and E1178.

As seen in figure I.1 is the PV maximal for E1174, the sample with the lowest growth temperature.

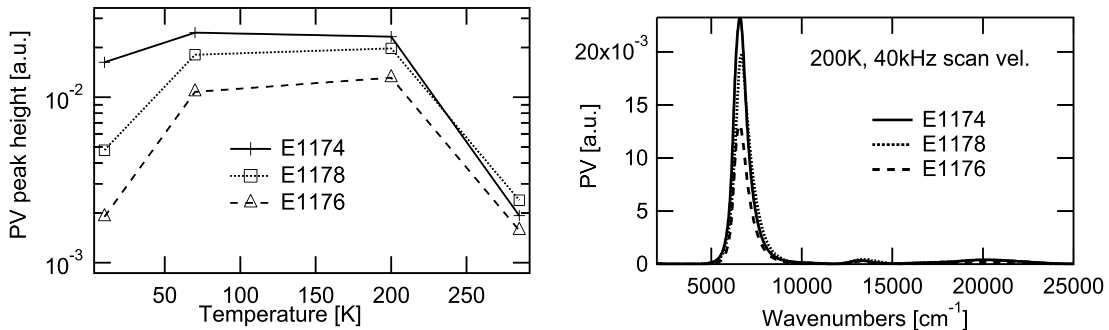

Figure I.1: Different growth temperatures. Left: PV peak height as function of temperature. Right: PV spectra at 200 K.